University of Nottingham
UK | CHINA | MALAYSIA

Random Walk Approach to Predict Electromagnetic Emissions for Multiple Power Electronic Converters

Thesis submitted to the University of Nottingham for the degree of **Doctor of Philosophy, March 2025.**

Erjon Ballukja

20214842

Supervised by

Paul L. Evans
Mark Sumner
David W. P. Thomas
F. B. J. Leferink
Robert Smolenski

Signature _____

Date _____ / _____ / _____

Abstract

This thesis addresses the increasing Electromagnetic Compatibility (EMC) challenges posed by multiple Power Electronic (PE) converters operating simultaneously within a network. As current EMC standards predominantly focus on single-device evaluation, a significant research gap exists in modelling and predicting aggregate electromagnetic interference from multiple converters. The research proposes a new application of Pearson's Random Walk (PRW) theory to characterise Common Mode (CM) electromagnetic emissions in multi-converter configurations.

The investigation demonstrates that Pearson's Random Walk provides an effective statistical framework for modelling electromagnetic emissions from multiple PE converters, where traditional deterministic approaches have proven inadequate. The model is based on the assumption that the sole variable under control is the switching-ON time of the converters. The model employs vectors that represent the phase of waveforms being produced by each converter, associating converter switch-ON times with vector angles to predict aggregated electromagnetic interference. This approach was verified through both simulation studies of eight identical converters and experimental measurements with three DC/DC converters.

Statistical verification through empirical and theoretical cumulative distribution function (cdf) confirmed the model's validity regardless of harmonic

number. Furthermore, the research presents the first explicit computation of the probability that electromagnetic interference is reduced in a multi-converter configuration compared to a single-converter arrangement. Results indicate that whilst electromagnetic interference reduction is possible, this probability diminishes with an increasing number of converters.

The developed methodology offers manufacturers and network operators a robust framework for predicting worst-case electromagnetic emissions in multi-converter systems, thereby addressing requirements specified in current electromagnetic compatibility directives. This contribution advances the standardisation efforts of the IEC CISPR Working Group 4 concerning the impact of increased device quantities on electromagnetic compatibility.

Contents

List of Tables

List of Figures

Abbreviations

AEA All-Electric Aircraft.

cdf cumulative distribution function.

CE Conducted Emissions.

CM Common Mode.

DM Differential Mode.

ecdf empirical cumulative distribution function.

EMC Electromagnetic Compatibility.

EME Electromagnetic Environment.

EMI Electromagnetic Interference.

EVs Electric Vehicles.

FD Frequency Domain.

FFT Fast Fourier Transform.

FT Fourier Transform.

GaAs Gallium Arsenide.

GaN Gallium Nitride.

HEA Hybrid Electric Aircraft.

HF High Frequency.

IGBT Insulated Gate Bipolar Transistor.

LF Low Frequency.

LISN Line Impedance Stabilisation Network.

MEA More-Electric Aircraft.

MOSFET Metal Oxide Semiconductor Field Effect Transistor.

PCC Point of Common Coupling.

pdf probability density function.

PE Power Electronic.

PRW Pearson's Random Walk.

PV Photovoltaic.

PWM Pulse Width Modulation.

RF Radio Frequency.

RF Radio Frequency.

SiC Silicon Carbide.

TD Time Domain.

Chapter 1

Introduction

1.1 EMC Problem

Electromagnetic Compatibility (EMC) is concerned with the generation, transmission and reception of electromagnetic energy. The classical EMC problem is depicted in Fig. 1.1: a source generates the emission that is transmitted to a victim (or receiver) through a coupling path in forms of radiation or conduction. In general, EMC focuses on ensuring electrical and electronic equipment operates correctly within its Electromagnetic Environment (EME) without producing unwanted electromagnetic emissions that might cause other devices to malfunction. EMC typically requires [1]:

1. To mitigate any susceptibility to Electromagnetic Interference (EMI) which usually requires immunity testing;
2. To ensure that an electrical or electronic device does not act as a potential source of EMI, which usually requires emissions testing.

Susceptibility to EMI is generally self-limiting, as products that are vul-

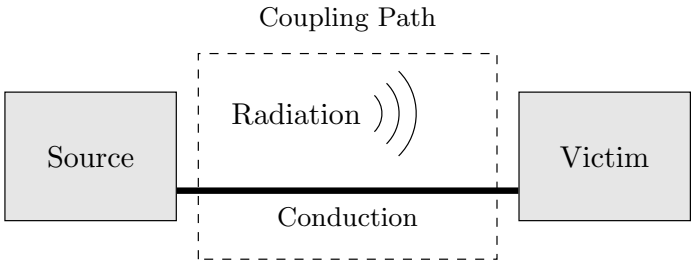

Figure 1.1: Description of the EMI model.

nerable will not function properly and will not satisfy the requirements to be placed in the market. Emissions, on the other hand, present a more complex challenge as a device might operate as intended while still generating interference that compromises the performance of other equipment. This thesis addresses the latter concern, specifically developing a statistical approach to estimate the aggregate electromagnetic emissions of multiple cooperating devices.

1.2 EMI Issues in PE Converters

EMC concerns not only the performance of an electronic device in isolation and within its operational frequency band, but also its behaviour when operating alongside an increased number of devices. The proliferation of Power Electronic (PE) converters represents a significant trend, as these devices play a crucial role in the conversion of electrical energy to achieve higher efficiency, lower emissions and better system performance. PE converters transform, process and control electrical power and energy. These systems convert input power according to specified control parameters, to produce conditioned output power. The power rating of these converters spans a vast range [2]:

- Less than one watt in DC/DC converters within battery-operated portable equipment;
- Tens to thousands of watts in power supplies for computers;
- Kilowatts to megawatts in variable-speed motor drives;
- Up to 1,000 megawatts in rectifiers and inverters that interface DC transmission lines with AC utility power systems.

Common type of converters include:

1. DC/DC converters, which are used to step up or down a DC input voltage into another level of DC output voltage;
2. AC/DC converters (rectifiers), which convert an AC input voltage into a DC output voltage;
3. DC/AC converters (inverters), which transform a DC input voltage into an AC output voltage of controllable magnitude and frequency;
4. AC/AC converters (cycloconverters), which convert an AC input voltage to a given AC output voltage of controllable magnitude and frequency.

PE converters are deployed across multiple critical domains. The following sections present key power electronics applications.

PE play a crucial role in renewable energy systems by interfacing renewable sources such as Photovoltaic (PV) panels and wind turbines with the electrical grid. These converters enable the conversion of variable DC output from renewable sources into stable AC power suitable for grid integration [3, 4]. Moreover, PE converters are integral to the operation of microgrids

(DC or AC), which are localised grids that can operate independently or in conjunction with the main grid [5–8].

In Electric Vehicles (EVs), PE converters manage energy flow between the battery, electric motor and charging systems. DC/DC converters step down the high battery voltage to lower levels suitable for auxiliary systems present in the vehicle. These converters are also used for energy management, allowing the vehicle to either draw power from the battery or feed energy back into it [9, 10].

In aerospace, the trend toward More-Electric Aircraft (MEA), Hybrid Electric Aircraft (HEA) and All-Electric Aircraft (AEA) architectures has significantly increased the reliance on PE converters. This transition is driven by the aerospace industry's imperative to address environmental concerns, reduce maintenance requirements, and ensure cheaper and more convenient flights. PE converters are systematically replacing traditional hydraulic and pneumatic systems with electrical equivalents, leading to improved efficiency and reduced weight [11–13]. Furthermore, the use of wide-bandgap semiconductors, such as Silicon Carbide (SiC) and Gallium Nitride (GaN) is becoming prevalent in aerospace applications due to their ability to operate in harsh environments and to enhance the efficiency and thermal performance of converters [14].

Finally, PE converters are extensively deployed in data centres and service facilities for voltage regulation purposes. For instance, buck converters perform voltage step-down operations while maintaining precise voltage regulation, which is essential for the reliable operation of sensitive electronic equipment typically deployed in these environments [15]. The capability of these converters to deliver regulated outputs is fundamental, as power supply variations may result in system instability and potential equipment

degradation [16]. Furthermore, PE converters significantly enhance energy efficiency within data centres. The implementation of high-density converters incorporating advanced semiconductors such as SiC, GaN and, Gallium Arsenide (GaAs), enables operation at elevated frequencies with enhanced dynamic performance characteristics, which proves to be advantageous in terms of energy consumption [17]. However, the implementation of PE converters presents specific challenges. Firstly, the electromagnetic interactions among multiple converters may generate EMI and compromise power quality, potentially degrading overall data centre performance [18]. Secondly, the degradation and the aging of PE components poses significant reliability concerns for data centres [19].

1.2.1 Source of EMI: Switch Mode Power Converters

In all of the applications described above, PE converters predominantly employ switch-mode power conversion techniques where power semiconductors operate as controlled switches. The fundamental principle relies on modulating the ratio between conduction (on-time) and blocking (off-time) states through various switching patterns that allow to control the output voltage and current. Advanced semiconductor technologies such as Insulated Gate Bipolar Transistor (IGBT) and Metal Oxide Semiconductor Field Effect Transistor (MOSFET) [20–22] have enabled significant reductions in switching transition times [23]. However, while these faster switching transitions improve energy conversion efficiency, they simultaneously generate more rapid voltage and current transients. From an EMC perspective, as it will be discussed in the next chapter, rapid current variations $\left(\frac{di}{dt}\right)$ and voltage variations $\left(\frac{dv}{dt}\right)$ resulting from power converter switching states are sources of electromagnetic emissions [24]. The steep

slopes of the waveforms excite multi-mode oscillations through parasitic coupling mechanisms. These rapid changes generate electromagnetic pulses that manifest as radiated interference, or couple through parasitic inductances and capacitances to create conducted interference [25].

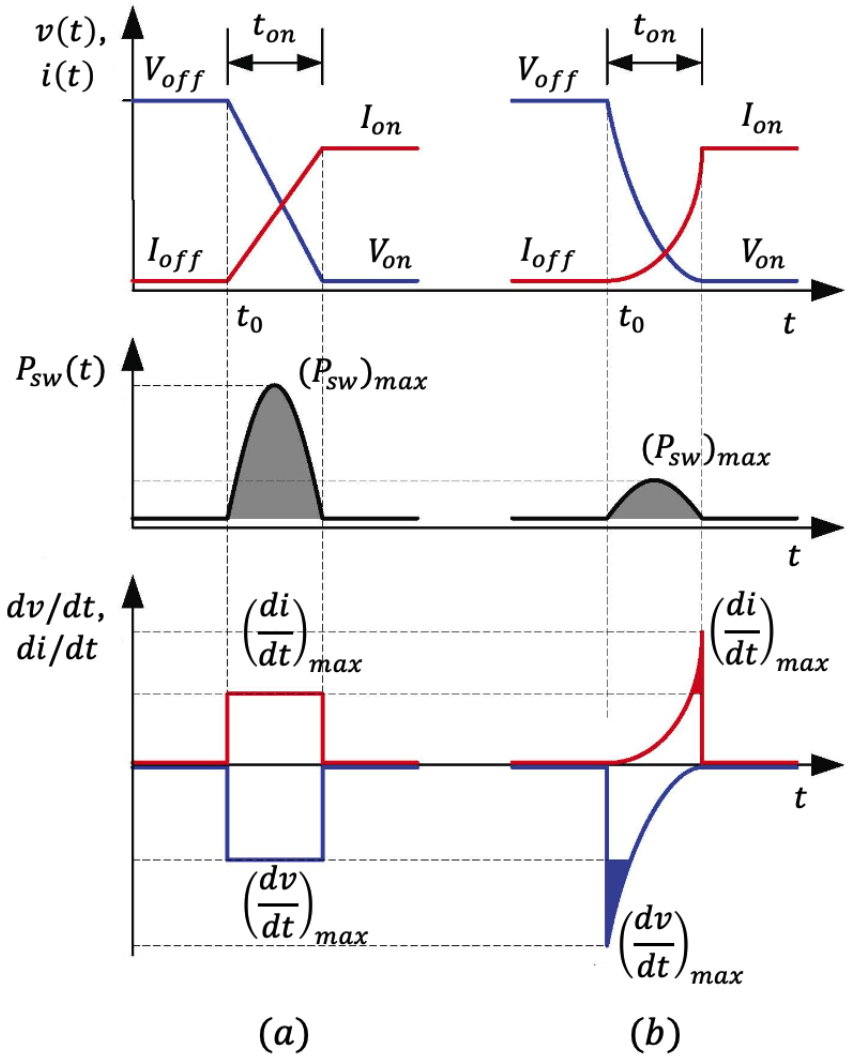

Figure 1.2: Rate of change of current (di/dt) and voltage (dv/dt) during transistor switching-ON for: (a) linear and (b) exponential voltage and current waveforms [24].

Fig. 1.2 illustrates the rate of change for voltage (blue) and current (red) during switching-ON transitions for both linear waveforms (a) and exponential waveforms (b). The exponential case represents a more realistic approximation of transistor behaviour, albeit still simplified. In case (b),

the exponential voltage and current waveforms demonstrate that during the switching-ON process, voltage decreases more rapidly whilst current increases slower compared to case (a), resulting in reduced total switching losses (denoted as P_{sw} in the middle facet). The minimisation of switching losses by reducing the total switching-ON time (equivalently by increasing voltage and current derivatives), is recognised as a fundamental source of EMI in switch-mode power converters [24]. Such emissions are undesirable as they may adversely affect other equipment or the common electromagnetic environment. Furthermore, EMI results from a combination of $\left(\frac{di}{dt}\right)$, $\left(\frac{dv}{dt}\right)$ at each switching instant and the repetition rate of the switching (i.e., the switching frequency). The switching frequency also significantly influences the EMI spectrum.

Fig.1.3 shows an example of a spectrum of trapezoidal waveform where the rise time and fall time are equal.

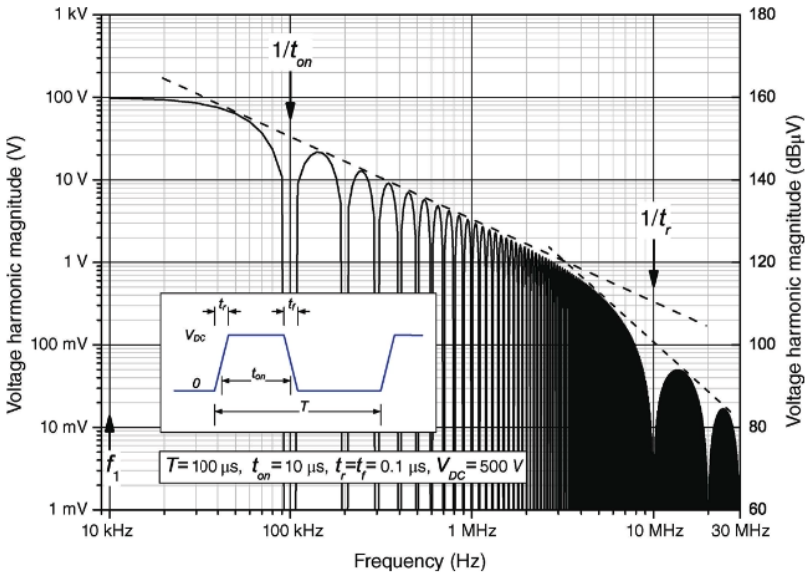

Figure 1.3: Exemplary spectrum of trapezoidal waveform with equal rise time and fall time. [24].

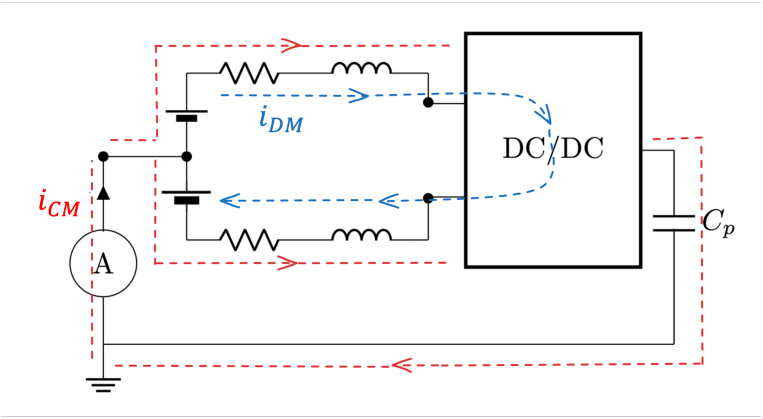

Figure 1.4: CM and DM current paths in a DC/DC converter.

1.2.2 Electromagnetic Emissions

The electromagnetic emissions manifest in two distinct modes: Common Mode (CM) and Differential Mode (DM). Fig. 1.4 shows the CM (red) and DM (blue) paths for the current. Although these modes typically coexist, CM emissions pose the more significant interference challenge [26, 27] and, therefore, in this thesis the focus will be on CM currents. The characteristic oscillatory behaviour of CM currents is determined by two key factors: the voltage slope $\left(\frac{dv}{dt}\right)$ of CM voltage transitions and the resonant frequencies and damping factors of the current paths [25]. Such electromagnetic phenomena coupled with the increasing deployment of simultaneously operating PE converters, intensify interference risks in nearby electronic devices. Consequently, new EMC solutions must be developed to address these challenges.

Electromagnetic emission propagation depends on spectral content, while electronic device susceptibility to interference varies with frequency. This relationship between emissions and frequency-dependent susceptibility has led to the development of EMC standards. Electromagnetic emissions are categorised into four distinct classifications according to contemporary standards. These classifications are defined by two characteristic frequency

boundaries 9 kHz and 30 MHz, as illustrated in Fig. 1.5 [28]:

1. The frequency range above 9 kHz is known as Radio Frequency (RF) range. The 9 kHz frequency is also defined as the limit for Low Frequency (LF) and High Frequency (HF) bands, as defined by IEC 60050-161 [29];

2. The 30 MHz limit differentiates EMC phenomena for conducted emissions below 30 MHz and radiated emissions above 30 MHz. Below this frequency, electromagnetic energy predominantly transfers through conductive paths such as cables and other conducting structures. Above 30 MHz, electromagnetic energy propagates primarily through space as electromagnetic waves [30].

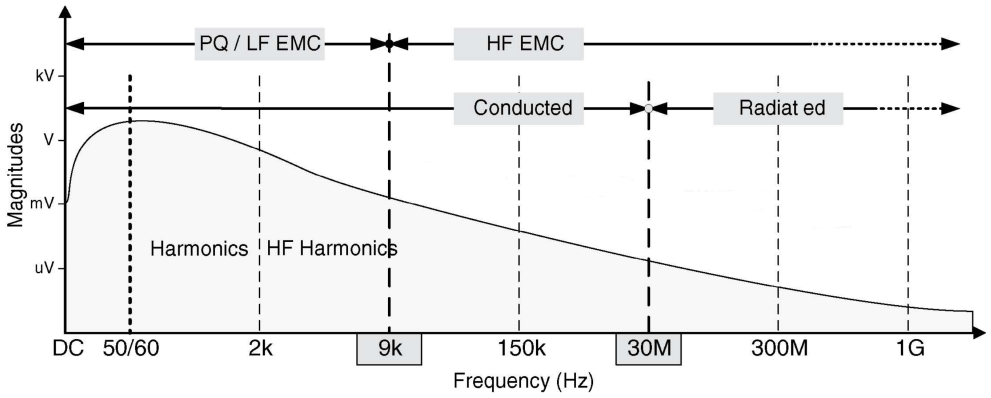

Figure 1.5: Electromagnetic emission frequency band [30].

Fig. 1.5 represents the magnitudes of currents and voltages from electromagnetic emissions of electronic devices. In general, the magnitudes of electromagnetic emissions in power electronic applications decrease with frequency. Indeed, the graph starts at a few millivolts for frequencies close to the grid frequency and reaches much smaller values of microvolts or microamperes in the upper frequency range of the conducted EMI band, close to 30 MHz. Even such low voltages and currents can be harmful due to the high frequencies that result in propagation through parasitic coupling [28].

In conclusion, PE converters, predominantly utilising advanced semiconductor technologies such as MOSFET or IGBT, generate significant electromagnetic emissions within the HF conducted emission range of 9 kHz to 30 MHz, corresponding to typical switching frequencies. These emissions can rapidly propagate through conductive paths. As mentioned above, the primary source of EMI in PE converter systems stems from rapid voltage and current transitions, which couple both inductively and capacitively to nearby conductors.

1.3 Directives and Lack of standards

As stated above, PE devices are increasingly used not just independently, but in cooperation with other equipment. This introduces EMI risks, necessitating appropriate EMC solutions. All electronic devices, including PE converters, must comply with current EMC regulations before market placement. In the United Kingdom, these requirements are specified in 'the Electromagnetic Compatibility Regulations - SI 2016/1091', where Schedule 1 (Essential Requirements), article 1 [31] states: "Equipment must be so designed and manufactured, having regard to the state of the art, as to ensure that:

(a) the electromagnetic disturbance generated does not exceed the level above which radio and telecommunications equipment or other equipment cannot operate as intended;

(b) it has a level of immunity to the electromagnetic disturbance which allows it to operate without unacceptable degradation of its intended use."

The EMC requirements established within the European Union's EMC Directive 2014/30/EU [32], specifically in Annex I (Essential Requirements), Section 1(a), present analogous stipulations to the British regulation. Furthermore, Clause 14 of said directive emphasises that "manufacturers should construct equipment intended to be connected to networks in a way that prevents networks from suffering unacceptable degradation of service." Of particular significance is Clause 31, which addresses devices capable of multiple configurations. The clause stipulates that EMC assessment shall verify compliance with essential requirements across all configurations that the manufacturer deems foreseeable. In such instances, it is deemed sufficient to conduct assessments focusing on two critical configurations:

- "The configuration most likely to cause maximum disturbance;
- The configuration most susceptible to disturbance."

The requirements outlined in these directives raise the following questions:

- What is the total effect when multiple EMI sources are connected to the same system?
- How do the operating conditions of each individual source affect the total EMI?
- How can the worst-case scenario be defined?
- How can manufacturers be best advised in testing their devices and predicting EMC outcomes?

The directives require manufacturers to consider worst-case scenarios in EMC assessments; however, this requirement presents methodological challenges, as the directives provide no guidance on how to achieve this, despite

making it mandatory. Such guidance is particularly relevant due to the unpredicted device configurations that may arise. A fundamental limitation exists in current standardisation approaches which focus on single-device evaluation. However, this presents a fundamental issue - while individual device EMC compliance may be achieved, multiple devices operating simultaneously may not meet this requirement. This can be expressed as:

$$\mathrm{CE}_{individual} \not\Rightarrow \mathrm{CE}_{multiple}$$

where individual EMC compliance does not guarantee EMC compliance in multi-device scenarios. For instance, in the context of data centres, EMI phenomena can manifest when PE devices, such as inverters (e.g., PV inverters), interact with energy meters. To illustrate this point, even though a single solar inverter installed on a roof may not cause energy meters to malfunction, installing an array of solar inverters provides no guarantee of continued proper meter function. Indeed, Leferink *et al.* [33] demonstrated that devices meeting individual CE marking requirements, can fail to operate correctly when integrated into larger systems due to EMI, manifesting as unreliable meter readings.

Thus, models for predicting electromagnetic behaviour in N-device configurations become necessary [34]. The directives specify requirements without providing implementation methodologies. This omission represents a significant research gap as models for predicting electromagnetic behaviour in multi-device operations are required. This thesis aims to investigate new measurement and simulation methodologies for characterising and predicting EMI in multi-converter configurations. Furthermore, the research aims to derive models capable not only of predicting electromagnetic behaviour but also of computing the probability for reducing EMI in multi-converter

configurations which can lead to furture work such as development of algorithms for EMI mitigation. This objective aligns with the work of the IEC CISPR Working Group 4, which focuses on the impact of increased device quantities on EMC and radio protection [35].

1.4 Proposed Method

The primary objective, as understood from above, is to derive and verify models for configurations in which multiple PE devices operate simultaneously. Furthermore, models capable of predicting electromagnetic emissions from multiple devices operating concurrently, based on the behaviour of an individual device, are required. Both the EMC and PE research communities have investigated the modelling of multiple interference sources [36–43]. However, existing approaches address this challenge through purely deterministic approaches, as will be examined in Chapter 2. These methods characterise converter disturbances through deterministic models, which raise questions about their suitability. A significant limitation of deterministic approaches lies in their restricted representation of actual system behaviour. These approaches do not account for the limited control over PE devices within the grid, for example of the phase of the carrier signals of each device. Here is where statistical approaches can help in taking these aspects into account.

To demonstrate this concept, consider a simulated configuration of two ideal PE converters as shown in Fig. 1.6, comprising two DC/DC full-bridge converters with resistive-inductive elements representing the parasitic components in both the converters and their connecting bus bars. The parasitic capacitance C_p creates a path for the CM current to flow (in red).

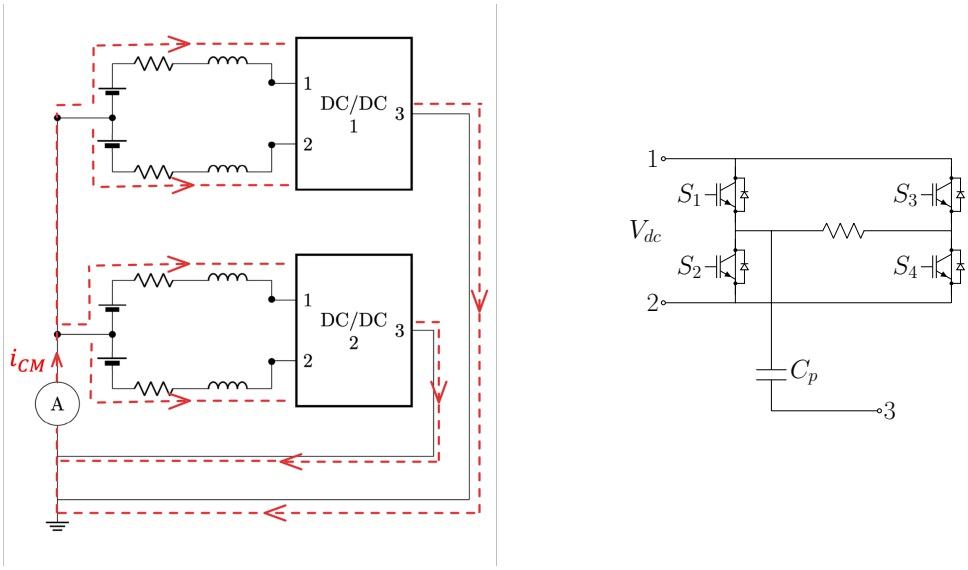

Figure 1.6: Two DC/DC converters, each comprising a full-bridge topology with asymmetric parasitic capacitance (C_P) to ground. CM current path indicated in red.

The resistive-inductive elements interact with the converter's parasitic capacitance C_p to produce an oscillatory CM current waveform. Fig. 1.7 illustrates the CM currents generated by these converters, with each current exhibiting damped oscillations. The first converter activates at $t = 0$ (upper panel), while the second activates after a phase delay of 180 degrees (middle panel). The sum of CM currents (lower panel) results in complete cancellation, representing optimal EMI performance (best case scenario).

In contrast, Fig. 1.8 illustrates the scenario in which the second converter activates with a 360-degree phase delay (middle panel) relative to the first converter, which activates at $t = 0$ as before (top panel), resulting in a doubling of the CM current. This configuration represents the maximum emission scenario (worst-case).

These observations lead to two questions:

1. What is the electromagnetic behaviour between these two extreme cases?

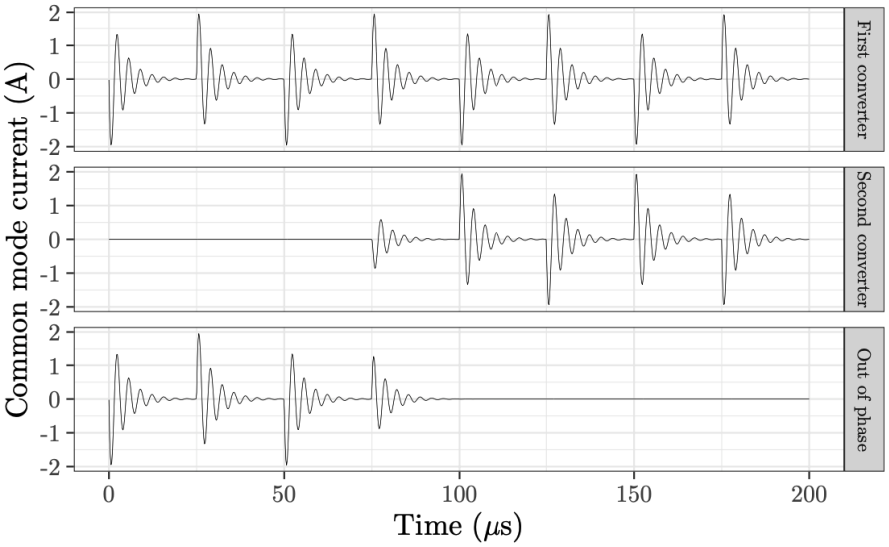

Figure 1.7: Common-mode current damped oscillations of two power electronic converters operating out of phase.

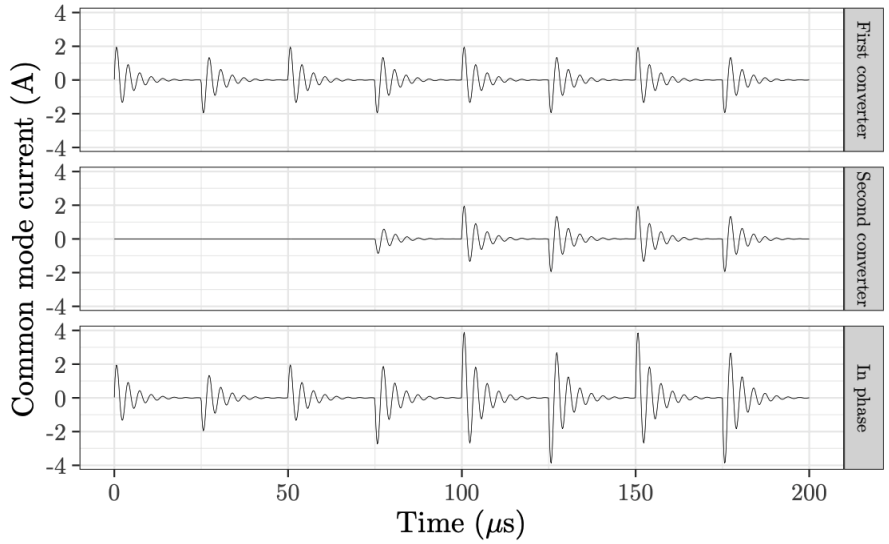

Figure 1.8: Common-mode current damped oscillations of two power electronic converters operating in phase.

2. Are there additional configurations that could produce equivalent worst-case emission scenarios?

The idea that this thesis is proposing, is to take a worst case scenario for characterising worst-case electromagnetic emissions in multi-converter systems. A simplistic approach to quantifying the aggregate CM noise generated by N converters would suggest multiplying the maximum emission level of a single converter operating at full load by N. However, this approach does not account that all of those converters have different switching phases, which can lead to a degree of natural cancellation in the aggregate CM noise, as previously demonstrated.

To address this challenge, statistical approaches are necessary to accurately model the EMI generated by multiple PE converters. This thesis proposes the application of Pearson's Random Walk theory as a suitable mathematical framework.

Pearson's Random Walk

The main idea is that when considering multiple PE converters connected to a DC microgrid, and each of these converters injecting CM noise into the system, it becomes essential to understand how to quantify the CM noise from any number of converters, based on the knowledge of the CM noise of a single converter. This quantification allows us to examine the influence of the combined CM noise on other equipment.

This thesis proposes the application of Pearson's Random Walk as a statistical technique for modelling common-mode noise in multi-converter configurations. In this approach, each converter is identified with an element of the random walk, with converters switched-ON with a random walk pat-

tern. Similarly to predicting the system state after N random steps, this methodology predicts the contributions of an increased number of converters to the total emission levels when N converters operate simultaneously.

1.5 Research Project: SCENT

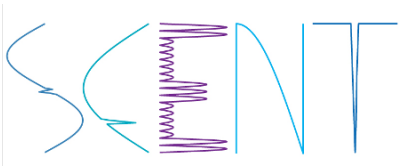

This research was conducted within the framework of Smart Cities EMC Network for Training (SCENT), a Marie Skłodowska-Curie Action project supported by the European Union's Horizon 2020 programme under grant agreement no. 812391. The initiative addressed the challenges of EMC in Smart and Sustainable Cities, particularly concerning the complex electromagnetic interactions between power electronic devices. Furthermore, the research was focused on the impact of the increasing number of electronic devices on EMC which included methods for EMI measurement in multi-converter configurations.

Scent was a consortium of three academic institutions: the University of Nottingham (United Kingdom), the University of Twente (Netherlands) and the University of Zielona Góra (Poland). The programme aimed to develop highly skilled EMC engineers through specialised training and networking opportunities.

This thesis was conducted within Work Package 6, which contributed to the project's objectives through statistical and probabilistic analysis, and Work Package 7, which focused on measurement techniques and experimental evaluation of power networks.

This project has received funding from the European Union's Horizon 2020 research and innovation programme under the Marie Skłodowska-Curie grant agreement No 812391.

1.6 Thesis Objectives

The main objective of this thesis is to demonstrate that statistical methods, can be effectively applied to EMC problems, including describing multi-source EMI scenarios.

More specifically the thesis has the following specific objectives:

1. propose a methodology to characterise the electromagnetic behaviour of multiple PE devices from an EMI perspective;
2. discuss whether the proposed methodology, based on Pearson's Random Walk, is applicable to PE converters;
3. verify the proposed methodology through both simulation and experimental investigation;
4. quantify the probability of EMI reduction in multi-converter configurations compared with single converter arrangements.

1.7 Thesis Contributions

The contributions of this thesis are as follows:

- The thesis addressed several objectives established by the IEC CISPR Working Group 4 - Impact of 'increased number of devices' on EMC and radio protection [35]. Specifically, the work of this thesis aligned with the group's investigation into new measurement and simulation methods for EMI in multi-converter configurations.

- The thesis developed a novel application of Pearson's Random Walk theory to analyse electromagnetic emissions in PE converter systems. Although this statistical methodology is well-established in its original domain, it has not previously been applied to EMC analysis. In this context, the thesis presented a mathematical framework for modelling the aggregation of electromagnetic emissions across multiple PE converters.

- The thesis developed a methodology to test and verify the Pearson's Random Walk model in the EMC field. The method was verified through both simulation and experimental data, with results confirming its validity.

- The thesis provided a mathematical formulation to calculate the probability of electromagnetic emissions reduction in multi-converter configurations, compared to single-source interference scenarios. This theoretical framework was verified through both simulations and experimental measurements on a real test setup. The results demonstrated close alignment with the theoretical formula. Notably, this probabilistic approach to electromagnetic emissions reduction had not been previously addressed in the literature.

The research presented in this thesis is based on three conference papers and one journal paper authored by the thesis author.

1.8 Research Publications

The following research papers were published under the SCENT project with the author as the main contributor:

Journal publication:

- E. Ballukja, K.Niewiadomski, P. Koch, J. Bojarski, P. Evans, N. Moonen, M. Sumner and D. W. P. Thomas, "A Pearson's Random Walk Method of Estimating the Electromagnetic Emissions of N Parallel Connected Power Electronic Converters" in *IEEE Transactions on Electromagnetic Compatibility*, vol. 67, no. 3, pp. 1004-1015, April 2025, doi: 10.1109/TEMC.2025.3556297.

Conference proceedings:

- E. Ballukja, K. Niewiadomski, D. W. P. Thomas, S. Sumsurooah, M. Sumner and J. Bojarski, "A Statistical Approach to Predict the Low Frequency Common Mode Current in Multi-Converter setups," *2023 IEEE Symposium on Electromagnetic Compatibility & Signal/Power Integrity (EMC+SIPI)*, Grand Rapids, MI, USA, 2023, pp. 7-12;
- E. Ballukja, I. Aitbar, K. Niewiadomski, D. W. P. Thomas, M. Sumner and R. Smolenski, "Stochastic Approach to Modelling Emissions of Multiple Power Electronic Converters," *2023 IEEE 7th Global Electromagnetic Compatibility Conference (GEMCCON)*, Nusa Dua, Indonesia, 2023, pp. 28-28;

- E. Ballukja, K. Niewiadomski, A. Pena-Quintal, D. W. P. Thomas, S. Sumsurooah and M. Sumner, "Stochastic Modelling of Power Electronic Converters under Uncertainties," *2022 IEEE International Symposium on Electromagnetic Compatibility & Signal/Power Integrity (EMCSI)*, Spokane, WA, USA, 2022, pp. 232-237.

Additionally, the following publications were produced under the SCENT project as a co-author:

Conference proceedings:

- K. Niewiadomski, E. Ballukja, P. Lezynski and N. Moonen, "On Sensitivity Analysis Techniques for PE Circuit Simulation," *2024 International Symposium on Electromagnetic Compatibility - EMC Europe*, Bruges, Belgium, 2024, pp. 162-167;
- I. Aitbar, S. Voskresenskyi, E. Ballukja, D. W. P. Thomas and S. Greedy, "EMI Modelling and Validation Methods in Electrified Railways," *2023 International Symposium on Electromagnetic Compatibility - EMC Europe*, Krakow, Poland, 2023, pp. 1-5;
- S. Voskresenskyi, I. Aitbar, E. Ballukja, K. Niewiadomski, D. W. P. Thomas and S. Greedy, "State of the Art of Near-Field Scanning: Contemporary Standards and Methods," *2023 IEEE 7th Global Electromagnetic Compatibility Conference (GEMCCON)*, Nusa Dua, Indonesia, 2023, pp. 29-30;
- A. D. Khilnani, A. E. Pena-Quintal, E. Ballukja, M. Sumner, D. W. P. Thomas, L. Sandrolini and A. Mariscotti, "Influence of Impedance Interaction & Comparability on Spectral Aggregation (2–150 kHz) in DC Grids," *2022 International Symposium on Electromagnetic Compatibility - EMC Europe*, Gothenburg, Sweden, 2022, pp. 788-792;

- A. D. Khilnani, K. Niewiadomski, C. Rose, M. Sumner, D. W. P. Thomas, E. Ballukja, L. Sandrolini, A. Mariscotti, "Power Quality Analysis (0-2kHz) in DC/DC Converters under Steady State and Transient Conditions," *2020 International Symposium on Electromagnetic Compatibility - EMC Europe*, Rome, Italy, 2020, pp. 1-5.

1.9 Thesis Structure

The rest of the thesis is structured as follows:

Chapter 2 discusses the origins of electromagnetic emissions in PE converters and their aggregate effect in multi-converter configurations. Subsequently, the chapter reviews current literature concerning the modelling of multiple EMI sources, demonstrating the limitations of deterministic methods and establishing the need for statistical analysis.

Chapter 3 introduces the concept of Pearson's Random Walk and establishes its analogy to the behaviour of multiple PE converters. The chapter presents a mathematical model for the summation of electromagnetic emissions in multi-converter configurations. Furthermore, it examines Kluyver's solution regarding the distribution of contributions to emission levels generated by multiple PE converters.

Chapter 4 presents the verification methodology for the Pearson's Random Walk model. The primary objective is to verify that Pearson's Random Walk, which generates vectors in various directions analogous to a random walk process, can characterise the behaviour of multiple PE converters. The verification comprises two stages: a simulation framework using eight identical converters, each connected to an individual DC source, and an

experimental implementation using three DC/DC converters. The results demonstrate successful verification through both simulation and experimental data.

Chapter 5 presents the statistical verification of the Pearson's model using empirical cumulative distribution function (ecdf). The results are structured as follows: first, a comparison of the Pearson's model with simulation and experimental data using ecdf is presented. Then, the chapter concludes by computing the probability of EMI reduction in a setup with multiple converters configuration versus single converter configuration.

Finally, chapter 6 concludes the thesis by summarising the key findings of the proposed method and outlines possible ways of extending this research.

Chapter 2

Literature Review

2.1 Power Electronics as a Source of EMI

The widespread adoption of PE converters, their integration with power networks, and the adoption of wide-bandgap semiconductors such as Gallium Nitride (GaN), Silicon Carbide (SiC) and Gallium Arsenide (GaAs) have resulted in significantly reduced switching transient times (t_{ON} and t_{OFF}), presenting EMC challenges [44]. These converters typically operate within interconnected systems, where multiple devices function simultaneously and continuously, introducing additional EMC concerns [45]. Furthermore, converters may experience beating phenomena due to minor variations in operating switching frequencies, which may result in further EMC issues [46]. This section analyses these phenomena with respect to EMI generation in PE converters.

2.1.1 PWM Operation: a Brief Reminder

Pulse Width Modulation (PWM) is a fundamental control technique in PE converters as it enables efficient power control with minimal switching losses while maintaining precise voltage regulation through duty cycle manipulation. An idealised PWM operation is illustrated in Fig. 2.1 where a square wave governs the switching-ON and the switching-OFF of transistors within a PE converter. The square PWM signal considered in the figure is characterised by duty cycle d, a rising edge t_{on} and a falling edge t_{off}, while Δt represents the switching period. Modulating the duty cycle controls the output voltage levels, while the slopes of the rising and falling edges typically manifest in the EMI spectra.

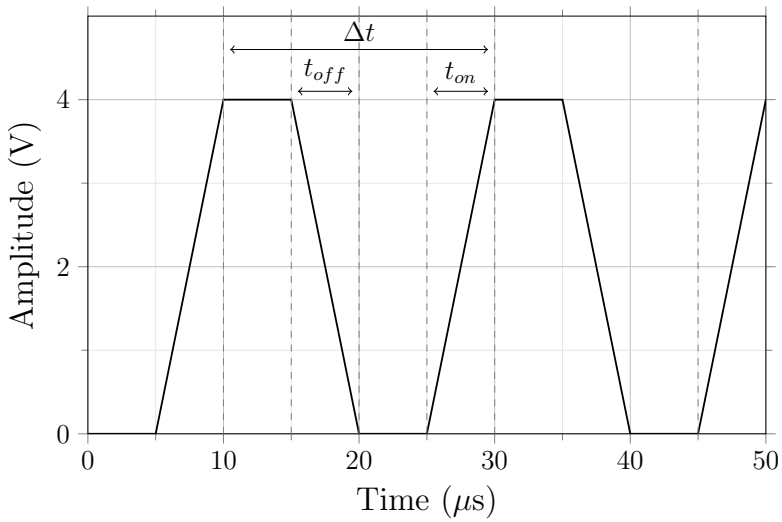

Figure 2.1: PWM signal with indicated parameters.

2.1.2 Origins of Electromagnetic Emissions from Rapid Transistor Switching

PE converters employ modern fast switching devices such as IGBTs and MOSFETs. The use of these fast switching devices provides benefits such

as reduced switching losses and increased converter efficiency. However, they also introduce negative effects, particularly from an EMI perspective. The primary source of EMI in PE converters arises from the high $\left(\frac{dv}{dt}\right)$ and $\left(\frac{di}{dt}\right)$ of the nearly square-wave voltage and current waveforms resulting from the switching operations. The steep slopes of the waveforms in presence of parasitic couplings (mainly capacitive) generate EMI spectra [47].

During steady-state operation, the switch operates in two states: ON ($v(t) = 0$) and OFF ($i(t) = 0$). These states exhibit negligible losses. However, power losses occur during switching transitions. These power losses can be expressed as [48]:

$$P_{\text{sw}} = \int_{t_0}^{t_0+t_{\text{ON}}} v(t)i(t)\ dt, \tag{2.1}$$

where

- P_{sw} represents the power dissipated during the switching event;
- $v(t)$ denotes the voltage across the switch;
- $i(t)$ denotes the current through the switch.

Fig. 2.2 illustrates the switching losses (middle facet) associated with the transistor switching-ON process for exponential waveforms which provide a simplified representation of transistor voltage and current. To reduce switching losses, various methods are used, focusing on increasing either the voltage time derivatives $\left(\frac{dv}{dt}\right)$ or current time derivatives $\left(\frac{di}{dt}\right)$ or both (lower facet). From an EMC perspective, voltage and current changes in switch-mode power converters generate electromagnetic emissions, which must remain within specified limits [49]. Consequently, a fundamental

trade-off exists between efficiency and power density versus electromagnetic emissions and EMC compliance in converter design.

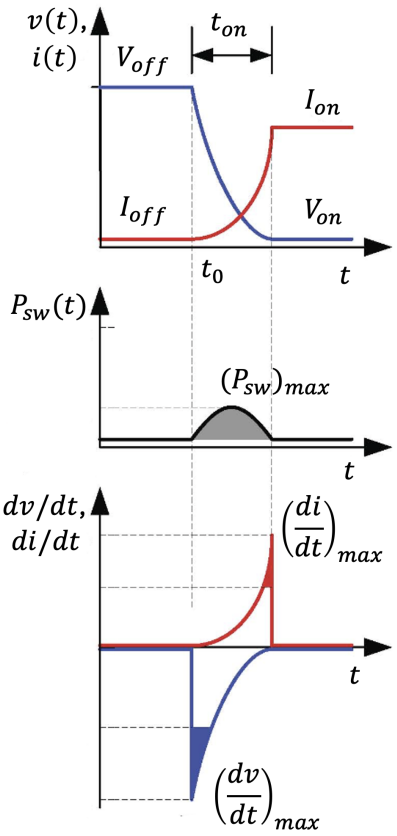

Figure 2.2: Rate of change of current (di/dt) and voltage (dv/dt) during transistor switching-ON for exponential voltage and current waveforms [24].

The spectrum of electromagnetic emissions from PE converters spans a wide frequency range, from low frequencies to higher harmonics. A typical spectrum plot for the CM current is shown in Fig. 2.3 for a single converter (top panel) and for $N = 4$ converters (bottom panel). The most prominent characteristic is the presence of multiple harmonics at integer multiples of the fundamental switching frequency. An increase in switching frequencies causes the high-energy interference to shift into the frequency range corresponding to conducted EMI range (9 kHz - 30 MHz) where converters typically switch [50].

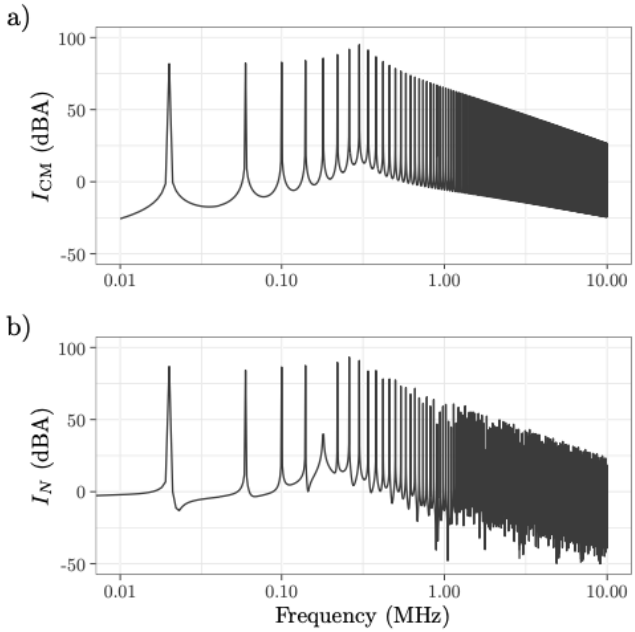

Figure 2.3: CM current spectrum plots: a) for a single converter, b)for $N = 4$ converters [51].

The relationship between waveform characteristics and the conducted emissions spectra, which enables the evaluation of how switching characteristics influence electromagnetic emissions and their spectral content [52], will not be considered in this chapter, as this would greatly complicate the analyses. The effect of multiple electromagnetic sources will be discussed in the following subsection.

2.1.3 Aggregation of Electromagnetic Emissions

The switching elements in PE circuits, as mentioned above, are the primary sources of conducted electromagnetic emissions. Rapid variations in current $\left(\frac{di}{dt}\right)$ and voltage $\left(\frac{dv}{dt}\right)$ couple inductively and capacitively through parasitic elements onto other conductors. The electromagnetic emissions, as introduced in the previous chapter, may be separated into Common Mode (CM) and Differential Mode (DM). The CM noise is a type of EMI induced on signals with respect to a reference ground. The remaining total conducted EMI is defined as DM. These modes typically occur together, with circuit asymmetries leading to coupling between them. However, the common mode causes most interference problems; therefore, in this thesis the focus will be on CM currents. A typical CM current shape is shown in Fig. 2.4, which depicts the measured current flowing through the enclosure parasitic capacitance of a half-bridge converter.

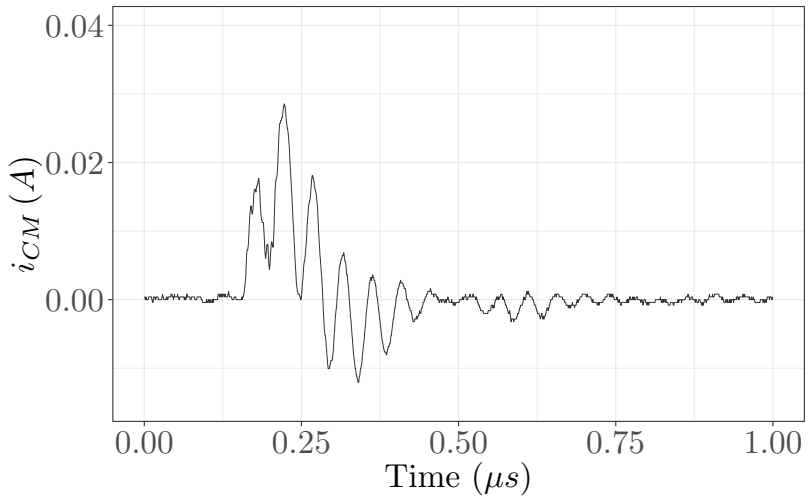

Figure 2.4: A typical CM current waveform exhibiting damped oscillations measured in a half-bridge evaluation board.

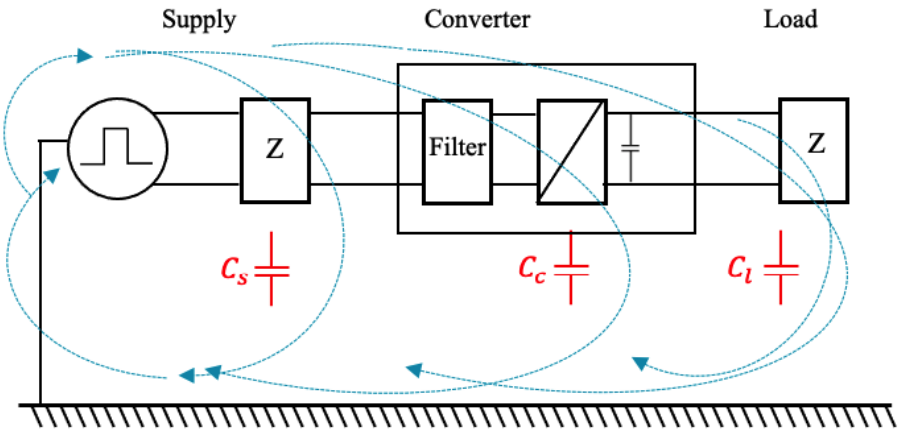

Figure 2.5: CM current paths in a generic PE converter circuit.

Fig. 2.5 illustrates a generic PE circuit and the CM current paths. Typically, several CM paths exist [53]. In the example shown in this figure, a significant path comprises the loop formed by the source, filter, power converter and load. The main common mode coupling occurs through stray capacitance to ground and cable capacitance to ground. In the power converters, among the most significant parasitic elements are the capacitance to ground of the transistor collector and the capacitance to ground of the terminals of the diodes [48]. Furthermore, the aggregation of conduced emissions from multiple connected PE converters could be challenging to assess. Stray capacitances are very variable and require a statistical approach.

2.1.4 Origins of Electromagnetic Emissions from Beating Phenomena

Individual converters operating at slightly different switching frequencies can generate beating phenomena, resulting in slow temporal variations in emission amplitudes [46]. The phenomenon of beating is discussed in [45],

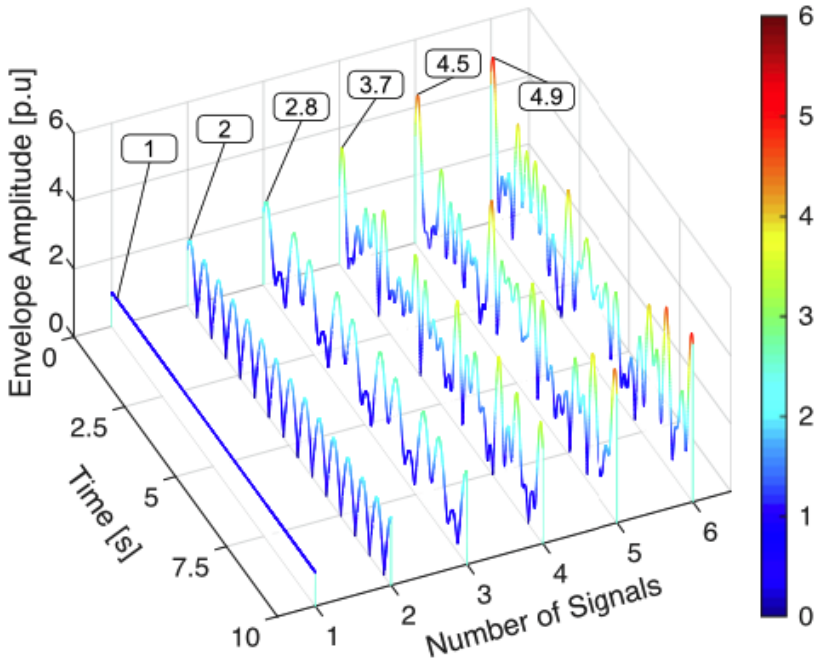

Figure 2.6: Envelopes of signals produced by the superposition of multiple sinusoidal components, illustrating the beating phenomenon [45].

which examines the envelope patterns created by the aggregation of sinusoidal components with slightly different frequencies and uniform amplitude. Fig. 2.6 shows signals formed by the addition of different number of sinusoidal components with random initial phase. These components operate at 15 kHz with a 0.02% random frequency variation. It is evident that smaller frequency differences produce slower variations in the aggregated signal envelopes. From a measurement perspective, greater precision in converter switching frequency results in slower EMI envelope variations, necessitating extended measurement periods for accurate EMC evaluation.

Additionally, these converters operate continuously rather than sequentially, producing repetitive pulses at the switching frequency or its harmonics (for instance, at twice the switching frequency due to turn-on and turn-off events), which leads to EMC issues.

2.2 Modelling of EMI from Multiple PE Converters: State of the Art

Deterministic Approaches

Currently there is a lack of standardised testing procedures for multiple similar devices operating within the same grid. This remains the case despite ongoing discussions by various committees [54] and the specific focus of IEC CISPR Working Group 4 - Impact of 'increased number of devices' on EMC and radio protection [35]. Having established both the need for investigating electromagnetic behaviour of multiple PE converters and the need for statistical methods to develop consensus models describing aggregated interference from multiple PE devices, this section examines relevant research literature based on deterministic approach.

In the standard IEC 61000-3-6 [36], a summation law of the harmonic currents and voltages for the aggregation of conducted disturbances in power systems, was proposed. The mathematical expression for the resultant harmonic current of order h can be represented as:

$$I_h = \sqrt[\alpha]{\sum_{i=1}^{N} I_{h_i}^{\alpha}} \tag{2.2}$$

where:

- I_h represents the magnitude of the resultant aggregated harmonic current of order h for the considered aggregation of sources;
- I_{h_i} denotes the magnitude of the harmonic current of order h for individual devices;

- α is an exponent that varies with the harmonic order. Typical values of α are presented in Table 2.1.

Table 2.1: Summation Exponents for Harmonics

Harmonic Order (h)	α
$h < 5$	1
$5 \leq h \leq 10$	1.4
$h > 10$	2

To formulate such hypotheses, standardised models that predict the Conducted Emissions (CE) generated by multiple PE devices are required. The EMC and PE communities have undertaken research to model the behaviour of multiple interference sources, mostly following deterministic approaches rather than statistical ones.

Espín-Delgado *et al.* [37] proposed an aggregation law for the frequency range 2–150 kHz. Their work assumed that the grid impedance is capacitive and that N devices connected to it have identical input capacitance and identical amplitude of internal emissions. The total current was then calculated by grouping and summing the current over a range of frequencies. This law was experimentally validated in a setup consisting of multiple homogeneous LED lamps. Additionally, the paper compared several models, particularly those presented by:

- Larsson *et al.* [38], inspired to the summation model proposed in IEC 61000-3-6 but assuming that all the currents are the same and can be scaled by a certain factor;

- Rönnberg *et al.* [39], this model assumes that the grid impedance is purely resistive, while the impedance of the device is capacitive;

- Bollen *et al.* [40] this model adds more complexity to the previous one by considering also the inductive component of the grid.

Espín-Delgado's model builds on those presented by Rönnberg and Bollen, with the key difference being that it considers the grid's impedance as capacitive as opposed to resistive and inductive, respectively. Furthermore, while Larsson, Rönnberg, and Bollen's models focus specifically on three-phase four-wire systems and the quantification of neutral supraharmonic currents, Espín-Delgado's model has a broader scope; it addresses the behaviour of supraharmonic currents in low-voltage installations across a wider frequency range. Moreover, the harmonic distortion emitted by N identical devices aggregates at the Point of Common Coupling (PCC) in such a way that, after reaching a maximum value, it decreases with an increasing number of devices. This phenomenon occurs due to differences in frequencies and angles of the spectral components, and most likely due to the cumulative effect of device impedances.

The issue of aggregation of supraharmonic currents in neutral wire of a four-wire three-phase system has also been discussed in [41]. The authors compute a total supraharmonic distortion (TSHC) (equivalent to total harmonic distortion) over a frequency range 40–50 kHz in a neutral wire produced by 20 LED lamps connected to each of three line wires. They also propose to express the influence of supraharmonics on the grid by computing a ratio of TSHC in neutral wire to TSHC in each phase and show how this ratio varies depending on four sources of emissions, namely LED lamps, fluorescent lamps, electric vehicle, and solar power inverter (the latter presenting the highest variability). Moreover, a mathematical formula for the ratio is presented, which involves the number of connected devices N, as well as the resistance and capacitance measured at a common cou-

pling point. The ratio is shown to decrease with increasing the number of devices.

The models proposed in the above studies are purely deterministic, and more complex model, most likely statistical ones, could take into account the variability of load (non-identical but similar devices emitting conducted emissions). In addition, a statistical approach could characterise the devices through probability distributions of their parameters such as capacitance, emission magnitude or frequency characteristics. A statistical approach could account for distortion existing at different frequencies. Finally, statistical approaches offer practical advantages; instead of testing a larger number of similar devices (such as 20, 50 or 100 devices), statistical characterisation could be performed on a smaller number and extended to predict larger system electromagnetic behaviour.

Another interesting study was performed by Czerniewski *et al.* [42], who investigated CE in multi converter systems focusing on how EMI behaves when converters operate together versus individually. Their approach focuses on modelling the behaviour of multiple PE converters, which aligns with the objectives of this thesis. Their study centred on two DC/DC boost converters with identical nominal parameters (V_{in} = 14 V, V_{out} = 48 V, f_{sw} = 110 kHz) but implemented using different manufacturing technologies. Their initial approach allowed the assessment of each converter's emissions individually in a standardized arrangement, utilising a Line Impedance Stabilisation Network (LISN). Measurements were captured in both time and frequency domains. The total emissions were then obtained by summing the individual time-domain waveforms and converting the result to the frequency domain through Fast Fourier Transform (FFT) analysis. In the second approach the total disturbance of the grid was measured using a controlled setup with both converters operating si-

multaneously in a parallel configuration, connected to a common DC bus and to a LISN. The schematic is shown in Fig. 2.7.

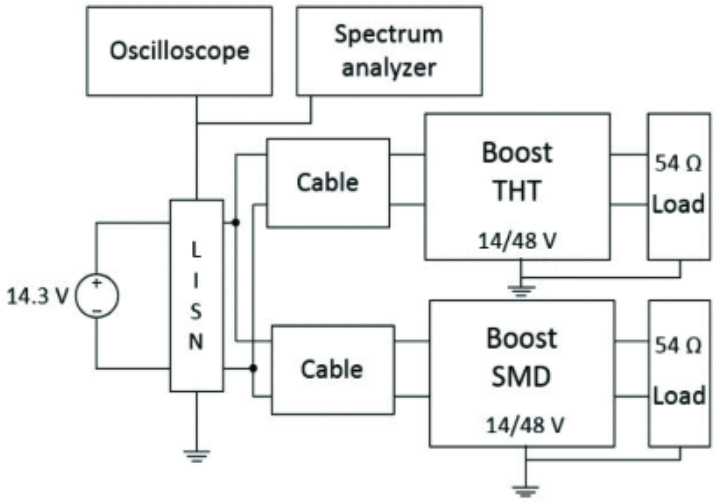

Figure 2.7: Schematic of two boost converters in a parallel configuration [42].

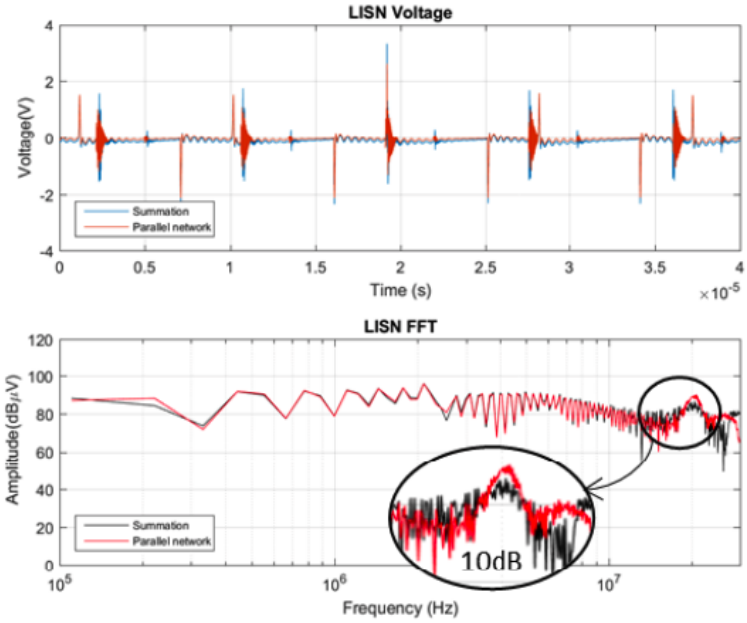

Figure 2.8: Comparison between the sum of EMI disturbance generated by each converter and the overall disturbance generated by the two converters connected in parallel [42].

Experimental comparison between the sum of EMI disturbance generated by each converter and the overall disturbance generated on the DC grid revealed discrepancies above 10MHz, as shown in Fig. 2.8. These discrepancies are most likely attributed to initial impedance variations.

This study further demonstrates the complexities associated with EMC assessment in multi-converter systems for conducted EMI. The electromagnetic behaviour of two electronic devices operating in parallel cannot be simply represented as the linear sum of their individual emissions ($1 + 1 \neq 2$).

In another study, Zumel *et al.* [43] investigate an alternative approach where multiphase converters are utilised to reduce EMI directly at the source. Their research examines the interleaving technique, that entails operating power converters in parallel with intentional phase shifts to facilitate the cancellation of input current harmonics, thereby diminishing EMI levels. Whilst their analysis considers the boundary conditions, when converters operate either in phase or in precise out of phase-phase,it overlooks the spectrum of intermediate configurations. This represents a limitation, as the time delays can be continuos creating numerous potential arrangements for EMI generation and suppression. Their study leaves a substantial gap in understanding the full range of EMI behaviours under varied phase relationships. Indeed, as stated in the Introduction chapter, the two scenarios, out of phase and in phase (shown in Fig. 1.8 and Fig. 1.7 as well), represent the best case (total emission cancellation) and worst case from an EMC perspective. However, what occurs between these extremes is an interesting research question that requires statistical methods to address properly. When considering a system with multiple converters, such as 4 PE converters, various scenarios can occur where the emissions (represented in Fig. 2.9 by the CM current) might double, cancel completely, or

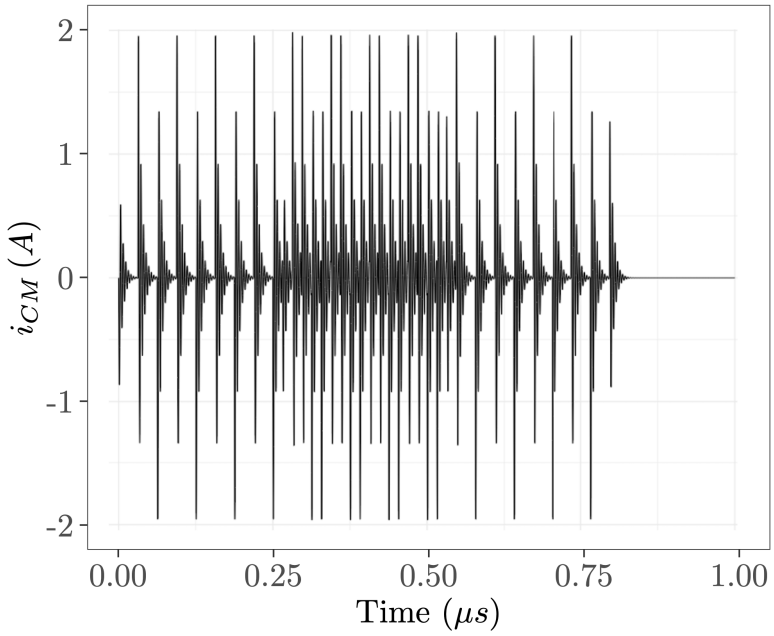

Figure 2.9: Common-mode current damped oscillations of four power electronic converters.

fall somewhere in between. Determining the probability where in this spectrum the emissions will actually fall can be effectively approached through statistical analysis rather than deterministic methods.

The methodologies examined so far approach converter disturbances as deterministic phenomena, which raises questions regarding their appropriateness. In reality, deterministic methods capture only a limited aspect of the actual conditions, failing to account for the incomplete control over power electronic devices within electrical networks (for instance, the carrier signal phases of individual devices). Consequently, a statistical approaches are needed.

2.3 Modelling of EMI from Multiple PE Converters: Need for Statistical Approaches

As stated in the Introduction chapter, when multiple PE converters interface with a grid, the Directive 2014/30/EU [32] - clause 31 stipulates that "where apparatus is capable of taking different configurations (...) it should be sufficient to perform an [EMC] assessment on the basis of the configuration most likely to cause maximum disturbance and the configuration most susceptible to disturbance." This directive implies that manufacturers of PE equipment should consider the aggregated interference introduced into the grid by multiple PE converters rather than the electromagnetic emissions of a single unit. However, current EMI practices indicate that manufacturers typically limit their assessments to standard testing, neglecting the analysis of external and internal electromagnetic compatibility of multiple PE devices [55]. To address these challenges, CISPR 11 (BS EN55011) [56] emphasises the necessity for statistical approaches for EMC evaluation in contexts such as that of multi converter systems. Specifically, *Annex H - "Statistical assessment of series produced equipment against the requirements of CISPR standards"* states that assessment requires testing between five and twelve equipment samples. An example of such an evaluation is presented by Smolenski in [45]. The author conducted 1,000 measurements using the peak detector, which is able to identify changes in measured values. Each measurement had a period of 1 s. The results for five DC/DC converters (measured individually) with similar characteristics are displayed as box-and-whisker plots in Fig. 2.10. According to current EMI standards such as CISPR 11 [56], a single final measurement at one selected frequency is considered sufficient. The distribution of results obtained for each individual converter supports this approach, as the

differences between values measured for individual converters fall within a 1 dB range.

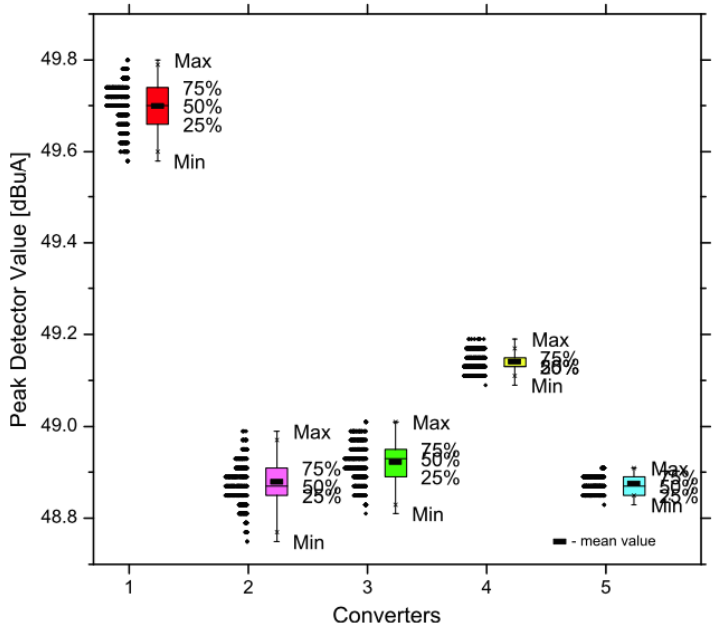

Figure 2.10: Box-and-whisker plots representing peak detector measurements from a single power converter [45].

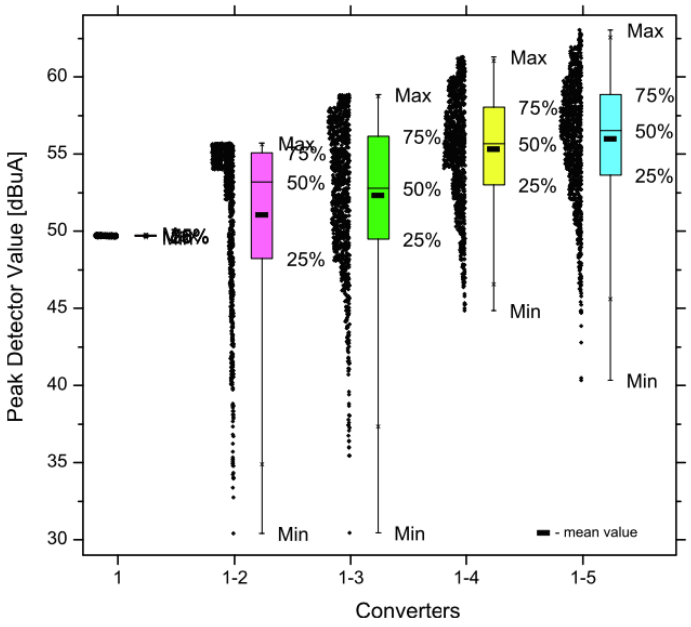

Figure 2.11: Box-and-whisker plots representing peak detector measurements for a group of power converter [45].

However, Smolenski in Fig. 2.11 showed that peak detector measurements obtained for groups of converters exhibit significant differences. The variations between individual measurements reached up to 28 dB, rendering the assessment of EMC in multi-converter systems unreliable. The dispersion of the 1,000 results for multi-converter arrangements (comprising 2 to 5 converters) indicates that the differences between results obtained from these arrangements make evaluation procedures based on single measurements inadequate. Consequently, statistical approaches and consensus models are necessary to predict the electromagnetic behaviour of multiple power electronic setups effectively.

In literature, the necessity of investigating aggregated electromagnetic interference from multiple PE converters is corroborated by an experimental study presented in [55]. The study examined a multi-converter system comprising three identical drives with 1.5 kW induction motors fed by 7.5 kW frequency converters supplied via LISN, as illustrated in Figure 2.12. In this configuration, parasitic parameters of the CM current path determine the frequency of the oscillatory mode. The CM current measurements are presented in Fig. 2.13. The measurement results, presented in Fig. 2.14, display the distributions of thousands of measurements obtained using an average detector in normalised time equal to 1 s for switching frequency. The distributions demonstrate significant variations, particularly during operation of multiple converters. The maximum level recorded for three simultaneous drives exceeded that of drive 2 in single-drive operation by 6 dB, which means doubling the voltage.

The study's findings demonstrate that conducted EMI introduced to the grid by multiple converter drives can significantly exceed the EMI levels generated by individual drives. This indicates an increased probability of EMC-related issues in systems incorporating multiple converters.

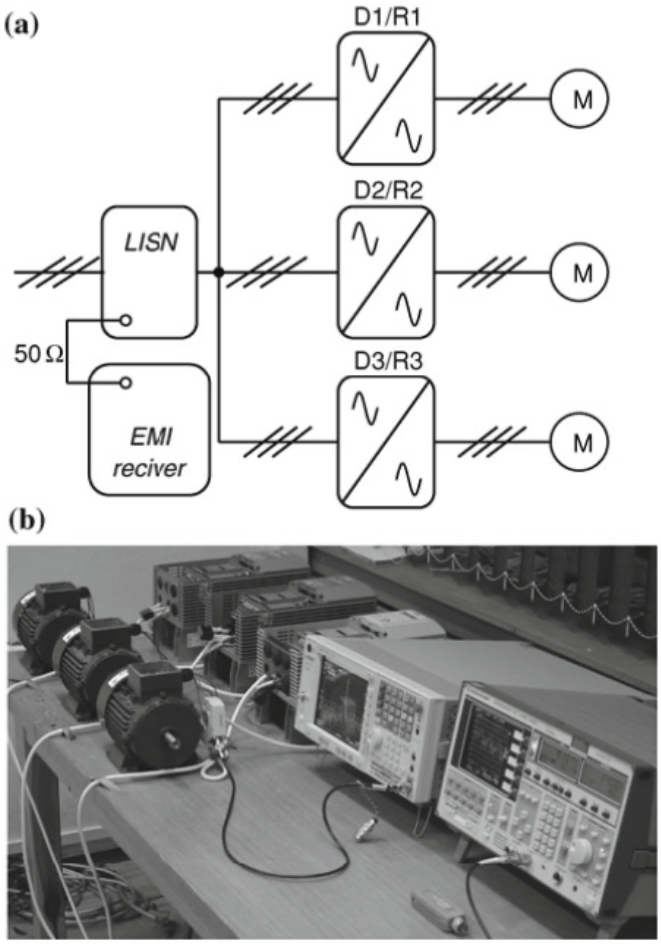

Figure 2.12: Experimental setup for measuring conducted EMI from multiple Power Converters, from [55].

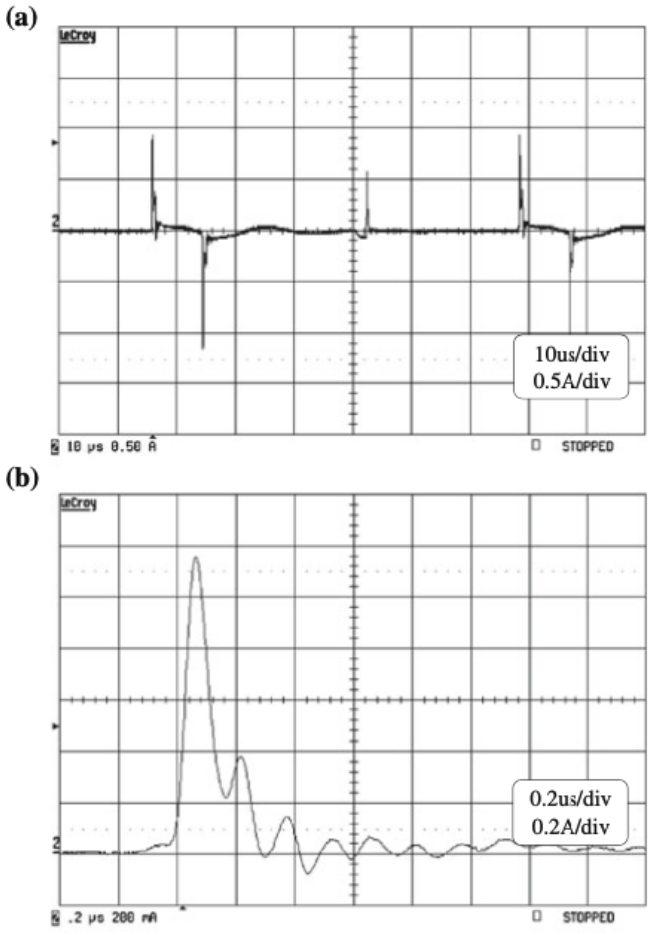

Figure 2.13: (a) Common-mode current in motor protective earth (PE) wire, (b) high-frequency (HF) component of common-mode current, from [55].

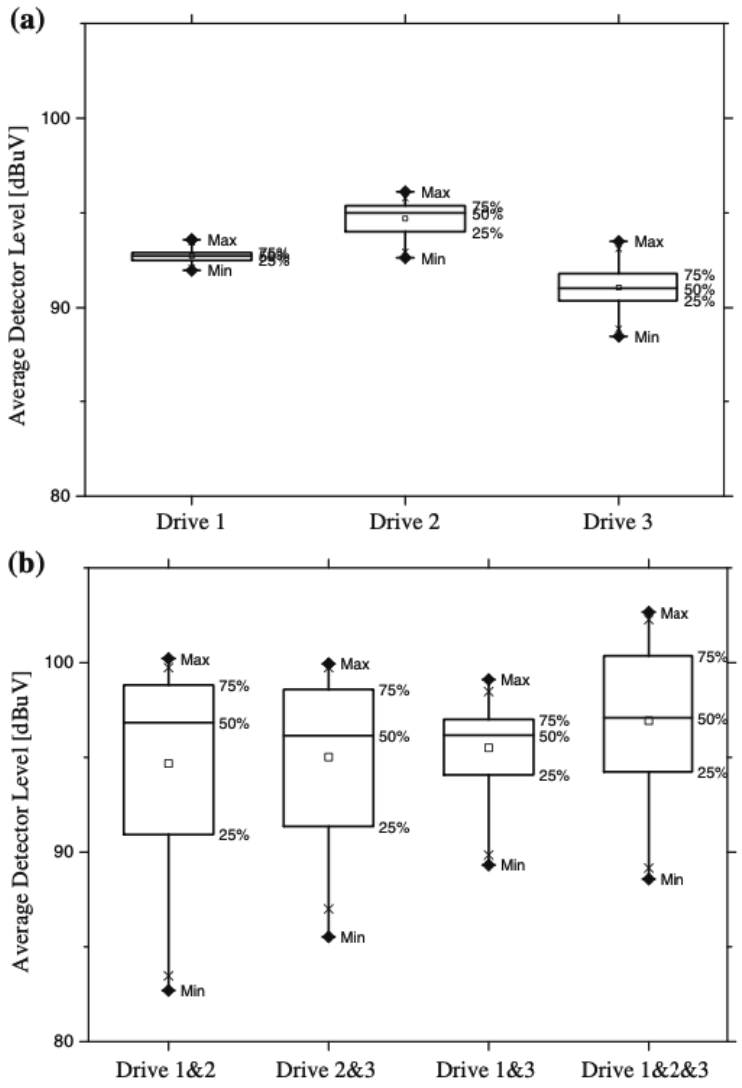

Figure 2.14: Box-and-whisker plot of average detector measurements for: (a) single drive, (b) group of drives, from [55].

In the Smolenski's case study presented, the theoretical expectation for three converters operating simultaneously would suggest EMI levels three times higher than those generated by a single converter. However, the distribution of harmonics reveals that across 1,000 measurements, the probability of reaching this theoretical maximum is notably low. The worst-case scenario of tripled EMI levels occurs infrequently. The measurements demonstrated that with three simultaneous drives, the total EMI exceeded single-drive operation by 6 dB, corresponding to a doubling of voltage levels. These findings substantiate the necessity for statistical rather than deterministic approaches. Two critical concerns emerge from this analysis. Firstly, whilst individual converters may meet EMC compliance requirements, the aggregate system comprising multiple converters might fail compliance testing due to increased EMI levels. Secondly, although the behaviour of EMI generated by single converters is well understood, current testing procedures and standards are not adapted for multiple PE converter systems, necessitating the development of appropriate models.

Furthermore, Bojarski *et al.*[34] emphasised the importance of adopting a statistical perspective when analysing aggregated conducted emissions from multiple PE converters, based on techniques such as Pearson's Random Walk. Their investigation examined CM current as a contributory factor to CE that manifests following switching transitions in PE devices. The authors asserted that emission peak prediction is inherently statistical in nature. Nevertheless, their theoretical model lacked comprehensive validation. Notably absent was any simulation-based or experimental corroboration of the Pearson's Random Walk approach to EMI modelling. This research gap will be addressed in the present thesis through the development of both simulation and experimental methodologies to assess and validate a statistical technique grounded in Pearson's Random Walk

principles. The ultimate objective is to determine probabilistic methods for EMI reduction in configurations involving multiple PE converters.

The fundamental aspects of phenomena associated with interference aggregation in groups of converters are essential for appropriate assessment of electromagnetic emissions, particularly given the absence of relevant standards. Current regulatory frameworks fail to provide objective EMC assessment methodologies for multi-converter configurations. In accordance with EMC directive recommendations, standardisation efforts should address the cumulative effects of electromagnetic phenomena. Statistical analytical approaches may offer valuable tools for accurately evaluating conducted EMI in multi-converter systems. This thesis addresses this research gap by developing a methodology for testing electromagnetic emissions of multiple power converters connected to a grid through a statistical approach. As demonstrated in the previous chapter, compliance of individual equipment with electromagnetic tests does not ensure compliance when multiple units operate simultaneously or when the equipment functions within a larger grid. Individual compliance remains a *conditio sine qua non* for achieving EMC compliance in multiple PE converter systems; however, this condition alone is not sufficient.

2.4 Conclusion

This chapter started with a discussion about PE converters as sources of electromagnetic interference The analysis began with a brief overview of PWM operation and the electromagnetic emissions that arise from rapid transistor switching, highlighting how the high $\frac{dv}{dt}$ and $\frac{di}{dt}$ values of switching waveforms contribute to EMI generation. The chapter also explored

how these emissions aggregate in systems with multiple converters. Lastly the beating phenomena, which occur when multiple converters operate at slightly different switching frequencies, were considered. The chapter progressed to examining the current state of art for modelling multiple PE converters based on deterministic approaches. Evidence from experimental studies demonstrated that multiple converters operating simultaneously can produce EMI levels significantly higher than those of individual units, substantiating the requirement for developing models for EMC within multiple-converter systems. The literature review revealed significant limitations in existing deterministic approaches, including summation laws, which fail to capture the full complexity of multi-converter systems. Consequently, the necessity for statistical approaches to modelling EMI in such configurations was established. The chapter concluded by emphasising this shift from deterministic to statistical methodologies as essential for advancing EMC assessment in multiple power electronic systems.

Chapter 3

Pearson's Random Walk Model

This chapter addresses two main objectives: firstly, to present the mathematical underpinnings of Pearson's Random Walk (PRW) model, and secondly, to demonstrate how this model can be applied to model electromagnetic emissions from PE converters. The main idea is that if one considers multiple PE converters connected to a DC microgrid, and each of these converters injects common mode noise into the system, it becomes essential to understand how to quantify the combined common mode noise from these converters, based on the knowledge of the common mode noise of a single converter. This is important when examining the influence of the combined common mode noise on other equipment. To do this, a consensual model is required to express the common mode current in such a multi-converter setup. The statistical technique deployed for this is "Pearson's Random Walk".

The chapter will begin with a brief overview of random walk theory, followed by an analysis of the CM current in both the Time Domain (TD)

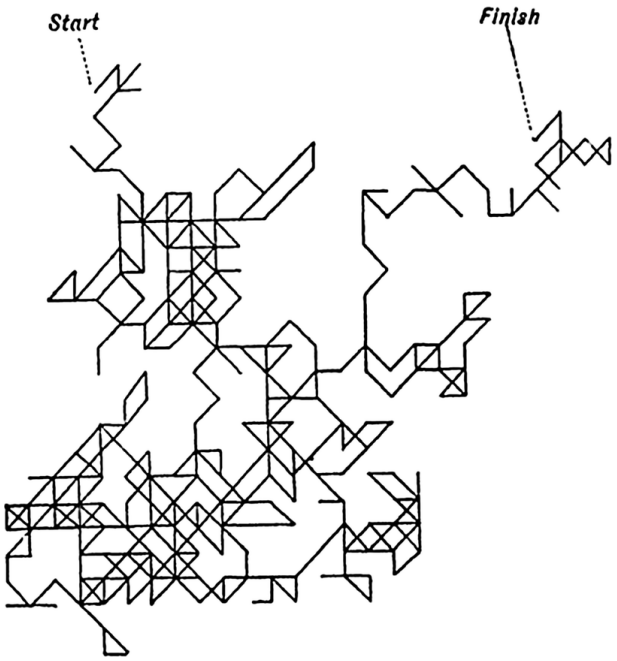

Figure 3.1: The first graph of Random Walk presented by Venn in 1888.

and Frequency Domain (FD) for PE converters. Subsequently, Kluyver's solution to Pearson's problem is analysed and considered for further analysis. This chapter establishes the theoretical foundation for the model which will be tested and verified in the next chapter.

3.1 History of "Random Walk"

The concept of *Random Walk* serves as a cornerstone in various disciplines, including statistics, physics and mathematics. However, in the literature, there is debate about its origin. One study [57] suggests that the roots of random walk theory can be traced back to the 1560s when the Italian mathematician Girolamo Cardano proposed a theory of gambling in *Liber de Ludo Aleae*. Furthermore, it is believed that the logician John Venn presented the first graphical representation of random walk in his 1888 publication *The Logic of Chance*, as shown in Fig. 3.1.

Alternatively, another study [58] attributes the origin of Random Walk to the French mathematician Bachelier, who proposed that share price movements resemble the steps taken by a drunk man. Despite the uncertain history of Random Walk's origin, it can be defined as a stochastic process that describes a path or a trajectory through a series of random steps. In general terms, it refers to a statistical occurrence in which a variable appears to change in an unpredictable manner. The random walk theory has found wide-ranging applications across numerous fields, including finance, economics, biology, physics and sociology. Here are some examples of its use in various contexts [58]:

- **Finance - Stock Prices**: The theory suggests that the stock prices follow random paths and cannot be predicted based on past movements;
- **Econometrics**: Random walk models are employed to analyse time series data such as GDP, inflation and unemployment rates;
- **Biology**: The theory is used to describe the movement patterns of organisms;
- **Physics**: Brownian motion, a fundamental concept in physics, is a type of random walk that describes the motion of particles in a fluid;
- **Computer Science**: Random walk models are used for network analysis and Monte Carlo simulations;
- **Sociology**: The theory can be applied to study social interactions within networks.

In recent years, with the advent of artificial intelligence, the random walk theory has found new applications in algorithms for optimisation, decision-making and problem-solving. Some examples include[59]:

- **Graph Search Algorithms**: Random walks are used to traverse nodes and edges randomly for tasks such as search engine optimisation or network analysis;
- **Randomised Algorithms**: Random walks are employed to solve various computational problems;
- **Network embedding**: Random walk based method are used to extract topological information and calculate proximity between nodes in networks.

The following section will provide a definition of Pearson's Random Walk.

3.2 Definition of Random Walk

The concept of random walk was formally introduced in a 1905 letter to *Nature* by Karl Pearson [60]. In his correspondence, Pearson described a scenario in which a person starts walking from a point O (the origin) along a straight line for a distance u. At each step, the person turns at a random angle and walks another unit u along a new straight line. This process is repeated n times. After n steps, the person will be at a distance d from the origin. Pearson's fundamental question was: What is the probability that after n steps, the person is at a distance between d and $d + \Delta d$ from the starting point? This problem, concerning the probability density of a sum of random vectors, includes a significant part of the theory of mathematical probability and was resolved by Jan Cornelis Kluyver in 1906 [61]. This solution will be examined later in this chapter.

However, one might question how the PRW can be adopted within the electrical engineering field to model PE converters. Pearson's Random Walk

fundamentally is about adding up vectors and describes the displacement from an initial position. These vectors can be applied to model emissions from PE converters. If one considers a configuration comprising multiple PE converters, such as the one illustrated in Fig. 3.2, the vectors represent the phase of waveforms being produced by each converter. The common mode current I_{CM} (at an harmonic h) produced by power converters at a specific frequency can be considered as a vector with an amplitude and phase. Thus, the vectors in Pearson's Random Walk can be used to represent harmonics from various power converters. The notion of the Random Walk, as formulated by Pearson, generates vectors with specific angles, similar to the steps taken by a person, first in one direction, then in a second direction and so on so far. The assumption in the research work presented in this thesis is that the vector angles can represent the switch-ON times (or more precisely, the phase) of the converters. Therefore, these vectors generate a path which corresponds to a unique emissions pattern. The objective is to check if this concept can be used to model the behaviour of multiple PE converters. A detailed examination and proof of this approach will be presented in Section 4.1.3.

To illustrate this concept graphically, consider the diagram shown in Fig. 3.2, which depicts four PE converters. Two switching-ON patterns are presented: one represented by dashed vectors and the second by continuous vectors. The assumption is that the first converter switches-ON at time $t = 0$, and in both patterns depicted, this is represented by the same green vector (dashed and continuous). The additional three converters in the network switch-ON at random times. All vectors have equal amplitude of 1 with phases determined by the random switching-ON time.

Since the first converter always switches-ON at time $t_1 = 0$, the vector representing the second converter would always start at 1. Suppose that:

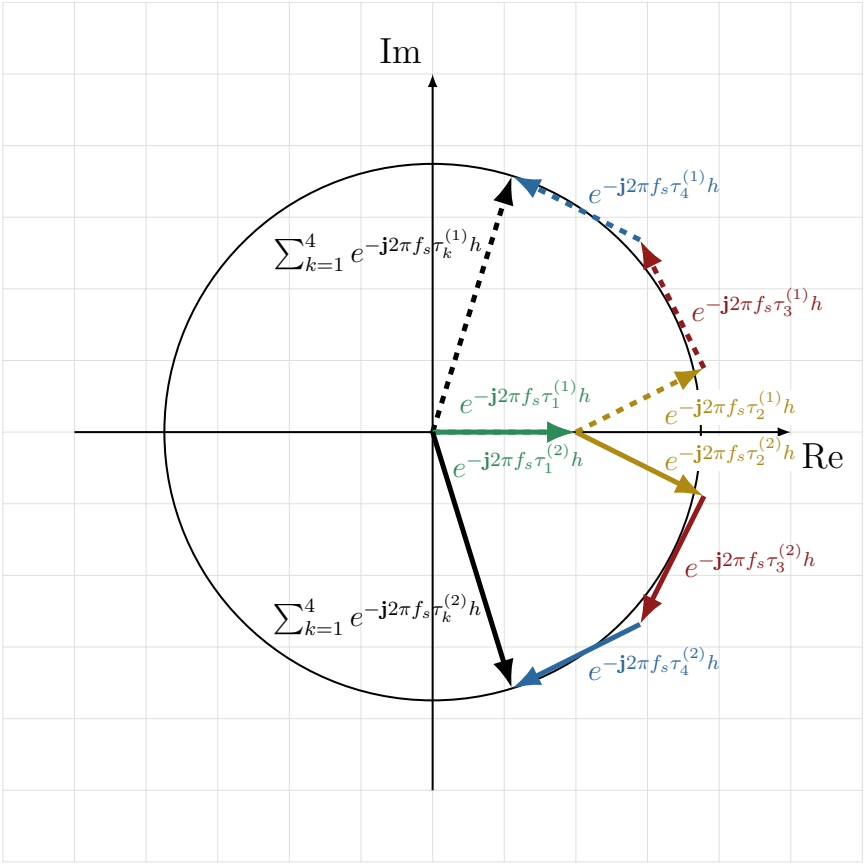

Figure 3.2: Pearson's random walk concept applied to four PE converters, where coloured vectors represent switching-ON times. Two switching patterns are shown (dashed and continuous lines), with the first converter activated at $t_1 = 0$.

- f_s denotes the switching frequency of a converter;
- h represents a harmonic of the switching frequency;
- $\tau_k^{(p)}$ indicates the switch-ON time of the k-th converter with $p = 1, 2$ indicating the patterns according to which the converters switch-ON.

For the first pattern (dashed vectors), the resultant vector is expressed as:

$$\begin{aligned} \sum_{k=1}^{4} e^{-\mathbf{j}2\pi f_s \tau_k^{(1)} h} &= \underbrace{e^{-\mathbf{j}2\pi f_{\mathrm{sw}} \tau_1^{(1)} h}}_{1} + \ldots + e^{-\mathbf{j}2\pi f_s \tau_4^{(1)} h} \\ &= 1 + \sum_{k=2}^{4} e^{-\mathbf{j}2\pi f_s \tau_k^{(1)} h} \end{aligned} \tag{3.1}$$

where:

- 1 represents the contribution of the first converter. Since the first converter always switches-ON at time $t_1 = 0 \rightarrow \tau_1^{(1)} = 0$, then $e^{-\mathrm{j}2\pi f_{\mathrm{sw}} \tau_1^{(1)} h} = 1$;
- $\sum_{k=2}^{4} e^{-\mathrm{j}2\pi f_s \tau_k^{(1)} h}$ represents the contributions of the additional converters that switch-ON at random times.

The resultant of the second switching-ON pattern, represented by continuous line in Fig. 3.2, can be expressed similarly to (3.1). For sake of simplicity, the first vector can be subtracted to depict only the contributions of the additional converters (2, 3 and 4). Consequently, Fig. 3.3 omits the vector of the first converter.

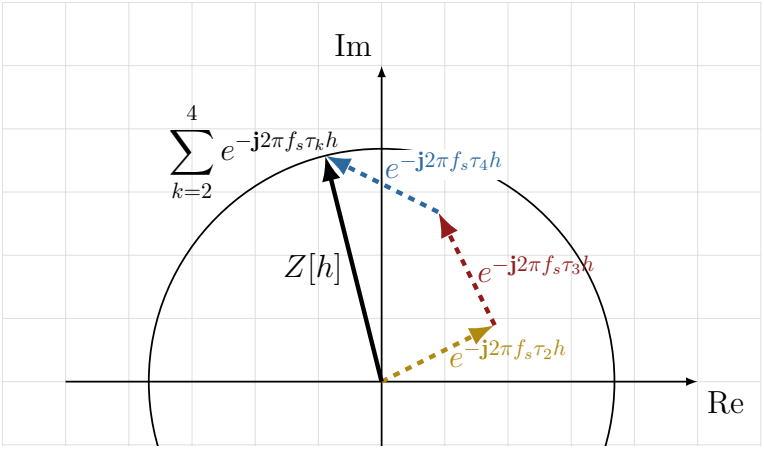

Figure 3.3: Pearson's Random Walk concept applied to four PE converters. The first converter vector is subtracted with respect to Fig.3.2.

When examining the total electromagnetic emissions, one must consider both the emissions from the reference converter (first converter) and the contributions from the additional three converters. The vectors (yellow, red, and blue) represent the different switching-ON times, or more precisely, the contributions due to time shifts to the total emissions with respect to the first converter, generated by two, three, and four converters,

respectively. By varying the angle of these vectors, their directions change, generating new vector paths that correspond to different patterns of activating the converters (as shown win the previous Fig.3.2). The resultant vector (shown in black and denoted as $Z[h]$ in Fig.3.3), representing the summation of contributions, will be discussed in the next section.

The rationale for not depicting the the first converter in the above diagram is bifold:

1. At a testing site, the objective is to test one converter rather than the entire network to predict the behaviour of N similar converters;

2. The first converter (reference converter) serves as a benchmark, as this thesis aims to determine the probability of reducing electromagnetic interference produced by N converters relative to that generated by a single converter.

The following section addresses the analysis of CM current in PE converters, focusing on DC/DC converters. A mathematical expression for this current, which includes the resultant vector mentioned above ($Z[h]$), will be presented in both TD and FD. This expression establishes the summation model for aggregated emissions from multiple converters. The model verification will follow in the next chapter.

3.3 Common Mode Current Analysis

This section examines the CM current of PE converters, particularly DC/DC converters. The focus on CM currents is due to their role as a form of EMI, which is considered one of the primary sources of EMC challenges

[62–64]. The switching operation of the converters induce CM current to flow. These currents may propagate through parasitic capacitance to ground or protective earth wires. EMI propagation paths are typically represented by equivalent RLC circuits due to parasitic elements such as stray capacitances, resistances and inductances. As a result, EMI currents exhibit damped oscillations. The parasitic parameters of the current paths determine the current shape, with one dominant mode of oscillation often distinguishable in a given frequency range [50].

The analysis that follows considers the CM current in both TD and FD. As standards prefer FD analyses, this section proposes a simplified frequency domain model of aggregated interference generated by a group of identical DC/DC converters.

3.3.1 Time Domain

Given that EMI currents typically manifest as signals with damped oscillations, and that a dominant oscillating frequency can often be identified, it is reasonable to model the CM current of a single DC/DC converter as a simplified oscillatory damped signal [34, 65]. This approach allows for a simpler analysis wherein a single oscillation can be expressed as:

$$i_{\mathrm{CM}}(t) = I_0 \sin(\omega t) e^{-\lambda t} \mathbf{1}(t), \tag{3.2}$$

where:

- I_0 represents the amplitude of the single oscillation,
- ω signifies the angular frequency of the oscillation,
- λ denotes the damping factor, which determines the rate at which

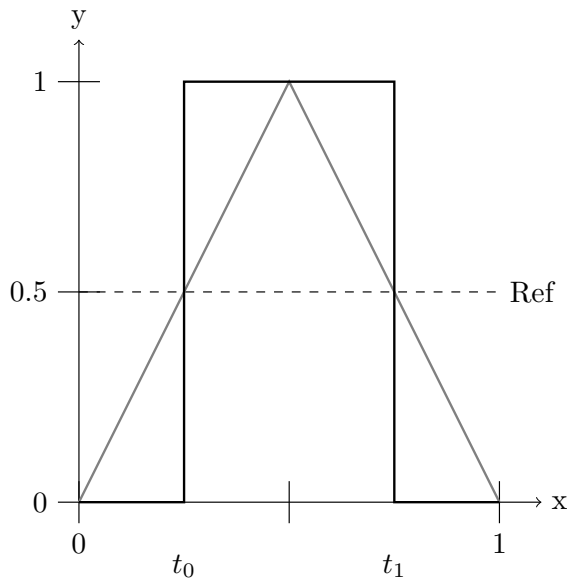

Figure 3.4: PWM technique applied to DC/DC converters.

the oscillation attenuates,

- $\mathbf{1}(t)$ represents the unit step function (also known as the Heaviside function).

In general, DC/DC converters allow the control of the output DC voltage through adjustments to the duty cycle of a rectangular waveform [34]. This is typically achieved by comparing a triangular function with a reference level which is proportional to the desired output voltage, as shown in Fig. 3.4. The intersection points of these signals determine the switching times t_0 (switch-ON) and t_1 (switch-OFF), which control the pulse width and, consequently, the output voltage. In a PE converter, such as the one shown in Fig. 3.5, it is assumed that the output voltage is regulated using a PWM technique with a switching frequency f_{sw} and a duty cycle $0 < d < 1$.

The full bridge converter (or H-bridge), shown in Fig. 3.5, consists of four switches that switch-ON in pairs (S_1 with S_4 and S_2 with S_3), resulting in a rectangular voltage at the middle point of each bridge leg [2]. The voltage transitions from $+V_{dc}$ to $-V_{dc}$. For a half cycle (period), $0 < t < \frac{T}{2}$, a

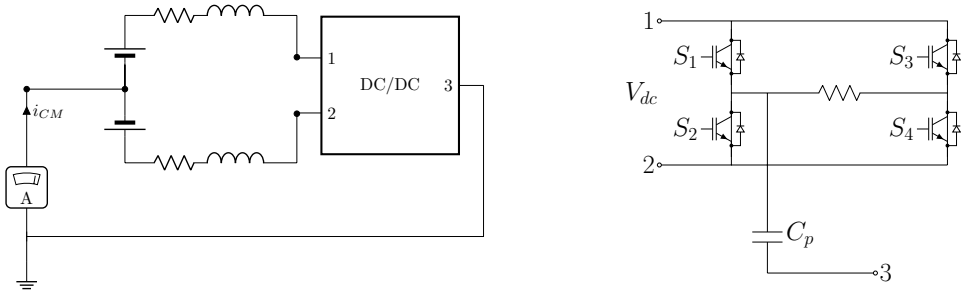

Figure 3.5: Single DC/DC converter consisting of a full-bridge converter with an asymmetric parasitic capacitance C_P to ground.

positive $\frac{dv}{dt}$ occurs across the parasitic capacitance C_p, while during the other half cycle (period), $\frac{T}{2} < t < T$ a negative $\frac{dv}{dt}$ occurs, resulting in either $i^{+}_{\mathrm{CM}}(t)$ or $i^{-}_{\mathrm{CM}}(t)$. Consequently, during a first switching-ON event, a rising current $i^{+}_{\mathrm{CM}}(t)$ is induced, while the complementary switching-ON event results in a falling current $i^{-}_{\mathrm{CM}}(t)$. These currents are time-shifted with respect to each other by the duty cycle times period $\frac{d}{f_{\mathrm{sw}}}$ and have opposite polarities. For a switching instant $l \in \mathbb{N}$ those currents can be mathematically represented by

$$i^{+}_{\mathrm{CM}}(t) = i\left(t - \frac{l}{f_{\mathrm{sw}}}\right), \tag{3.3}$$

$$i^{-}_{\mathrm{CM}}(t) = -i\left(t - \frac{l+d}{f_{\mathrm{sw}}}\right) = -i^{+}_{\mathrm{CM}}\left(t - \frac{d}{f_{\mathrm{sw}}}\right). \tag{3.4}$$

The total CM current is given by summing $i^{+}_{\mathrm{CM}}(t)$ and $i^{-}_{\mathrm{CM}}(t)$ (the oscillatory mode currents induced by rising and falling slopes of the PWM voltage) and can be expressed as

$$i_{\mathrm{CM}}(t) = \sum_{l=-\infty}^{\infty}\left(i\left(t - \frac{l}{f_{\mathrm{sw}}}\right) - i\left(t - \frac{l+d}{f_{\mathrm{sw}}}\right)\right). \tag{3.5}$$

A typical CM current shape with damped oscillation is shown in Fig. 3.6. This current was obtained from a Simulink simulation of a setup comprising

up to eight identical converters operating simultaneously. The zoom plot shows the waveform of the CM current from a single converter, switched at time $t_1 = 0$. Similarly, Fig. 3.7 shows the CM current measured from a real setup consisting of three half-bridge evaluation board converters (M100002230 CoolGaNTM e-mode HEMT [66]) based on GaN MOSFET technology. The measurement shows the CM current from a single converter. The following section presents an expression for the CM current in the FD.

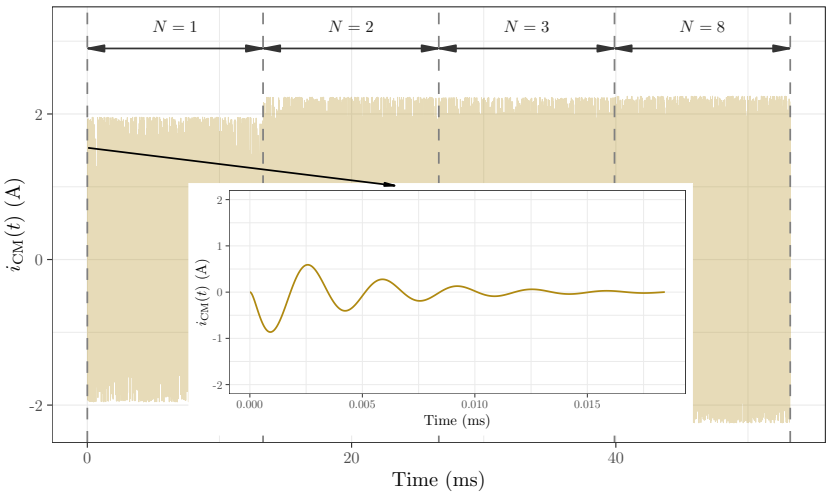

Figure 3.6: Simulated CM current waveform showing damped oscillations for a single converter within an eight-converter Simulink model.

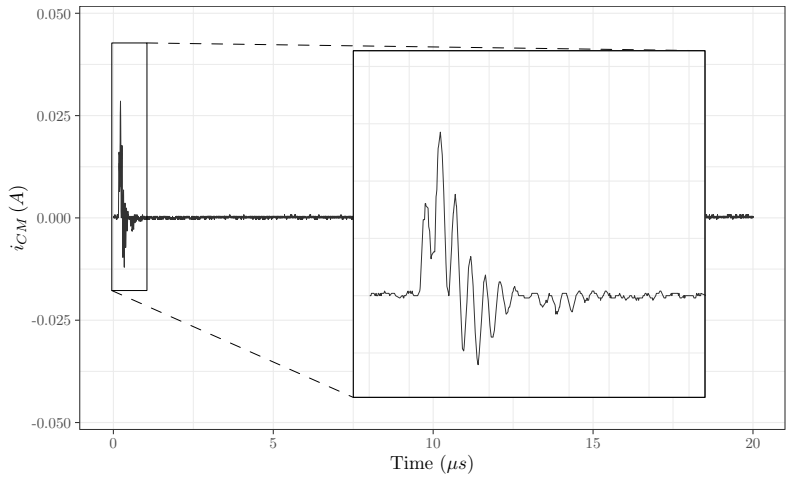

Figure 3.7: Measured CM current waveform exhibiting damped oscillations in a half-bridge evaluation board.

3.3.2 Frequency Domain

In order to consider the CM current in the FD, the Fourier Transform (FT) should be used. To facilitate the analysis in the FD, two keys assumptions regarding the CM current are made:

1. only the rising portion of the CM current is considered (if referred to the PWM, this corresponds to a falling PWM edge). In Fig.3.8, the rising portion of CM current under consideration is indicated by the purple rectangle. As the two currents, $i^{+}_{\mathrm{CM}}(t)$ and $i^{-}_{\mathrm{CM}}(t)$, are shifted with respect to each other by a duty cycle times the period $\dfrac{d}{f_{\mathrm{sw}}}$;
2. the current exhibits periodic properties within time intervals of length $1/f_{\mathrm{sw}}$ and it is assumed to be in steady state.

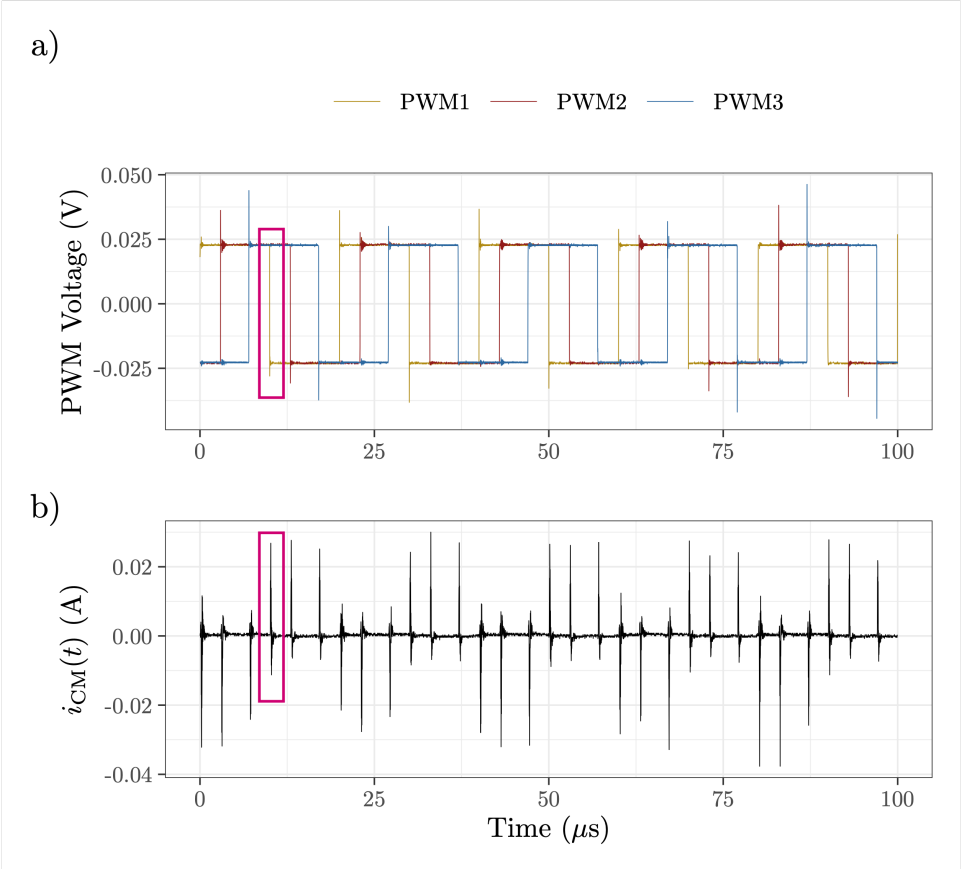

Figure 3.8: Time-domain representations: a) PWM signals and b) CM current, with the rising portion of the CM current highlighted in purple.

Building upon the first assumption, in the case of a single PE converter operating in steady-state, both the rising and falling currents, $i^{+}_{\mathrm{CM}}(t)$ and $i^{-}_{\mathrm{CM}}(t)$ become repetitive, as does $i_{\mathrm{CM}}(t)$. Consequently one can express the h-th harmonic of of the switching frequency of the total rising current $I^{+}_{\mathrm{CM}}[h] = \mathcal{F}\{i^{+}_{\mathrm{CM}}(t)\}$ as [67]:

$$I^{+}_{\mathrm{CM}}[h] = f_{\mathrm{sw}} \int_{0}^{1/f_{\mathrm{sw}}} i^{+}_{\mathrm{CM}}(t) e^{-\mathbf{j}2\pi f_{\mathrm{sw}} h t} \, \mathrm{dt}, \tag{3.6}$$

which upon analytical integration yields to the following solution:

$$I^{+}_{\mathrm{CM}}[h] = \frac{i_0 \omega f_{\mathrm{sw}}}{(\lambda + \mathbf{j}2\pi f_{\mathrm{sw}} h)^2 + \omega^2}. \tag{3.7}$$

Moreover, the FT exhibits two properties: linearity and time-shifting. The latter property demonstrates that a time shift in a signal results in a corresponding phase adjustment in its FT. These properties can be used to express the total current generated by a single converter as:

$$\begin{aligned} I_{\mathrm{CM}}[h] &= I^{+}_{\mathrm{CM}}[h] + I^{-}_{\mathrm{CM}}[h] \\ &= I^{+}_{\mathrm{CM}}[h]\left(1 - e^{\mathbf{j}2\pi d f_{\mathrm{sw}} h}\right). \end{aligned} \tag{3.8}$$

Consider a system with N converters, where the CM current in each is identical, but offset in time. The total CM current generated by these N converters can be expressed by assuming that the first converter is switched-ON at $\tau_1 = 0$, while the subsequent $N-1$ converters are activated at $\tau_2, \ldots, \tau_N$, respectively. The total current $I_N[h]$ generated by N converters is thus formulated as:

$$\begin{aligned} I_N[h] &= I_{\mathrm{CM}}[h] \sum_{k=1}^{N} e^{-\mathbf{j}2\pi f_{\mathrm{sw}} \tau_k h} \\ &= I_{\mathrm{CM}}[h] \left(1 + \sum_{k=2}^{N} e^{-\mathbf{j}2\pi f_{\mathrm{sw}} \tau_k h}\right). \end{aligned} \tag{3.9}$$

It is worth noting that (3.9) consists of two components:

- $I_{\mathrm{CM}}[h]$ which represents the CM current generated by a single converter, disregarding any time shift;
- $1 + \sum_{k=2}^{N} e^{-\mathbf{j}2\pi f_{\mathrm{sw}} \tau_k h}$ which accounts for the the contribution due to time shifts; the 1 represents the first PE converter's contribution with zero phase delay ($t_1 = 0$).

In the case where all the converters are activated at the same time, i.e., $\tau_1 = \ldots = \tau_N = 0$, the total current becomes $I_N[h] = I_{\mathrm{CM}}[h]N$. With τ_1

fixed and variables $\tau_2, \ldots, \tau_N$ changing, the notation $Z_N[h]$ is introduced to denote the $\sum_{k=2}^{N} e^{-\mathrm{j}2\pi f_{\mathrm{sw}} \tau_k h}$. Therefore, (3.9) can be expressed as:

$$I_N[h] = I_{\mathrm{CM}}[h]\,(1 + Z_N[h])\,. \tag{3.10}$$

The vector $Z_N[h]$ represents the contributions to the total current $I_N[h]$ with respect to the first converter, generated by converters 2 to N. In Fig. 3.3, the solid vector represents $Z_N[h]$ for 3 converters. Please note, this means that there are 4 converters operating simultaneously: the reference converter with $\tau_1 = 0$ and 3 additional converters with $\tau_2, \tau_3, \tau_4 > 0$. Each of the converters for $\tau_i > 0$ is represented by the coloured dashed-line vectors of length 1.

3.4 Kluyver's Solution to Pearson's Random Walk

From the previous section, the CM current model in a multi-converter setup is expressed by (3.10). In this model, the vector $Z_N[h]$ represents the contributions to the total current $I_N[h]$ with respect to the first converter, generated by converters 2 to N. However, the first converter still contributes to the overall CM current with a value of 1. Fig. 3.3, illustrates $Z_N[h]$ as a solid vector for three converters. Please note, this means that there are four converters operating simultaneously: the reference converter with $\tau_1 = 0$ and three additional converters with $\tau_2, \tau_3, \tau_4 > 0$. Each of the converters for $\tau_i > 0$ is represented by the coloured dashed-line vectors of length 1.

The vector $Z_N[h]$ represents the summation contributions to the CM cur-

rent value generated by each of the operating 2 to N converters. The lengths of the vectors composing $Z_N[h]$ are identical (equal to 1), while the phase angles are random variables with uniform distributions $U(0, 2\pi)$. The resultant vector $Z_N[h]$ shows two properties:

1. a random variable *length (or magnitude)* of a certain distribution, which will be determined and discussed in this thesis,
2. a random *direction* of a uniform distribution $U(0, 2\pi)$

Since $Z_N[h]$ represents the sum of unit vectors $e^{-\mathbf{j}2\pi f_{\mathrm{sw}}\tau_k h}$, with direction following a uniform distribution $U(0, 2\pi)$, these characteristics allow the association of the PE converters behaviour with the problem stated by Pearson. This analogy between the Pearson's Random Walk and the random switching-ON of several PE converters introduces a new approach to electromagnetic emissions modelling in PE systems. Regarding Pearson's original question, concerning the distribution of $|Z_N[h]|$, Jan Kornelis Kluyver provided a solution in [68], expressing the cumulative distribution function (cdf) of $|Z_N[h]|$ as:

$$P(|Z_N[h]| \leq r) = \int_0^\infty r J_0(t)^{N-1} J_1(rt)\ \mathrm{d}\, t, \tag{3.11}$$

where

- J_0 is the Bessel function of order 0,
- J_1 is the Bessel function of order 1.

This solution will be verified in Chapter 5 through comparison with 1,000 and both 1,000 and 4,000 experimental measurements, evaluating the **ecdf** from real data against Kluyver's theoretical **cdf**.

Furthermore, as the solution proposed by Kluyver utilises Bessel's functions, which exhibit recursive properties, the above integral (3.11) can be used to derive the **probability density function (pdf)** of $|Z_N[h]|$, which will be described in Section 5.3. Indeed, differentiating the **cdf** from (3.11) yields:

$$p_N(r) = r \int_0^\infty t J_0(t)^{N-1} J_0(rt)\,\mathrm{d}\,t. \tag{3.12}$$

3.5 Conclusion

This chapter presented a historical overview of "Random Walk" and its use diverse applications, introducing Pearson's Random Walk based on Karl Pearson's 1905 inquiry. The rationale for applying Pearson's Random Walk to PE converter modelling was discussed as well.

In addition, this chapter addressed the following aspects:

- The analogy between Pearson's Random Walk and modelling of the emissions of PE converters through a diagram with vectors representing the CM current I_{CM} (at a harmonic h) produced by power converters;
- TD analysis of CM current in PE converters. The CM current was modelled as a damped oscillation signal, and a mathematical expression in the TD was provided;
- FD analysis of CM current, focusing on a harmonic of the switching frequency;
- Proposal of CM current aggregation model expressed as ($I_N[h] =$

$I_{\mathrm{CM}}[h](1 + Z_N[h])$;

- Analysis of vector $Z[h]$, addressing Pearson's distribution question through Kluyver's solution;
- Derivation of the **pdf** for subsequent analysis, including EMI reduction probability in multi-converter configurations compared with single-converter setups.

In summary, this chapter introduced Pearson's Random Walk concept and established an analogy to multiple PE converters electromagnetic behaviour; provided a mathematical model for CM current in multi-converter setups; and discussed Kluyver's solution for the distribution of the contributions ($Z[h]$) to the emission levels (interference) generated by multiple PE converters. The next chapter discusses a methodology to verify the model proposed in this chapter and presents some preliminary results regarding the validity of Pearson's Random walk in modelling multiple PE converters.

Chapter 4

Verification Methodology for Pearson's Random Walk Model

The previous chapter introduced the mathematical framework of Pearson's Random Walk (PRW) for modelling PE converters. The CM current was identified as the quantity of interest, being a primary source of EMC issues. The aim was to propose a model (Pearson's Random Walk) that would express the CM current, at a harmonic h (e.g., of the switching frequency), produced by N converters by referring it to the CM current generated by a single converter. This model then incorporates the contributions due to time shifts to the total current $I_N[h]$ with respect to the first converter, generated by 2 to N converters. This current was examined in both the time and frequency domains. A mathematical expression for Pearson's model was then presented in the frequency domain for the total current generated by N converters operating simultaneously, as shown in (3.9) which is here

recalled again,

$$
\begin{aligned}
I_N[h] &= I_{\mathrm{CM}}[h] \sum_{k=1}^{N} e^{-\mathbf{j}2\pi f_{\mathrm{sw}} \tau_k h} \\
&= I_{\mathrm{CM}}[h] \left(1 + \sum_{k=2}^{N} e^{-\mathbf{j}2\pi f_{\mathrm{sw}} \tau_k h} \right).
\end{aligned}
\tag{4.1}
$$

Building upon the introduction of PRW model in the previous chapter, this chapter discusses a methodology to verify it. The verification methodology relies on two approaches:

1. A simulation consisting of eight identical converters, each connected to an individual DC source (if a single source is used, the current path remains uncertain unless all converters have identical impedances);
2. An experiment in which a setup consisting of 3 DC/DC converters is used.

In this chapter the verification of the methodology with some preliminary results will be presented whereas the statistical results of both simulation and experiments will be presented in the following chapter.

4.1 Simulation-Based Verification

4.1.1 Simulation setup

The simulation setup consists of eight identical DC/DC converters, as illustrated in Fig. 4.1. Each converter is characterised by specific impedance parameters, represented by inductive-resistive elements with values of $L = 6.28\,\mu\text{H}$ and $R = 0.01\,\Omega$. The resistive-inductive elements represent an approximation of the parasitic components in both the converter and its connecting bus bars. These parasitic elements interact with the converter's parasitic capacitance to produce oscillations. Specifically, the introduced inductive parasitic components generate the characteristic ringing effect. Moreover, for the sake of simplicity, each converter is modelled as a basic full-bridge converter with a load resistor $R = 47\,\Omega$ and an arbitrary parasitic capacitor of value $C_p = 467\,\mu\text{F}$, as shown in Fig. 4.1 (b). The inclusion of this capacitor accounts for the parasitic capacitance arising from the proximity of circuit elements to the metallic enclosure, creating a path for the CM current to flow. The choice of a relatively large parasitic capacitance was intentional, aimed at allowing simple initial verification of Pearson's Random Walk model. Indeed, the presence of a large capacitor allows a measurable current to flow through the capacitor. It should also be noted that this method remains valid for more 'realistic' metallic enclosure capacitance values (typically ranging from tens to hundreds of picofarads), as the focus is on the damped oscillations of the CM current. Considerations of the frequency-dependent reactance formula for capacitors demonstrate an inverse relationship between capacitance and reactance: a larger capacitor results in a lower reactance, meaning that the capacitor permits more current to flow. This concept has been verified experimentally. In the simulation, the CM current is measured at a common coupling

point, as indicated in Fig. 4.1 (a).

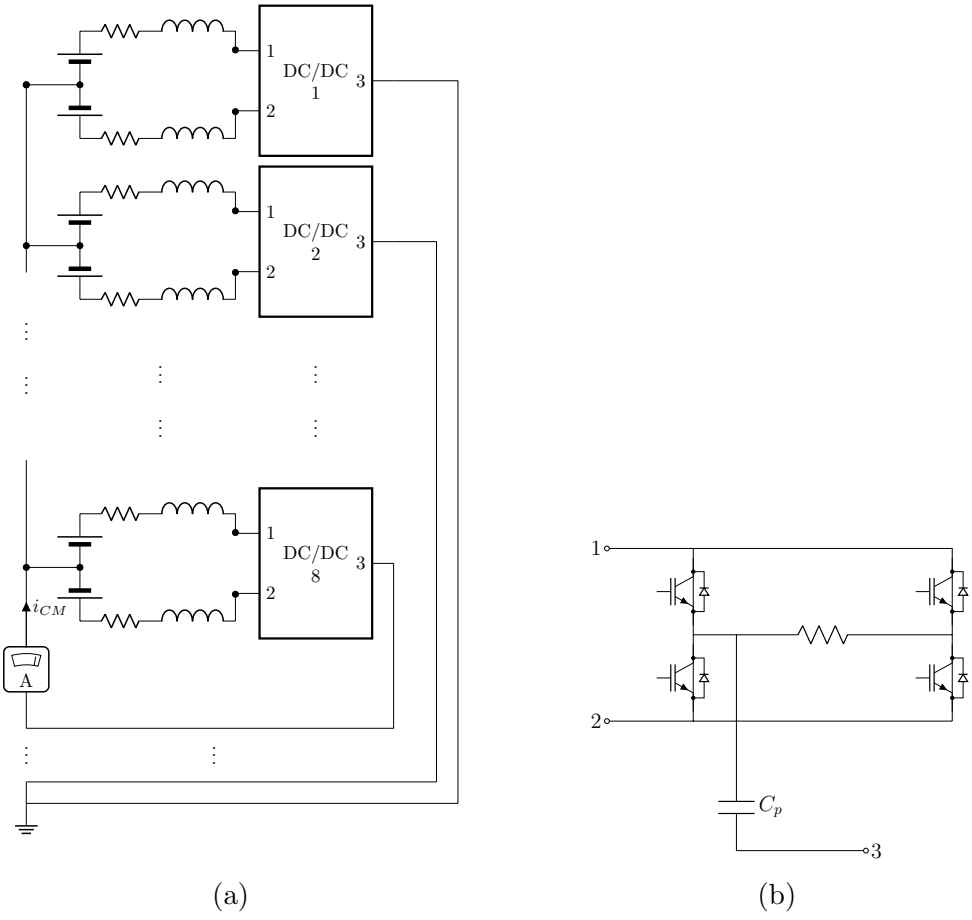

(a) (b)

Figure 4.1: Simulation setup: (a) overall simulation setup consisting of 8 identical DC/DC converters. (b) single DC/DC converter structure showing full bridge topology and an asymmetric parasitic capacitance (C_p).

4.1.2 Simulation procedure

The simulation procedure is carried out under the assumption that all eight converters have identical characteristics (although realistically, they would be similar rather than identical). A switching frequency of $f_{\text{sw}} = 20\,\text{kHz}$ is selected for verification. The model holds regardless the choice of the switching frequency, therefore other frequencies could be used depending on the specific application of the power converter. Additionally, the simulations were carried out using MATLAB Simulink and the Simscape Spe-

cialized Power Systems Toolbox. The sampling frequency of the solver, F_s, was set to 276 MHz with a fixed time step ($1/F_s$). This sampling value was selected to satisfy the Nyquist-Shannon sampling theorem, which states that to capture a signal accurately, the sampling rate must be at least twice the frequency of the highest frequency component in that signal. In the proposed simulation procedure, the sole variable under control is the switching-ON time t_k of the k-th converter where $k = 1, \ldots, N$ and N denotes the number of converters. For each converter k, where $k = 1, \ldots, N$ the time t_k is defined as:

$$t_k = (k-1)\Theta T_{\text{sw}} + \tau_k, \tag{4.2}$$

where:

- Θ is an arbitrary constant set to 266 which controls the staggered switch-ON of N converters;
- $\tau_k \in [0, T_{\text{sw}})$ is a randomly chosen time constant ensuring a random phase shift between harmonic h in each converter.

The value of $\theta = 266$ allows sufficient settling time for any newly introduced converter. By definition $t_1 = \tau_1 = 0$. A correspondence exists between a random phase angle $\alpha_k = \arg(e^{-\mathrm{j}2\pi f_{\text{sw}} \tau_k h})$ and the time instant τ_k, for $k = 2, \ldots, N$. Indeed, selecting the time instant τ_k from a uniform distribution $\mathcal{U}(0, T_{\text{sw}})$ corresponds to drawing an angle α_k from a uniform distribution $\mathcal{U}(0, 2\pi)$, and vice versa.

The simulation process was carried out through the following steps:

1. Saving the CM current (i_{CM}) and the time (t) from each simulation;

2. Segmenting the data into bins such that $t \in [(k-1)\Theta T_{\text{sw}}, k\Theta T_{\text{sw}})$, representing the periods during which exactly k converters operate simultaneously, where $k = 1, \ldots, N$;

3. For each bin k, filtering the data for $t > ((k-1)\Theta + 2)T_{\text{sw}}$, and, performing FFT transformation of i_{CM} for the remaining $\Theta - 2$ periods. The data is filtered in this manner, disregarding the first 2 periods, to ensure that precisely N converters are switched-ON;

4. Collecting the harmonic values $I_k[h]$ of the switching frequency f_{sw} for k converters operating simultaneously with $k = 1, \ldots, N$.

The simulations were performed using a Lenovo personal computer with an Intel(R) Xeon(R) W-2123 CPU operating at 3.60 GHz, featuring four cores and eight logical processors, running Windows 10. Each simulation initially required approximately 10 minutes, amounting to 170 hours (7 days) for a complete set of 1,000 simulations on a single machine. To reduce computation time, the simulations were parallelised across two identical personal computers, with 500 simulations allocated to each.

In addition, it was decided to compare the results for $N = 3, 5, 8$ converters. Instead of running simulations where

$$t_k = (k-1)\Theta T_{\text{sw}} + \tau_k, \tag{4.3}$$

for each $k = 1, \ldots, 8$, it was assumed that:

$$t_k = s_k \Theta T_{\text{sw}} + \tau_k, \tag{4.4}$$

where:

- $s_1 = 1$ (the reference converter);

- $s_2 = s_3 = 2$ (three converters operating simultaneously);
- $s_4 = s_5 = 3$ (five converters operating simultaneously);
- $s_6 = s_7 = s_8 = 4$ (eight converters operating simultaneously).

Hence, instead of 8 bins with $\Theta = 266$ switching periods each, 4 bins were created, which allowed to further reduce the time of the simulations by approximately a quarter, i.e. to around 2 days.

Following the simulation procedure outlined above, the next subsection will describe a method to verify the validity ofPRW model.

4.1.3 Preliminary Results: Deterministic Verification

This subsection outlines a method to test Pearson's Random Walk Model. The central concept underlying Pearson's model is the notion of a random walk, which creates vectors in different directions, similar to the unpredictable steps of a drunk person who would take a step in one direction, then a second step in an other direction and so on and so far. This walk generates vectors with specific angles. The aim in this subsection is to check if this concept can be used to model the behaviour of multiple converters. The assumption is that the angle of the vector can be chosen to represent the switching-ON time (or phase) of the converter, and that vectors chosen in such a way create a path which corresponds to a unique pattern of emissions.

To verify this idea, a point $Z[h]$ is chosen, representing a certain level of interference. The question arises: can this point $Z[h]$ be reached through different paths? The added value of considering different paths is to double check how converters can be switched-ON in a pseudo-random fashion.

Once a path to the point is chosen, the corresponding switching-ON times for the converters are obtained. The goal is to confirm that the switching-ON order of the converters matches the initially selected path. By comparing the converter's switching-ON sequence with the initially chosen path, it can be assessed whether Pearson's Random Walk model correctly represents how multiple converters behave when switched-ON in a seemingly random order.

Summing up, the objective may be formulated as follows:

- Consider a scenario wherein a specific maximum interference level is to be achieved, which means selecting a point $Z[h]$ in the complex plane;
- The model stipulates that the total CM current generated by N converters, $I_N[h] = I_{\mathrm{CM}}[h]\,(1 + Z_N[h])$, where the CM current of a single converter is known. It becomes possible to modify the contributions due to time shifts to the total current $I_N[h]$ with respect to the first converter, generated by 2 to N converters, expressed as $\sum_{k=2}^{N} e^{-\mathbf{j}2\pi f_{\mathrm{sw}} \tau_k h}$;
- The subsequent investigation aims to verify the model's prediction that if the converters are switched-ON through different switching-ON patterns, a maximum level of predicted interference can be reached. In mathematical terms, this translates to identifying different paths of vectors terminating at the same point $Z[h]$ in the complex plane.

Therefore, to verify this idea, the following approach was developed and implemented:

1. For a selected harmonic $h' \in \{1, 2, \ldots\}$, several points $Z^{(1)}[h'], \ldots, Z^{(p)}[h'] \in \mathbb{C}$ were arbitrarily chosen, where $|Z^{(l)}[h']| = R$ is fixed for each $l = 1, \ldots, p$ and $R \leq N - 1$. This ensures that all the arbitrarily chosen points $Z^{(l)}[h']$ lie on the circle of radius R as shown in Fig. 4.2.

   Fixing R is equivalent to selecting a circle with a certain radius and choosing a random point along its circumference. The rationale for fixing the radius R is to facilitate the manipulation of time instants (through different vectors, and this will be shown in the next point) for switching-ON the converters. The idea is that of inputting these time instants into the simulation, then extracting the time instants from the simulation itself, and finally comparing these extracted time values with the initially chosen ones.

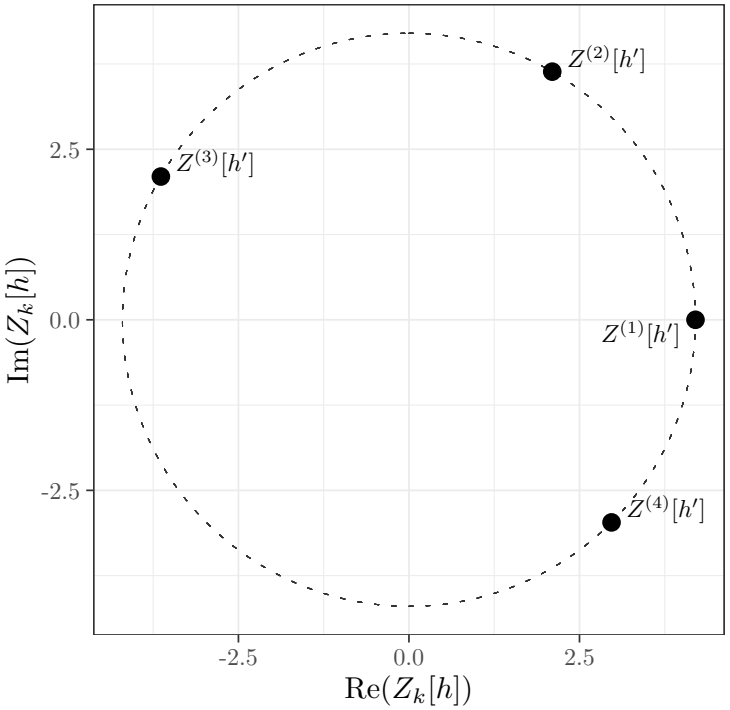

Figure 4.2: Visual representation of the applied verification methodology for Pearson's Random Walk model. Different points $Z^{(l)}[h]$ can be selected and represent the contributions due to time shifts to the total current $I_N[h]$ with respect to the first converter. These contributions are part of the interference.

2. For a selected point $Z^{(l)}[h']$, K sequences of N vectors $v_1^{(j)}, \ldots, v_N^{(j)} \in \mathbb{C}$ were constructed, such that

$$v_1^{(j)} + \ldots + v_N^{(j)} = Z^{(l)}[h'],$$
$$v_1^{(j)} = 0 + \mathbf{j}0,$$
$$\left|v_2^{(j)}\right| = \ldots = \left|v_N^{(j)}\right| = 1,$$

where each $j = 1, \ldots, K$ represents a distinct path to reach the selected point.

These K sequences represent K distinct paths or configurations of unit vector that sum to the point $Z^{(l)}[h']$, and are equivalent to random walks.

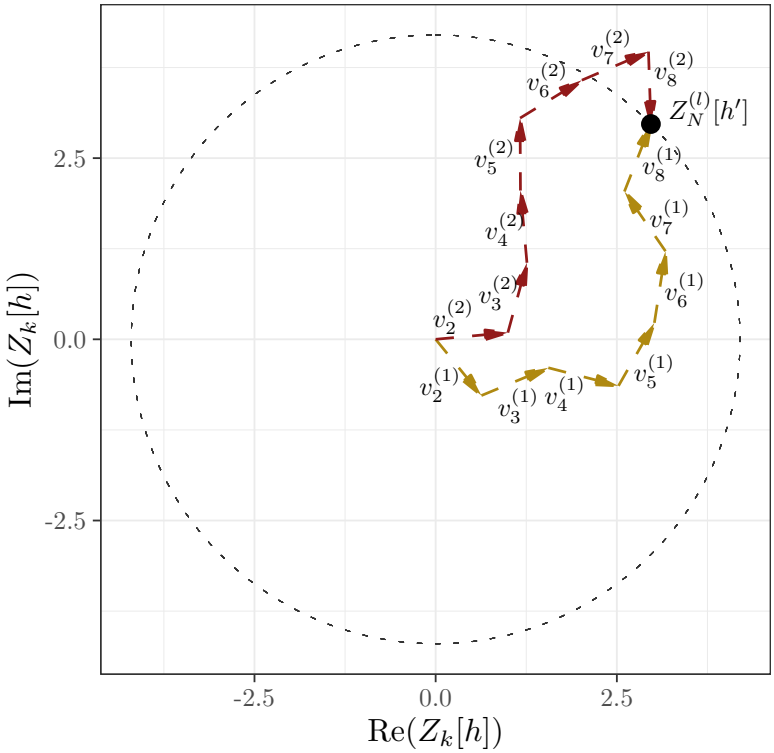

Figure 4.3: Visual representation of the applied verification methodology for Pearson's Random Walk model, utilising $K = 2$ paths, $N = 8$ converters, $R = 4.2$, $h' = 1$, and $Z^{(l)}[h] = 4(\frac{\sqrt{2}}{10} + \mathbf{j}\frac{\sqrt{2}}{10})$. It illustrates the selected theoretical vectors $v_1^{(j)}, \ldots, v_8^{(j)}$.

In Fig. 4.3, a point $Z_N^{(l)}[h']$ is chosen and two paths are selected to reach that point to demonstrate that converters can be activated using different patterns. In the next point, the angles of the vectors displayed in the picture, $\alpha = \arg\left(v_k^{(j)}\right)$, will be used to compute the time constants $\tau_k^{(j)}$ to be input to the simulation.

3. For each $j = 1, \ldots, K$ and $k = 1, \ldots, N$ the time constant $\tau_k^{(j)}$ was obtained via

$$\tau_k^{(j)} = -\frac{\arg\left(v_k^{(j)}\right)}{2\pi f_{\text{sw}} h'} \bmod \frac{1}{f_{\text{sw}} h'}, \tag{4.5}$$

where mod is the modulo operator.

$\tau_k^{(j)}$ is derived from (4.5) as the vector $v_k^{(j)}$ is expressed as a complex number in polar form $v_k^{(j)} = e^{-\mathbf{j}2\pi f_{\text{sw}} \tau_k^{(j)} h}$. These time constants $\tau_k^{(j)}$ are then input into the simulation. This concept is illustrated in Fig. 4.4. That is the switching time $\tau_k^{(j)}$ is used in the simulation to switch-ON the k-th converter.

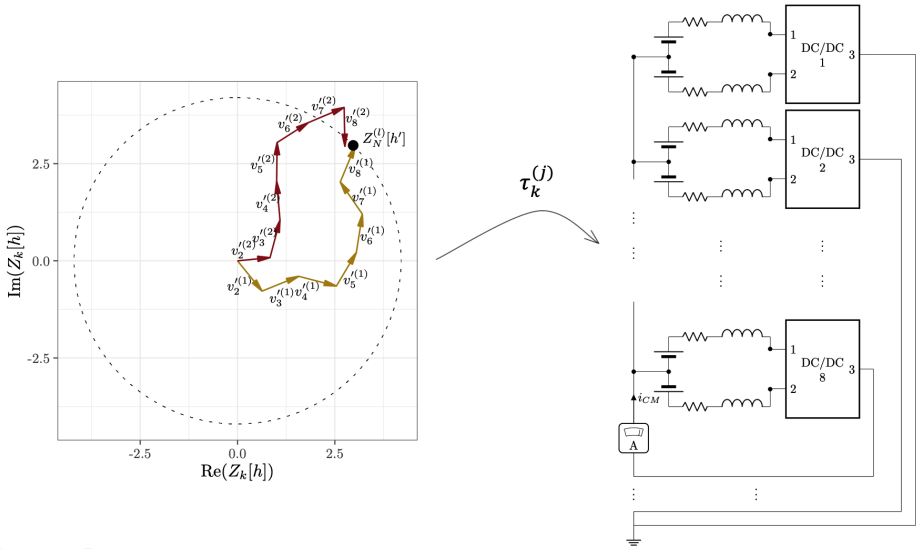

Figure 4.4: From the initially selected vectors $v_1^{(j)}, \ldots, v_8^{(j)}$, the time instants $\tau_k^{(j)}$ are calculated and used as inputs to the simulation setup for activating the converters.

4. Each sequence $\tau_1^{(j)}, \ldots, \tau_N^{(j)}$ was used to simulate the setup described in Section 4.1.1.

   To allow sufficient settling time, each converter operates for $\theta = 266$ periods before the next converter switches-ON. Fig. 4.5 presents the results of the time-domain MATLAB simulation. The CM current is divided into bins corresponding to one through eight simultaneously operating converters. The upper facet ($j = 1$) presents results for converters activated according to time delays obtained from the first path of vectors (golden), as described in point 2 and illustrated in Fig. 4.3. The lower facet ($j = 2$) presents the CM current for converters activated according to time delays obtained from the second path of vectors (red). Additionally, Fig. 4.5 illustrates the time delay $\tau_2^{(1)}$ which was derived from vector $v_2^{(1)}$.

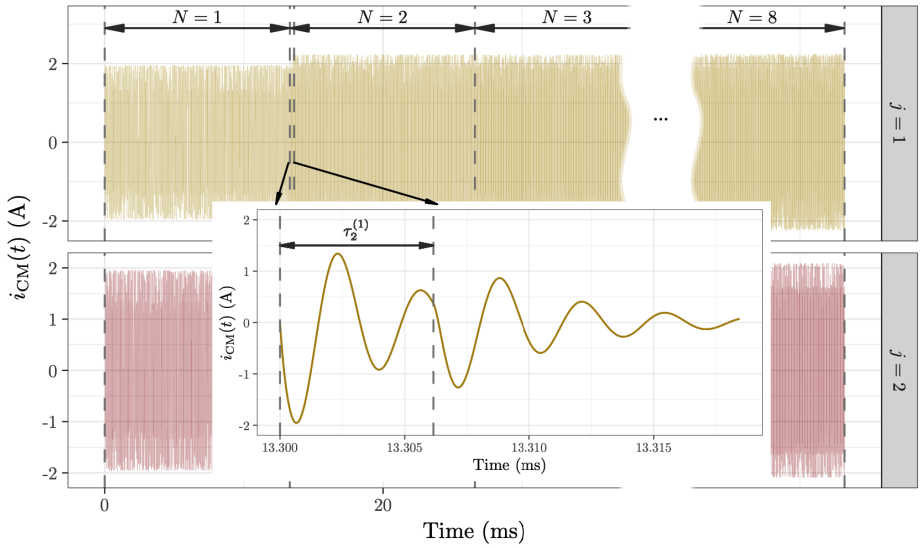

Figure 4.5: CM current for one to eight converters activated according to time delays obtained from the paths shown at point 2. Additionally, the time delay $\tau_2^{(1)}$ obtained from vector $v_2^{(1)}$ is indicated.

5. The simulation results, i.e. values $I_k[h]$, were post-processed to obtain the vector $Z^{(l)}[h]$ and the individual vectors $v'^{(j)}_1, \ldots, v'^{(j)}_N \in \mathbb{C}$ that sum to $Z^{(l)}[h]$ and correspond to the sequence of unit vectors $v^{(j)}_1, \ldots, v^{(j)}_N$.

   The CM current bins from the previous point are post-processed via FFT to obtain the frequency spectra (harmonics) of the CM current with N converters as shown in Fig 4.6.

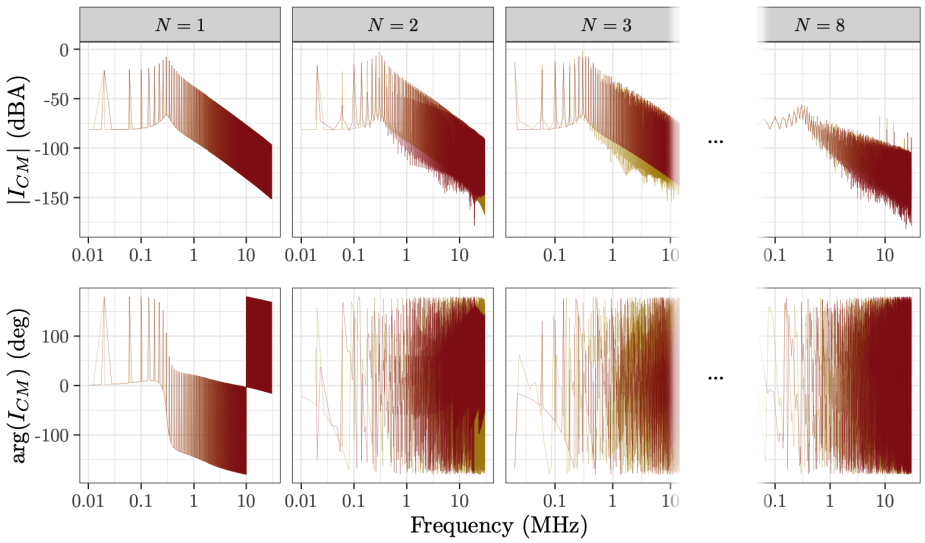

Figure 4.6: Spectra obtained from the CM current for one to eight converters, that is from each of the bins shown in the point 4.

Complex vectors $Z^{(l)}_N[h]$ are then obtained by rearranging Eq. (3.10). For instance, with two converters, the vectors are obtained as follows:

$$\begin{aligned} I_2[h] &= I_{\mathrm{CM}}[h]\,(1 + Z_1[h])\,, \\ \frac{I_2[h]}{I_{\mathrm{CM}}[h]} - 1 &= Z_1[h] = v'^{(j)}_1. \end{aligned} \tag{4.6}$$

For three converters, the following relationship holds:

$$\begin{aligned} \frac{I_3[h]}{I_{\mathrm{CM}}[h]} - 1 = Z_2[h] = v_1'^{(j)} + v_2'^{(j)}, \\ \frac{I_3[h]}{I_{\mathrm{CM}}[h]} - 1 - v_1'^{(j)} = v_2'^{(j)}, \end{aligned} \tag{4.7}$$

and so on so far for the remaining vectors.

Finally, these vectors, shown in Fig. 4.7, are compared with the originally selected paths to assess the alignment between the theoretical model and the results obtained from the simulations while the preliminary results obtained from the experiment will be discussed in the following section.

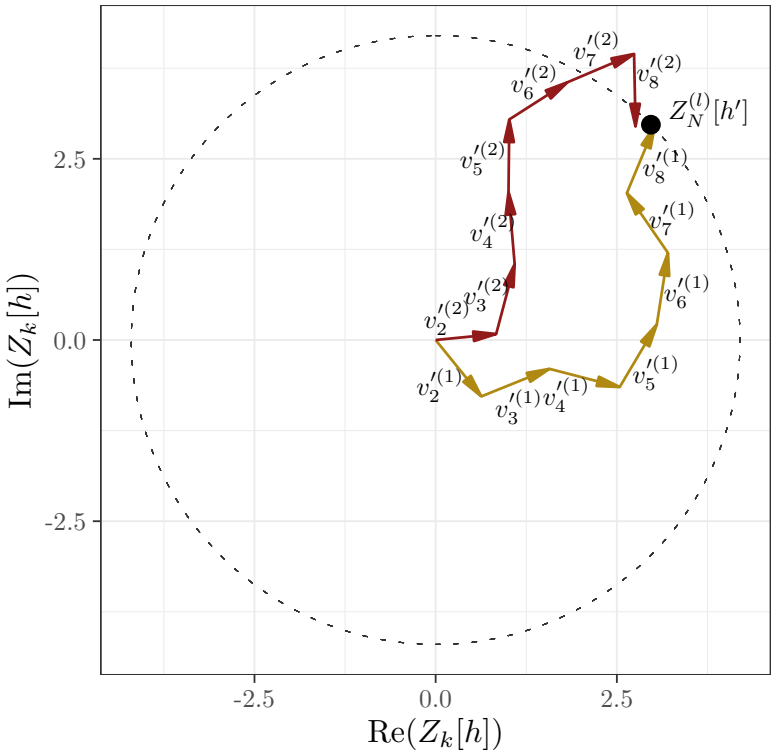

Figure 4.7: The vectors $v_1'^{(j)}, \ldots, v_8'^{(j)}$ are estimated for $h = 1$ using the frequency-domain data and have to be juxtaposed to the initially selected vectors, $v_1^{(j)}, \ldots, v_8^{(j)}$.

Comparison in the complex domain

Fig. 4.8 presents four distinct paths for the 1st, 5th and 101st harmonics, respectively. Points $Z^{(1)}[h']$ and $Z^{(2)}[h']$ were selected for $h' = 1$, i.e. to impose agreement for the 1st harmonic. The dashed lines represent vectors $v_2^{(j)}, \ldots, v_8^{(j)}$ initially chosen from the Pearson's model (theoretical), while continuous lines represent vectors $v'^{(j)}_2, \ldots, v'^{(j)}_8$ obtained from the circuit simulation, for $j = 1, \ldots, 4$. As it can be seen, imposing agreement on the first harmonic, leads to an agreement for further harmonics, extending at least to the depicted 101st harmonic.This comparison demonstrates that the summation model proposed in (3.10) is valid. The subsequent section will present verification against experimental data.

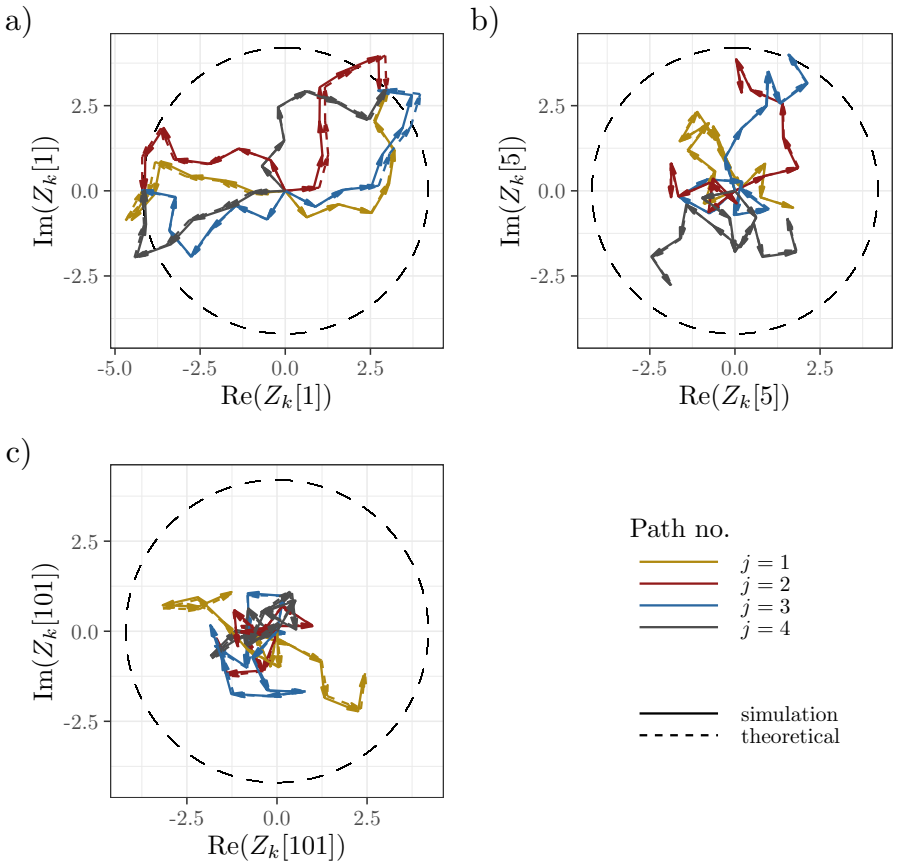

Figure 4.8: The sequences $v_1^{(j)}, \ldots, v_N^{(j)}$ and $v'^{(j)}_1, \ldots, v'^{(j)}_N$ obtained, respectively from Pearson's model and the circuit simulation for a) $Z[1]$, b) $Z[5]$, c) $Z[101]$ with $h' = 1$, $N = 8$, and $R = 0.6(N - 1)$.

4.1.4 Summary

This section established a methodology to verify the summation model proposed in (3.10), through the implementation of a simulation setup and procedure. The foundation of this approach lay in the random walk concept underlying Pearson's model. The analogy of a random walk of a drunk man, who takes a step in one direction and then in another direction, was applied to electrical engineering to describe the behaviour of multiple PE converters. Specifically, vectors (or vector angles) and vector paths analogous to random walk trajectories were employed to represent converter switching-ON times. The objective was to verify that the converter switching-ON sequence, represented by a specific vector path, matched the initially selected vector path from which the switching instants were derived and subsequently implemented in the simulation.

The verification procedure was described for $K = 2$ paths, $N = 8$ converters, an arbitrary chosen radius $R = 4.2$, and a point $Z^{(l)}[h] = 2(\frac{\sqrt{2}}{5} + \mathbf{j}\frac{\sqrt{2}}{5})$ through the following steps:

- Several paths representing random walks are selected to reach a point $Z[h]$ representing a certain level of interference;
- From the vectors constituting these paths, the time instants τ_k corresponding to the angles of the respective vectors are derived using (4.5);
- These time instants are fed into the simulation setup for converter activation;
- The CM current is measured, and the time-domain data is segmented into bins, each corresponding to N converters operating simultaneously;

- These bins undergo post-processing via FFT to obtain the harmonics of the CM current with N converters. Complex vectors $Z_N^{(l)}[h]$ are then obtained by rearranging (3.10);
- Finally, these vectors are juxtaposed to the originally selected paths to assess the alignment between the theoretical model an the results obtained from the simulation.

Fig. 4.9 presents a flow diagram of the above procedure. The next section will verify the model and its underlying Pearson random walk against experimental data.

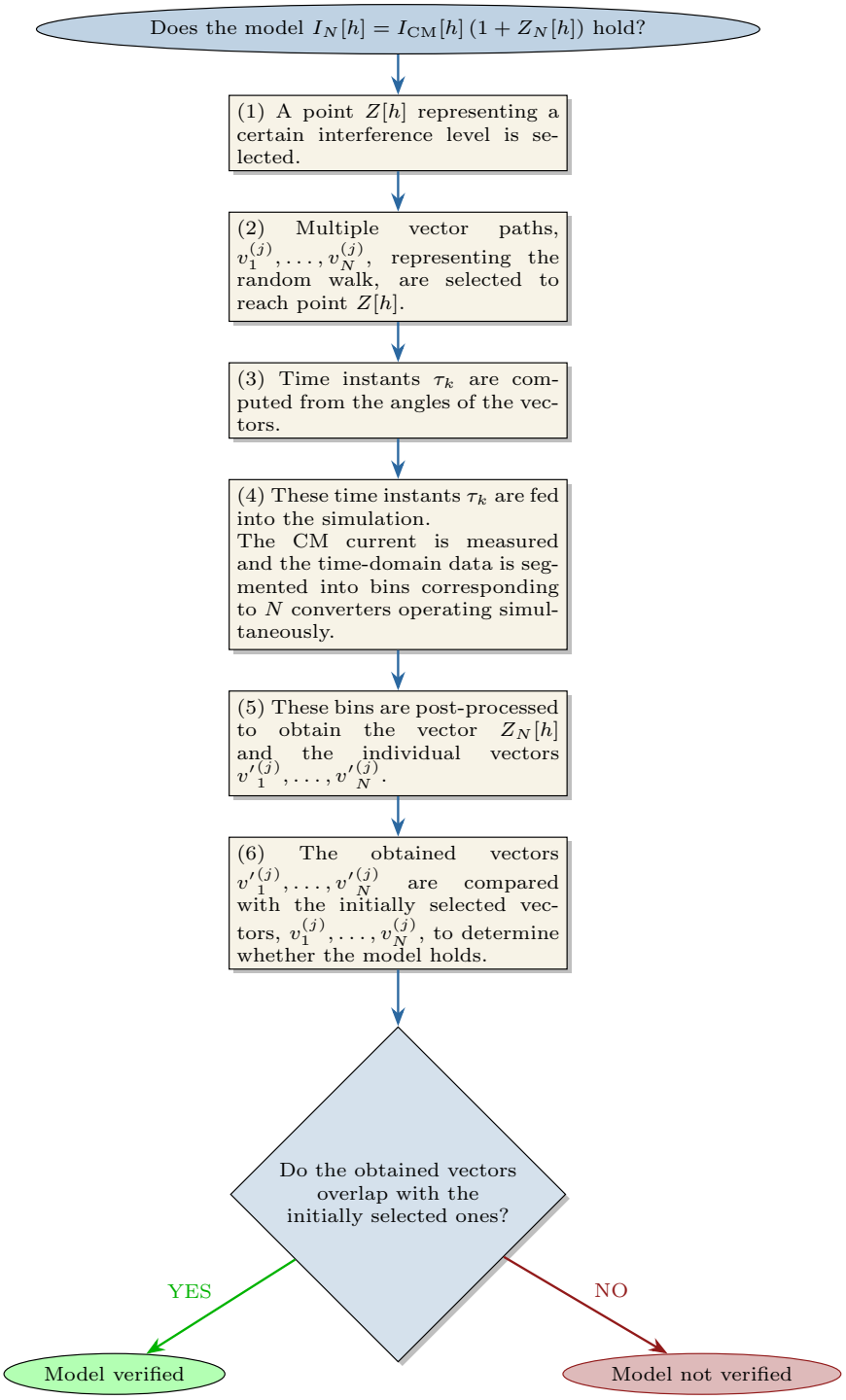

Figure 4.9: Flow diagram for the verification of Pearson's Random Walk model vs simulation data.

4.2 Experimental-based verification

The previous section verified the Pearson Random Walk summation model, described by $I_N[h] = I_{\mathrm{CM}}[h]\,(1 + Z_N[h])$, against simulation data. The section began with descriptions of both the simulation setup and procedure. The primary objective was to verify that the Pearson Random Walk concept, which generates vectors in different directions, can be used to describe the behaviour of multiple PE converters. The model's verification against simulation data was thoroughly described in subsection 4.1.3 and its effectiveness has been demonstrated. This section extends the verification to experimental data, beginning with the description of the experimental setup and procedure and followed by preliminary results.

4.2.1 Experimental setup

The experimental setup is illustrated in Fig. 4.10 where part a) presents an overview of the entire setup and part b) shows the converters within the enclosure. The schematic of the experiment is shown in Fig. 4.11. The setup consists of:

1. An EA-PS 3080-20 C power supply that provids 45 V DC voltage to the three DC/DC converters;

2. Two Teledyne T3AFG120 function generators, one dual-channel, one single-channel, used to drive the MOSFETs of the three DC/DC converters;

3. Three Infineon (M100002230) CoolGaNTM e-mode HEMT half-bridge evaluation boards, based on Gallium Nitride (GaN) MOSFET technology rated for 450 V and 35 A with a maximum rated power of

a)

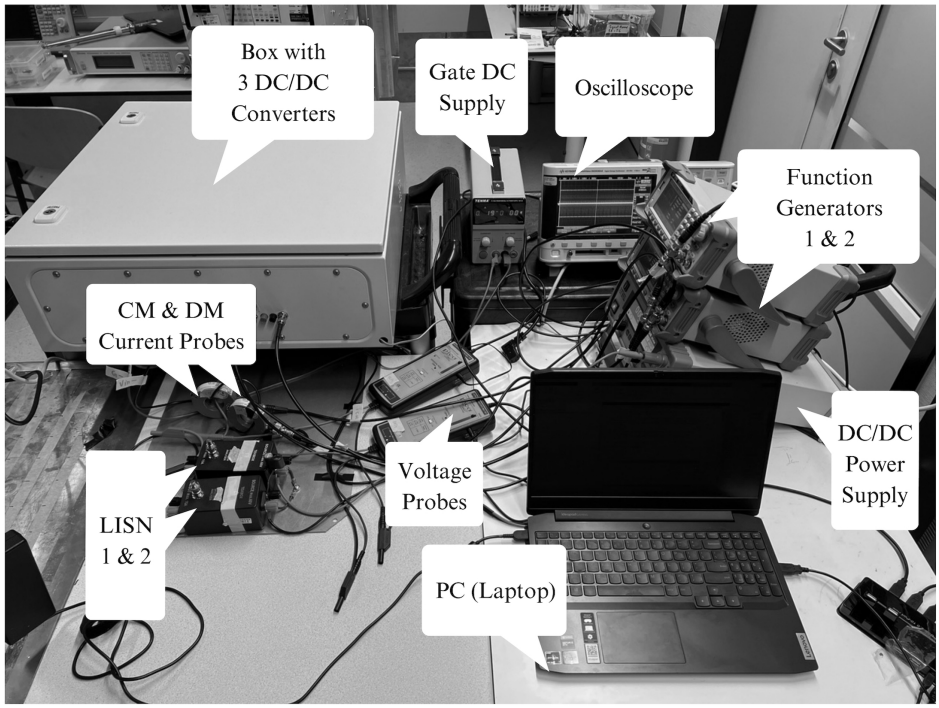

b)

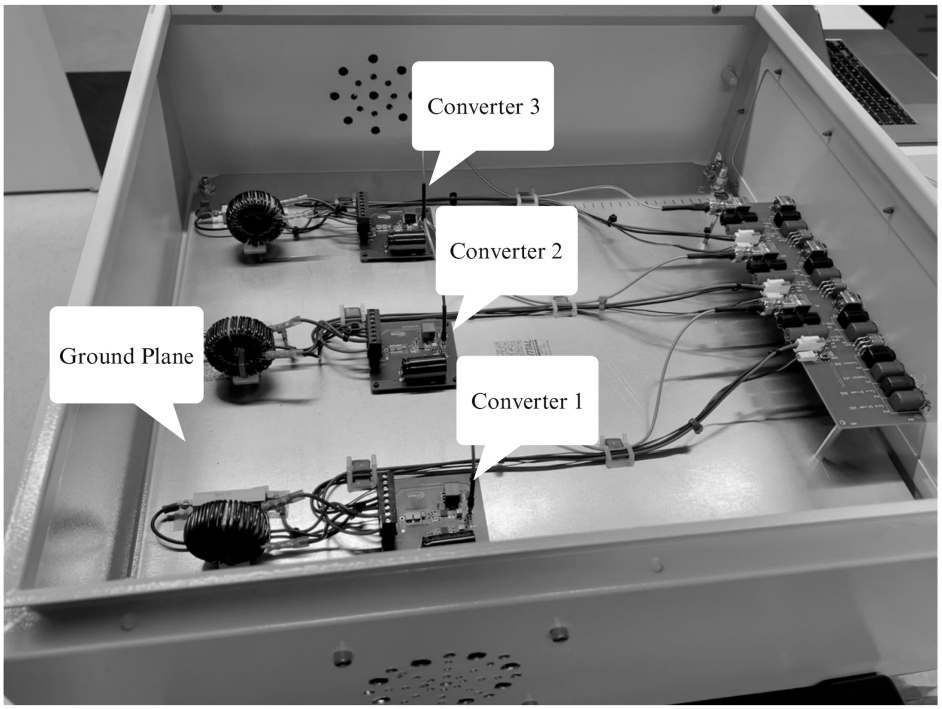

Figure 4.10: Experimental setup: (a) measurement system comprising three DC/DC converters, two function generators, two Line Impedance Stabilisation Networks (LISNs) and an oscilloscope. (b) arrangement of the three DC/DC converters within the enclosure.

2500 W. Each board is connected to a 50 µH inductor and a 50 Ω resistive load [66];

4. A Tenma 72-2720 programmable DC Power Supply providing a stable 5 V DC and approximately 220 mA to drive the gates of the DC/DC converters.

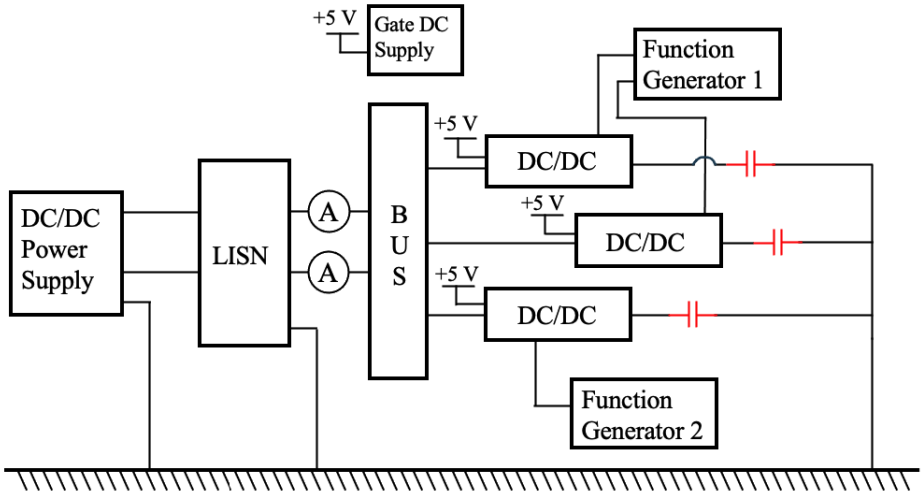

Figure 4.11: Experimental setup schematic with parasitic capacitances (shown in red).

The experimental procedure utilised three identical converters with specifications described above. Each converter operated at a switching frequency of $f_{\text{sw}} = 100\,\text{kHz}$ and a sampling frequency $F_s = 2\text{GHz}$ was used to sample the CM current. The Teledyne function generators were connected to a personal computer through USB ports, and controlled programmatically using SCPI commands through National Instrument's NI-MAX software. Control signals were rectangular waves with specified frequency, duty cycle, phase, and amplitude, generated with a basic wave SCPI command (BSWV) [1]. For CM current collection, a Fischer Custom Communications

[1]The BSWV command represents a fundamental SCPI (Standard Commands for Programmable Instruments) instruction used in signal generation instrumentation. This command enables the configuration of primary waveform parameters through a structured syntax.

Radio Frequency (RF) current probe (bandwidth of 1 kHz – 250 MHz) was employed and followed the procedure outlined in [69]. The probes was connected to the Keysight InfiniiVision DSOX3024A oscilloscope. Both the SCPI command transmission to function generators and data collection from the oscilloscope were implemented in MATLAB.

4.2.2 Deterministic Verification of Pearson's Random Walk Model

In order to verify that the signal generators were synchronised in producing accurately timed waveforms, and that Pearson's Random Walk model holds for the experimental setup proposed above, a series of deterministic test cases were performed with known resultant vector $|Z_3^{(l)}[h']|$ at 45° $\left(\frac{\pi}{4}\right)$, 90° $\left(\frac{\pi}{2}\right)$, 180° (π) and 225° $\left(\frac{5}{4}\pi\right)$. The phases presented in Table 4.1 were applied to the individual converters and the results used to verify that the control system was performing as expected as well as that the obtained vectors correspond to the initially chosen ones $|Z_3^{(l)}[h']|$.

The experimental measurements followed these steps:

1. CM current measurements were obtained by configuring the Function Generators with specific phases. The converter activation phases, specified in Table 4.1, were selected to achieve vector $|Z_3^{(l)}[h']|$ angles of $\frac{\pi}{4}, \frac{\pi}{2}, \pi$, and $\frac{5}{4}\pi$. The single converter phases were derived using parallelogram angle formulae. Appendix A provides a detailed derivation of these phases.;

2. Phase verification was performed by comparing the arbitrary chosen values with those estimated from the measured data;

3. Harmonic analysis was conducted in real-time, storing only the CM current harmonics. This approach optimised data storage requirements, as full time-domain data storage would require approximately 500 GB. However, three periods of time-domain data were retained for verification.

	Converter 1	**Converter 2**	**Converter 3**	$\angle Z_3^{(l)}[h']$
Case 1	0°	8°	82°	45°
Case 2	0°	53°	127°	90°
Case 3	0°	143°	217°	180°
Case 4	0°	188°	262°	225°

Table 4.1: Converter phase angles derived for known $\angle Z_3^{(l)}[h']$, using parallelogram formulae (see Appendix A).

Fig. 4.12 shows the representative PWM signals applied to the three converters, alongside the CM current measured via the RF current probe. The second test case from Table 4.1 is presented, where the first converter (yellow signal) operates at 0°, the second converter (red signal) at 53°, and the third converter (blue signal) at 127°. Part b) of the Fig. 4.12 demonstrates a clear correlation between the PWM signals and the spikes in CM current. Specifically, the rising edges of the PWM signals correspond to downward spikes in CM current, whilst the falling PWM edges correlate with rising spikes in CM current. Moreover, the damped oscillations of the CM current attenuate to a steady state before the next switching event.

The complex vector $|Z_3^{(l)}[h']|$ was subsequently recovered using the methodology detailed in the following Section 4.2.3

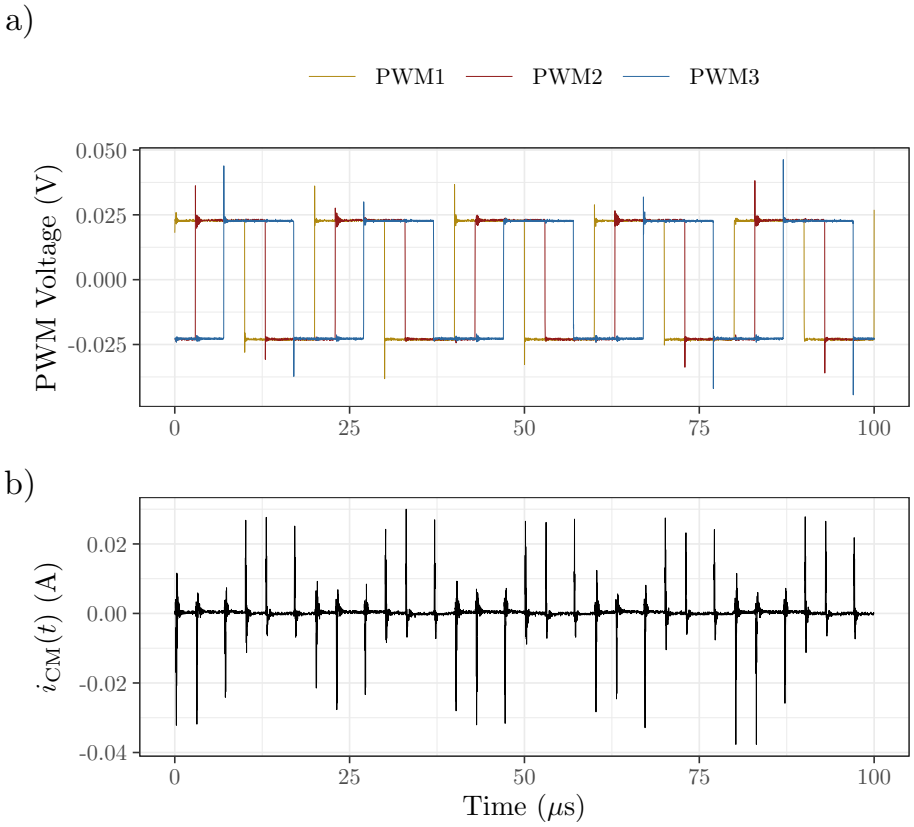

Figure 4.12: Time-domain representations a) PWM signals and b) CM current.

4.2.3 Preliminary Results

This section presents preliminary results to deterministically verify the Pearson's Random Walk Model against experimental data collected from three converters.

1. For a selected harmonic $h' = 1$, l points $Z_3^{(l)}[h']$ were chosen such that $|Z_3^{(l)}[h']| = 1.2$. The four arbitrarily chosen points $Z_3^{(l)}[h']$ are shown in Fig. 4.13 and correspond to 45° $\left(\frac{\pi}{4}\right)$, 90° $\left(\frac{\pi}{2}\right)$, 180° (π) and 225° $\left(\frac{5}{4}\pi\right)$.

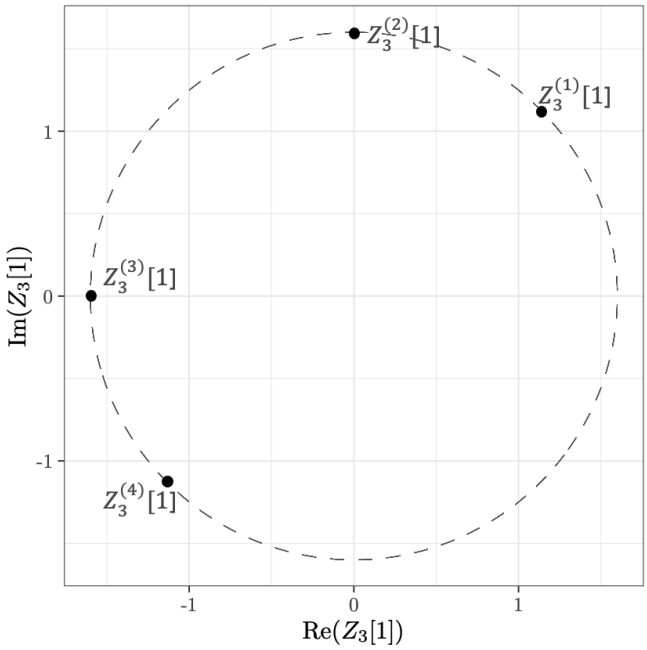

Figure 4.13: For a selected harmonic $h' = 1$, l points $Z_3^{(l)}[h']$ can be chosen such that $|Z_3^{(l)}[h']| = 1.2$..

2. For each point there are K paths $v_1^{(j)}, v_2^{(j)}, v_3^{(j)}$, where $j = 1, \ldots, K$ to reach that point.

   These paths are shown in Fig. 4.14 for each of the arbitrarily chosen points. For $N = 3$ converters, only two paths are possible. Given that

$$v_1^{(j)} = 0 + \mathbf{j}0 \tag{4.8}$$

   and

$$|v_2^{(j)}| = |v_3^{(j)}| = 1 \tag{4.9}$$

   for any j. Consequently, vectors $v_2^{(j)}, v_3^{(j)}$, and $Z_3^{(l)}[h']$ form an isosceles triangle, with internal angles determined by fixed side lengths. Thus, if $\arg(Z_3^{(l)}[h']) = \alpha$ and $\arg(v_2^{(j)}) = \beta < \alpha$, then $\arg(v_3^{(j)}) = 2\alpha - \beta > \alpha$. Similarly, if $\arg(v_2^{(j)}) = \beta > \alpha$, then $\arg(v_3^{(j)}) = \beta - 2\alpha < \alpha$. Therefore, with $K = 2$ the vectors $v_2^{(1)}, v_3^{(1)}, v_2^{(2)}, v_3^{(2)}$ form a parallelogram.

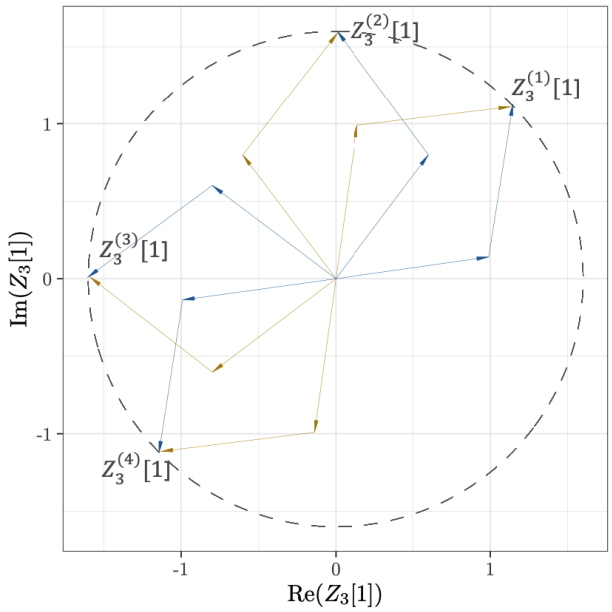

Figure 4.14: For each point there are K paths $v_1^{(j)}, v_2^{(j)}, v_3^{(j)}$. For $N = 3$ converters, only two paths are possible for each point.

3. Rather than selecting the time-step τ, as described in point 3 of the 4.1.3, where $\tau_k^{(j)}$ was obtained via

$$\tau_k^{(j)} = -\frac{\arg\left(v_k^{(j)}\right)}{2\pi f_{\mathrm{sw}} h'} \bmod \frac{1}{f_{\mathrm{sw}} h'}, \tag{4.10}$$

the procedure implemented for the function generators allowed specifying the phase $\alpha \in (0, 2\pi)$. This means that initially four distinct points $Z_3^{(1)}[1], Z_3^{(2)}[1], Z_3^{(3)}[1], Z_3^{(4)}[1]$ were selected such that their respective angles were $\frac{\pi}{4}, \frac{\pi}{2}, \pi$, and $\frac{5\pi}{4}$. Then, the phases of the converters were calculated using parallelogram angle formulae (described in Appendix A). These phases correspond to time instants τ_2 and τ_3, with the assumption that the first converter always starts at phase 0 ($\tau_0 = 0$).

4. The CM current values were collected. Fig. 4.15 presents the CM current for one, two and three converters, respectively, and indicates the time instants τ_2 and τ_3 at which the second and third converter

are activated. These τ_2 and τ_3 are calculated as described above (point 3), with τ_0 set to 0.

5. Two methods were employed to recover $Z^{(l)}[h]$ and the individual vectors ${v'}_1^{(j)}, {v'}_2^{(j)}, {v'}_3^{(j)}$.

   (a) FFT analysis: Application of FFT to the CM current.

   (b) τ-based analysis: Detection of peaks in the time-domain CM current values, estimation of the time-steps τ_k as illustrated in Fig. 4.15, and subsequent generation of vectors $e^{-\mathrm{j}2\pi f_{\mathrm{sw}}\tau_k h}$ using the estimated τ_k.

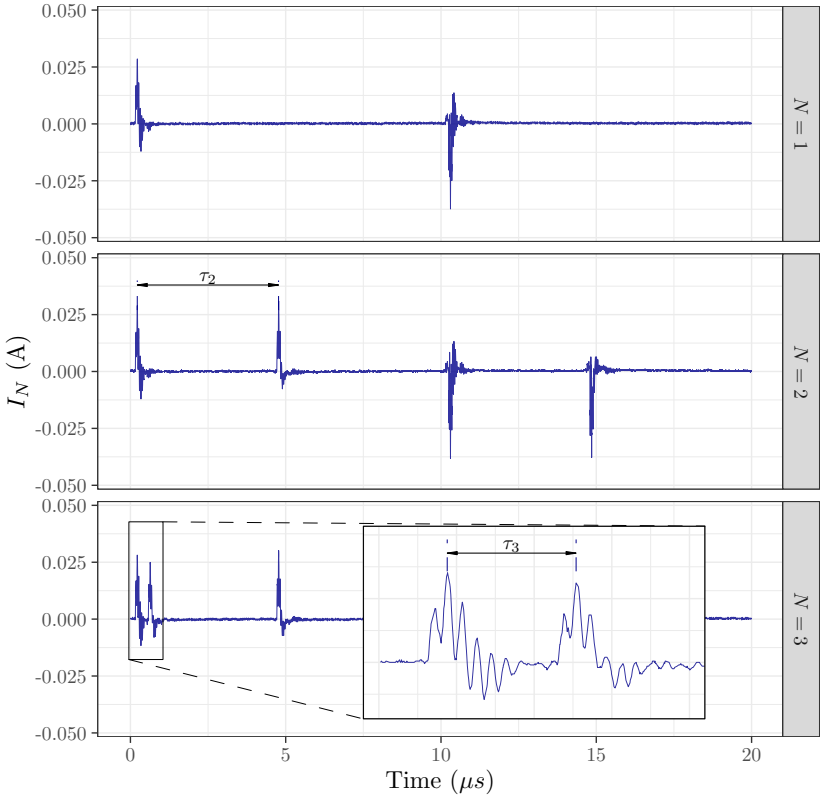

Figure 4.15: Common mode current with indicated τ_2 and τ_3.

Comparison in the complex domain

The vectors resulting from both post-processing methods are presented in Figure 4.16, illustrating two distinct paths (shown in gold and in blue) to reach the four arbitrary chosen points $Z_3^{(l)}[h']$. It can be noticed that the FFT-based method (shown with dotted lines) yields vectors that deviate slightly from the circle of radius 1.2, while the τ-based method (shown with solid lines), based on the estimation of time instants τ_k, produces precisely aligned vectors. The alignment in the second approach can be understood due to the fact that the τ-based method inherently assumes unit-length vectors and only the time instants τ_k are post-processed. However, the deviation obtained from the FFT approach is minimal, therefore, it could be assumed that the FFT-based approach, which does not make any implicit assumption about the length of the vectors, is appropriate for further exploration.

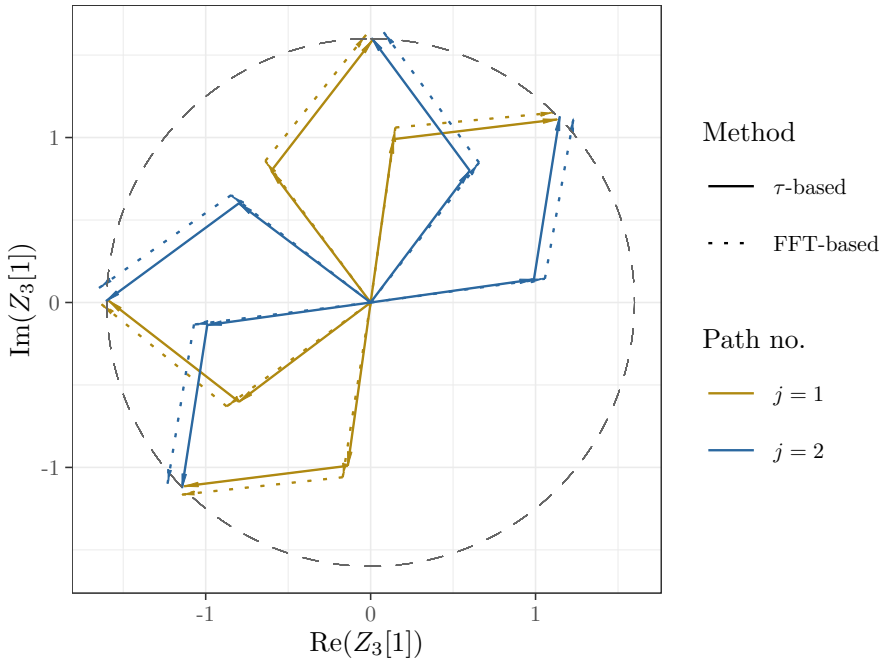

Figure 4.16: Vectors $v_1^{(j)}$, $v_2^{(j)}$, $v_3^{(j)}$ that sum up to $Z_3^{(1)}[1]$, $Z_3^{(2)}[1]$, $Z_3^{(3)}[1]$, $Z_3^{(4)}[1]$ obtained from measurements using the experimental setup presented in Fig. 4.10, using both τ-based approach and FFT-based approach.

4.2.4 Random Phase Measurements

Following successful verification of the Pearson's Random Walk model against the experimental setup, random-phase experiments were conducted. Two datasets of 1,000 and 4,000 CM current measurements were collected, with converter activation randomised according to the following procedure:

1. Converter phase assignment:
   (a) First converter maintained at 0° phase,
   (b) Second and third converters assigned independent random phases;
2. Measurement sequence for each iteration:
   (a) Single converter operation,
   (b) Two-converter operation,
   (c) Three-converter operation;
3. Data acquisition protocol:
   (a) Storage of CM current harmonics for each converter configuration,
   (b) Retention of two time-domain periods of CM current data.

The complex vector $|Z_3^{(l)}[h']|$ was recovered following the methodology detailed in Section 4.2.3 and the results will be presented in the following Chapter.

The experimental measurements with random phases required approximately 19 hours for 1,000 measurements and 75 hours (over 3 days) for 4,000 measurements.

4.2.5 Summary

Similar to the preceding section 4.1, this section established a methodology to verify the summation model proposed in (3.10) against measured data through the implementation of an experimental setup and procedure. The approach is founded on Pearson's random walk concept and its application to three PE converters in a simultaneous operation configuration.

The following was done:

- Four points were selected with angles of $\frac{\pi}{4}, \frac{\pi}{2}, \pi$, and $\frac{5}{4}\pi$, with two possible paths for three converters to reach each point;
- The switching times (converter phases) were derived from these selected points;
- CM current measurements were obtained and analysed using two methods (FFT-based and τ-based) to recover the complex vector $Z_3^{(l)}[h']$.

The objective was to verify that the converters switching-ON sequences, represented by two distinct vector paths, reached those arbitrarily selected points. The switching time instants were derived from the theoretical paths to reach those points and implemented in the converters. The alignment between theoretical and experimental paths signifies successful verification of the method to describe the behaviour of the three PE converters. Fig. 4.17 illustrates the procedural flow for model verification against experimental data.

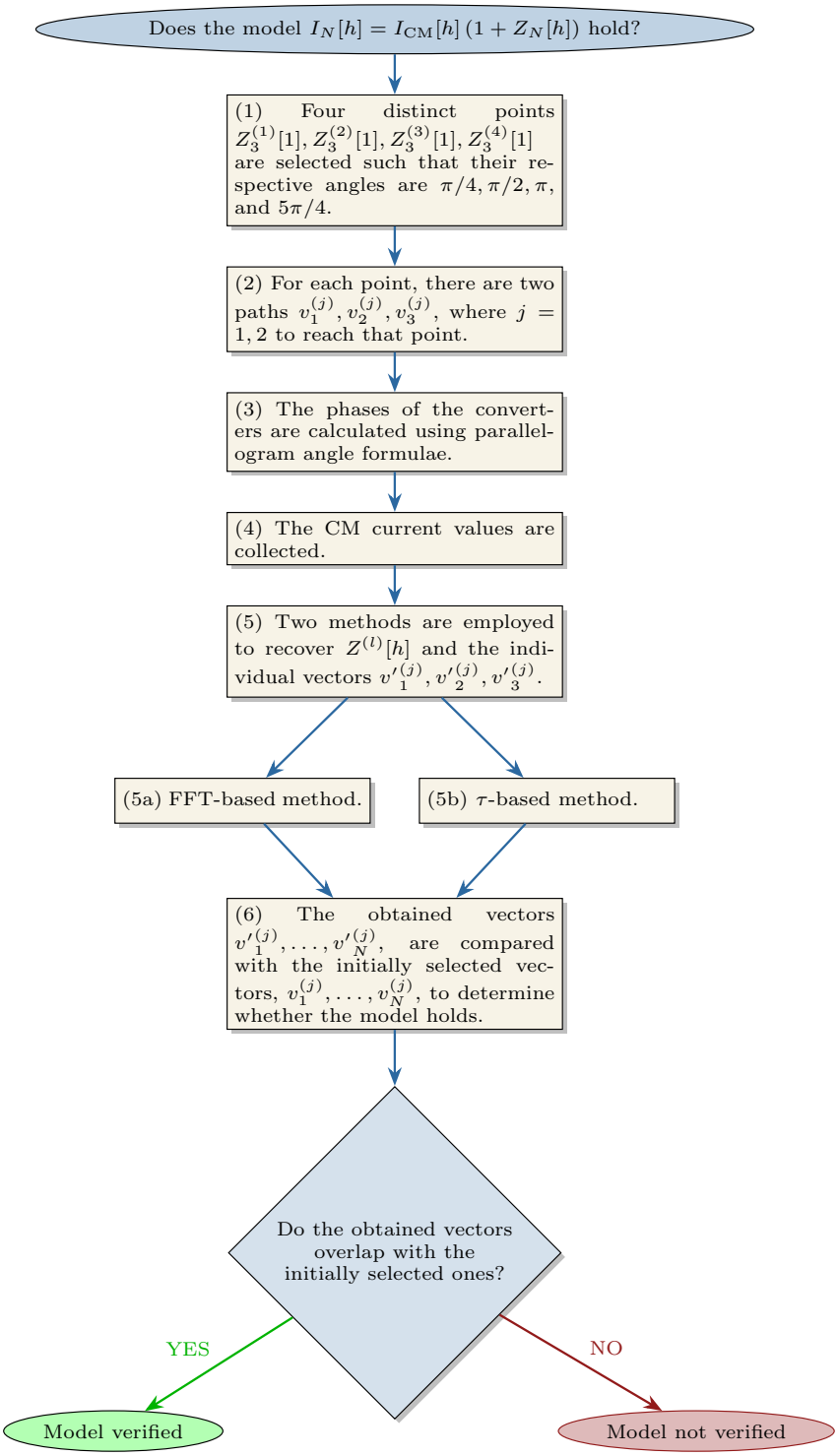

Figure 4.17: Flow diagram for the verification of Pearson's Random Walk model vs experimental data.

4.3 Conclusion

This chapter presented a methodology for verifying the applicability of Pearson's Random Walk model, described by (3.10), to the electrical engineering field to model the behaviour of multiple PE converters. The model verification through both simulation and experimental data demonstrated to be successful. Some preliminary results of deterministic verification of the model were included. The next chapter will present statistical verification using **empirical cumulative distribution funtion (ecdf)** and will address the research question: *what is the probability that the total CM current for N converters,* $|I_N[h]|$*, will decrease with respect to the CM current of one converter,* $|I_{\mathrm{CM}}[h]|$? This analysis will examine the probability of EMI reduction in multiple PE converter configurations compared with single-converter setups.

Chapter 5

Statistical Verification and EMI Reduction Analysis

The previous chapter introduced a methodology for verifying Pearson's Random Walk (PRW) model. The initial simulation approach provided descriptions of the setup, procedure and preliminary results, offering deterministic verification against simulation data. Subsequently, the experimental approach detailed the setup, procedure and preliminary results, providing deterministic verification against experimental data. The chapter demonstrated successful verification of the PRW model through alignment between the theoretical model and both simulation and experimental data, establishing its use to model the electromagnetic emissions, namely the CM current, of multiple PE converters.

From a practical perspective, the question regarding the absolute value of $I_N[h]$, representing the magnitude of the total CM current generated by N converters, remains to be addressed. More specifically, as the input variables (time shifts τ_k or, equivalently, the phase angles α_k) are randomly selected, it is necessary to determine the distribution of $|I_N[h]|$. At this

stage, the value of the total resultant current, $|I_N[h]|$ cannot be directly predicted, however, certain observations can be made regarding the effect of increasing the number of converters from 1 to N ($|Z_N[h]|$). Therefore, the focus can be placed on the contributions that result solely from the time-shifts. Particular attention is given to the **cumulative distribution function (cdf)**, which provides the probability that the random variable is less than or equal to a certain threshold value (in this case, denoted as r). In Chapter 3, these contributions were defined as

$$Z_N[h] = \sum_{n=2}^{N} e^{-\mathbf{j}2\pi f_{\mathrm{sw}} \tau_k h} \tag{5.1}$$

from (3.9). The distribution of the magnitude $|Z_N[h]|$ of the vector $Z_N[h]$ was provided by Kluyver [68] in the form of a **cdf**. This was described in Section 3.4 and its analytical form is recalled here:

$$P(|Z_N[h]| \leq r) = \int_0^{\infty} r J_0(t)^{N-1} J_1(rt)\ \mathrm{d}\, t, \tag{5.2}$$

where J_0 is the Bessel function of order 0 and J_1 is the Bessel function of order 1. The simulation results will therefore be juxtaposed with the analytical **cdf**.

This chapter presents, therefore, the statistical verification of the PRW model through **empirical cumulative distribution function (ecdf)**. The results are structured as follows: Section 5.1 presents a comparison using **ecdf** between the model based on (3.10), i.e., $I_N[h] = I_{\mathrm{CM}}[h]\,(1 + Z_N[h])$, and the simulation data. Section 5.2 provides a comparison using **ecdf** between the model and experimental data. The chapter concludes with an analysis and computation of the probability of EMI reduction (specifically, of the h-th harmonic of the common mode current) in a multi-converter setup compared to a single-converter configuration.

The results presented herein are published in IEEE Transactions on Electromagnetic Compatibility, with the paper accepted for publication in February 2025 [70].

5.1 Statistical Verification of Pearson's Random Walk: Simulation Results

To verify the compatibility of Kluyver's solution (provided by (5.2)) with simulation results, an **ecdf** was obtained from 1,000 simulation trials. As described in Section 4.1.2 each simulation required approximately 10 minutes, resulting in a total computational time of 170 hours (7 days) for the entire set of 1,000 simulations when performed on a single machine. However, to reduce this time, the simulations were parallelised across two identical PCs, with 500 simulations allocated to each. Furthermore, as detailed in Section 4.1.2, it was decided to compare the results for $N = 3, 5, 8$ converters. This means that the switching times were modified from the original formulation $t_k = (k-1)\Theta T_{\text{sw}} + \tau_k$ (where each converter was being switched-ON sequentially, with the first converter operating individually, followed by two converters working simultaneously, then the third converter being added, followed by the fourth, and so forth) to $t_k = s_k \Theta T_{\text{sw}} + \tau_k$, where s_k represents grouped converter operations: $s_1 = 1$ for the reference converter, $s_2 = s_3 = 2$ for three simultaneous converters, $s_4 = s_5 = 3$ for five converters, and $s_6 = s_7 = s_8 = 4$ for eight converters. This modification reduced the number of bins from 8 to 4, with $\Theta = 266$ switching periods each. This allowed the further reduction of the time of the simulations by approximately a quarter, i.e. to around 2 days.

Fig. 5.1 presents a comparison between the **cdf** evaluated using Kluyver's

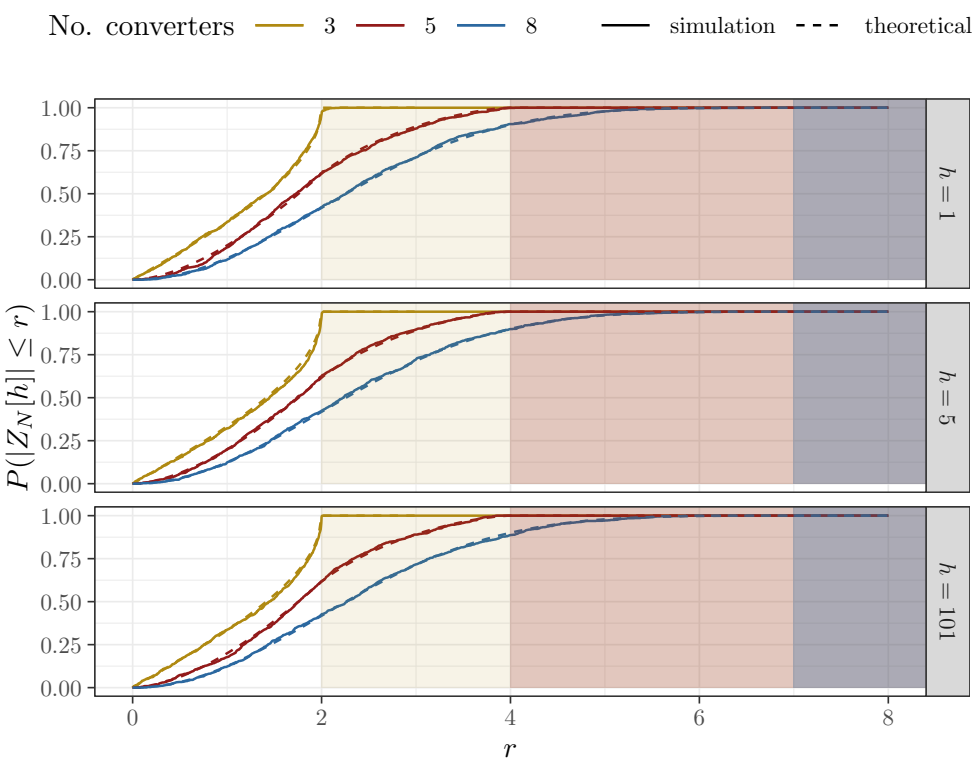

Figure 5.1: The empirical cumulative distribution function (simulation) vs cumulative distribution function obtained from Eq. (5.2) (theoretical) for $N = 3, 5, 8$ converters and 1^{st}, 5^{th} and 101^{st} harmonic.

solution to Pearson's Random walk, described by equation (5.2), and the **ecdf** resulting from the 1,000 simulations with 3, 5, and 8 converters operating, respectively. The x-axis shows the upper bound r for the length of $Z_N[h]$, while the y-axis presents the probability $P(|Z_N[h]| \leq r)$ that the length is smaller than or equal to r. The respective facets show the data for the 1st, 5th and 101st harmonic. Moreover, close alignment can be seen between the theoretical model (dashed lines) and the simulation results (comtinous lines).

The **ecdf** saturates (reaches the value of 1) at r equal to $N-1$ (with N the total number of converters), as illustrated by the shaded area in Fig. 5.1. This can be understood by recognizing that the highest magnitude achievable by $|Z_N[h]|$ occurs when all the unitary vectors $e^{-\mathbf{j}2\pi f_{\text{sw}}\tau_2 h}, \ldots, e^{-\mathbf{j}2\pi f_{\text{sw}}\tau_N h}$

align at the same angle, resulting in a magnitude of $N-1$. It is important to observe that the **ecdf** does not indicate the probability of $I_N[h]$ reaching a certain EMI level; rather, it counts the contributions from the converters 2 to N, without including the reference EMI current of a single converter $I_{\mathrm{CM}}[h]$. More precisely, the **ecdf** provides the probability of increasing or decreasing the total EMI at harmonic h. Analysis of the first harmonic (top facet in Fig. 5.1) for 8 converters (blue line) shows that both simulation and theoretical results (continuous or dashed line) yield a probability of approximately 0.35 for emissions to be below a certain threshold. For example, the probability of emissions being lower than 2 is ≈ 0.35. The probability of exceeding the threshold of 2 is the complement: $1-0.35=0.65$, representing the probability of EMI above the threshold. Moreover, this result (and therefore (5.2)) holds regardless of the harmonic number h. This also means that knowing the CM current for a single converter, the upper bound for the total CM current should not exceed $I_{\mathrm{CM}}N$.

A key question remains: *what is the probability that the total CM current for N converters, $|I_N[h]|$, will decrease with respect to the CM current of one converter, $|I_{\mathrm{CM}}[h]|$?* So, the investigation begins with a single converter generating a CM current. As additional converters are introduced, increasing from 1 to N converters, the research question addresses the probability of electromagnetic noise reduction in the presence of multiple sources. This presents an interesting theoretical challenge, as it contradicts the intuitive assumption that additional converter units would lead to increased electromagnetic interference levels. The theoretical resolution to this question will be presented in Section 5.3, following statistical verification of the model on experimental data in the next section.

5.2 Statistical Verification of Pearson's Random Walk: Experimental Results

The experimental setup comprising three converters, described in Chapter 4, Section 4.2, was employed to generate a larger dataset so that the statistical variation in the results could be analysed and compared with Kluyver solution (expressed in Equation (5.2)). The experiment consisted of two measurement sets: 1,000 and 4,000 runs, with randomly distributed converter phases. The first converter consistently operated with 0∘ phase delay, whilst the second and third converters were configured with independent random phases. The phases of the three converters were denoted as α_1, α_2 and α_3 with α_1 fixed at 0. The angles (phases) α_2 and α_3 were sampled from a pseudo-random uniform distribution $\mathcal{U}(0, 2\pi)$. These angles were applied as input to the function generators. The CM current measurement required approximately 19 hours for 1,000 runs and 75 hours (3.1 days) for 4,000 runs.

Fig. 4.15 displayed the measured CM current for one converter (top facet, $N = 1$), two converters (middle facet, $N = 2$), and three converters (bottom facet, $N = 3$). The time instants τ were calculated between them using the τ-based procedure. Initially, the first peak was detected, followed by the detection of the second peak, which enabled estimation of τ_1. Subsequently the third peak was detected, allowing estimation of τ_3. With the time instants identified and the switching frequency known, the angles were computed by inverting the relationship:

$$\tau_k^{(j)} = -\frac{\arg\left(v_k^{(j)}\right)}{2\pi f_{\text{sw}} h'} \bmod \frac{1}{f_{\text{sw}} h'}, \tag{5.3}$$

thus:

$$\arg\left(v_k^{(j)}\right) = -2\pi f_{\text{sw}} h' \cdot \tau_k^{(j)} \bmod 2\pi. \tag{5.4}$$

This provides the expression for the angles, $\arg\left(v_k^{(j)}\right)$, where the result is taken modulo 2π as the arguments of these complex numbers (which represent the angles) are expressed in the range $[0, 2\pi)$.

Then, for verification purposes, the angles drawn from a pseudo-random uniform distribution $\mathcal{U}(0, 2\pi)$ and input to the function generators (hereinafter referred to as assumed angles) were compared with the angles obtained as outputs from running the setup.

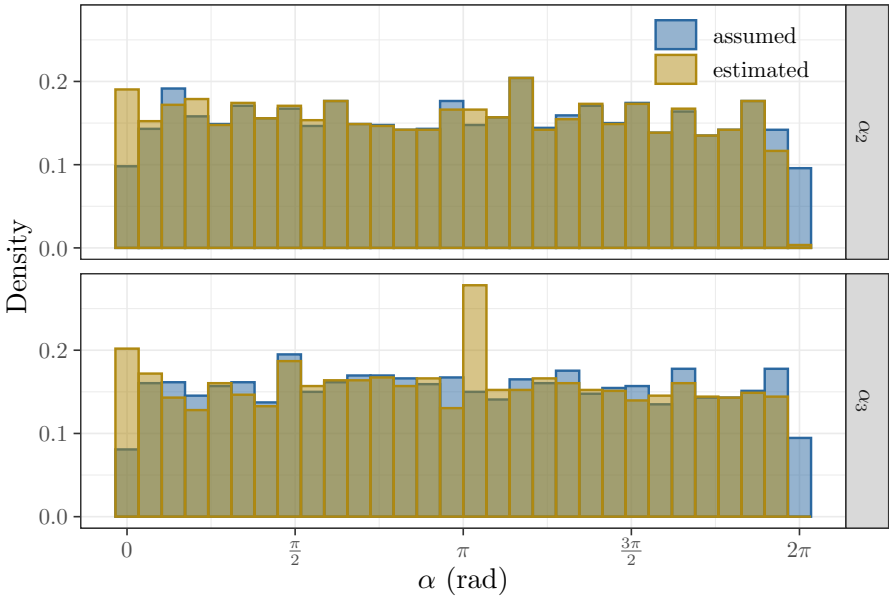

Figure 5.2: Histograms of angles α_2 and α_3, assumed as input to function generators, and estimated from time-domain measurements of CM current.

Fig. 5.2 presents the distributions of angles α_2 and α_3. It shows both the assumed angles, drawn from a pseudo-random uniform distribution $\mathcal{U}(0, 2\pi)$ and input to the function generators (shown in blue), and the angles estimated through the τ-based procedure obtained from running the setup (shown in gold). Slight deviations are observed between the assumed distribution and the one estimated from experimental measurements. The reason

could be twofold: the automatic measurement system may be misidentifying some of the pulses, or measurement noise could be confusing the system. However, as no skews occur, it can be confirmed that the distribution assumed for the angles has not significantly changed after running the set-up, i.e., the angles of the post-processed data also follow a uniform distribution $\mathcal{U}(0, 2\pi)$. Therefore, the experimental data can be used for estimating the cdf of $|Z_N[h]|$.

Finally, Fig. 5.3, similarly to what is shown in Fig. 5.1, presents a comparison between the theoretical cdf of $|Z_3[1]|$ and the numerically evaluated ecdf from the two measurement sets: 1,000 measurements (shown in red) and 4,000 measurements (shown in blue) obtained with three converters operating simultaneously. The ecdf curves, represented by solid lines, are bounded by confidence intervals (indicated by shaded areas enclosed by dotted lines), indicating the precision of the evaluation ($\pm 95\%$).

It can be observed that:

- For 1,000 measurements, the ecdf follows a similar trend to the theoretical one, although discrepancies are evident since the beginning and for values of r up to 2, with maximum deviation occurring at approximately $r = 2$.
- For 4,000 measurements, the ecdf aligns better with the theoretical curve, although the deviations persist in the vicinity of $r = 2$. (A more precise alignment with theoretical curve could be achieved through implementation of stratified sampling techniques [71], by identifying the angles that yield values of r close to 2 and increasing sampling from that range of angles.)

The distribution of $|Z_3[1]|$ is represented in Fig. 5.4 through a pdf histogram

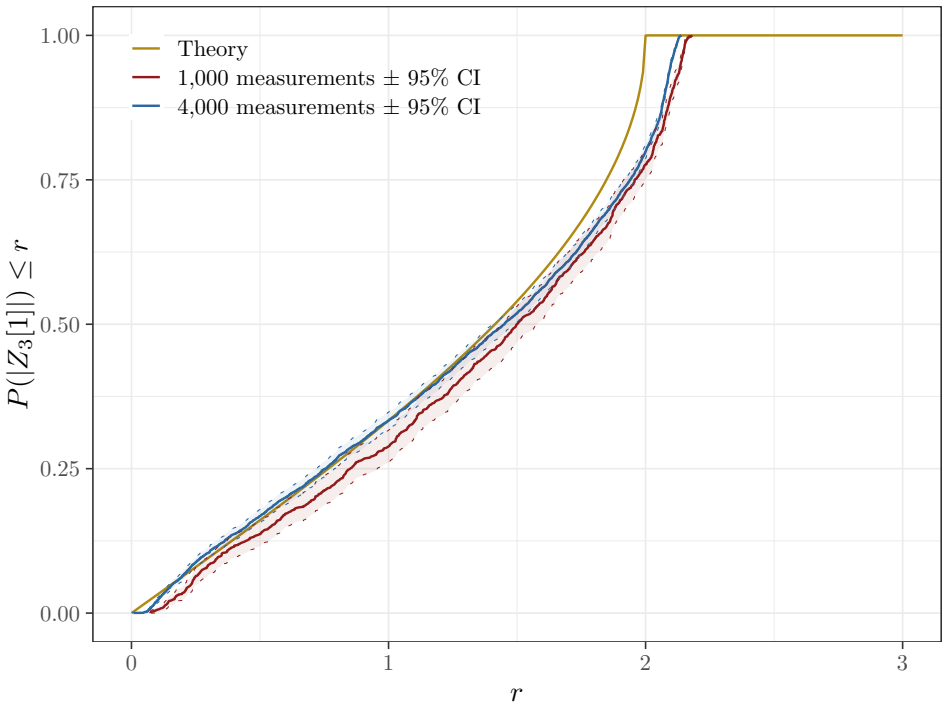

Figure 5.3: Cumulative distribution function of $|Z_3[1]|$ obtained from Eq. (5.2), and empirical cumulative distribution functions obtained from 1,000 and 4,000 measurements with confidence intervals indicated by dotted lines and shaded area.

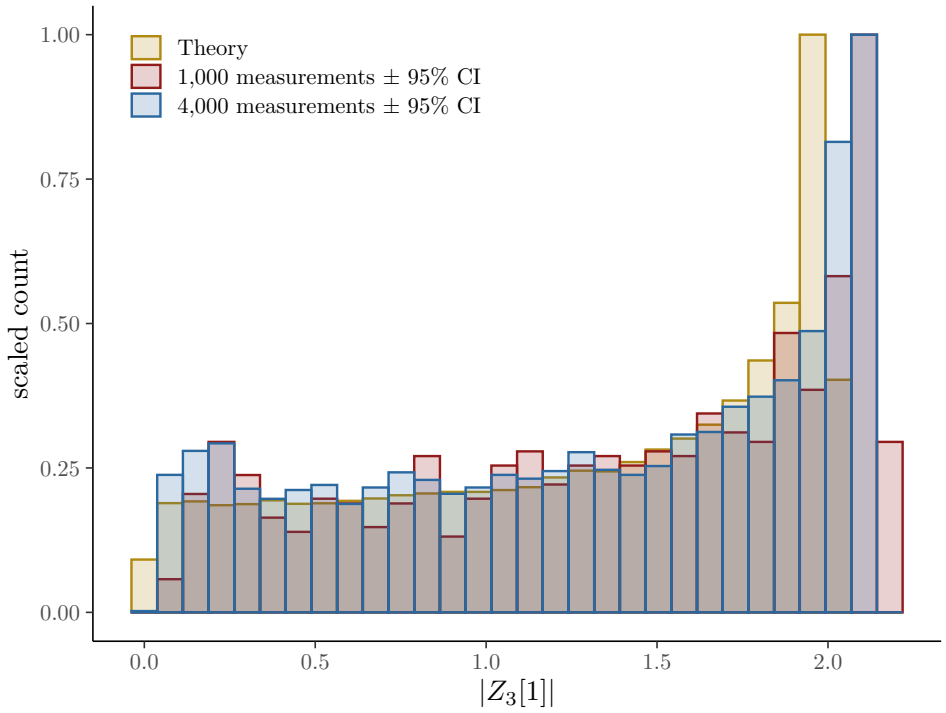

Figure 5.4: Histogram of $|Z_3[1]|$ obtained from differentiating the empirical cumulative distribution functions obtained from 1,000 and 4,000 measurements.

derived by differentiating the ecdf with each bin showing the counts of occurrences. While the increased number of measurements in the second case yields higher bin counts, normalisation to 1 facilitates direct comparison between the two measurement sets, thereby improving the visualisation of relative counts.

It can be observed that also in this case:

- The shape of the histograms for 1,000 and 4,000 measurements follow the theoretical one with the discrepancies mentioned before.
- From the set of 4,000 measurements, approximately 750 are around $r = 2$ and all the other measurements are 'evenly' distributed for values of r up to 2. This is in agreement with the theoretical probability.

These experimental results verify the Pearson's random walk model as an effective approach for characterising electromagnetic emissions in multi-converter configurations. Further investigation is needed regarding the potential for electromagnetic interference mitigation through multiple converter implementations. The next Section 5.3 will finally address the research question *what is the probability that the total CM current for N converters,* $|I_N[h]|$*, will decrease with respect to the CM current of one converter,* $|I_{\mathrm{CM}}[h]|$?

5.3 Probability of EMI reduction

This thesis ultimately seeks to answer the research question: *What is the probability that the amplitude of the CM noise in a system with multiple converters, $|I_N[h]|$ will decrease with respect to the CM noise generated by a single converter, $|I_{\mathrm{CM}}[h]|$?* By examining (3.10), namely $I_N[h] = I_{\mathrm{CM}}[h]\,(1 + Z_N[h])$, one can observe that sufficient conditions arise when $|1 + Z_N[h]| \leq 1$, which occurs if the endpoint of the vector $Z_N[h]$ lies within the unit circle centred at $(-1, 0)$. Fig. 5.5 depicts the random walk patterns for $N = 8$ converters, illustrating four distinct trajectories. Each trajectory represents a different random walk sequence, corresponding to various switching-ON sequences of the PE converters. Only two of these paths (shown in red) result in the reduction of h-th harmonic value, as their endpoints fall within the unit circle centred at $(-1, 0)$, whilst the remaining two paths do not yield EMI reduction. Of particular significance are the two upper paths. Although they begin in close proximity, only the red path terminates within the unit circle. Had the fifth golden vector been oriented marginally downward, the final vector would have terminated within the unit circle. This observation suggests that EMI reduction could be achieved by controlling the switching-ON time of the sixth converter (represented by the fifth golden vector), which directly translates to changing the length of the resulting contributions incorporated in $Z_N[h]$.

As stated at the beginning of this section, the aim is to provide an explicit computation of the probability that the h-th harmonic of the CM current will be reduced in a setup with multiple converters compared to one with a single converter. The question remains: how does one compute this probability?

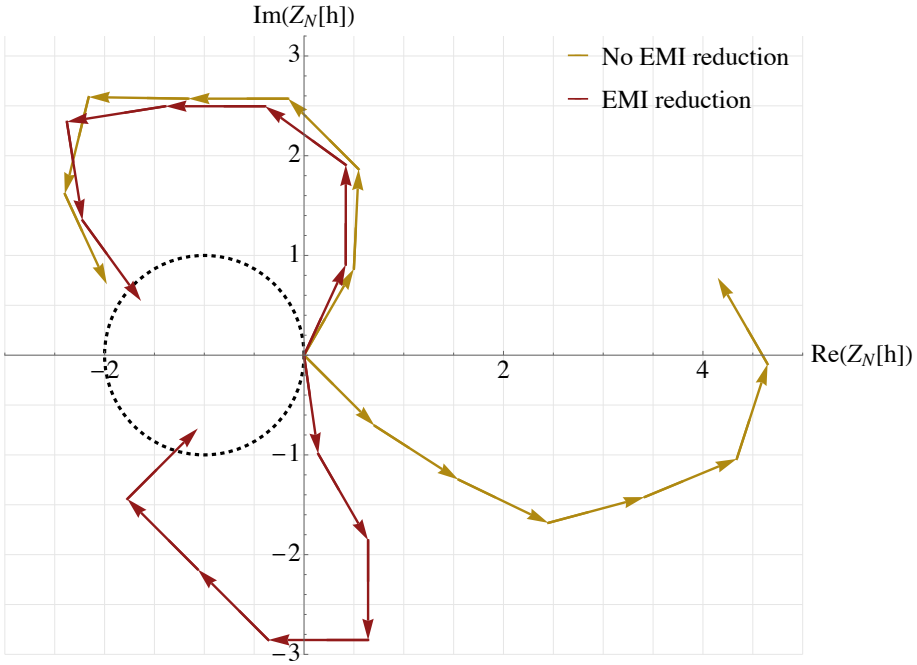

Figure 5.5: EMI behaviour for $N = 8$ converters. Four distinct random walk trajectories composed of $N-1$ unit vectors are shown. The red paths terminate within the unit circle centred at $(-1, 0)$, indicating configurations that achieve EMI reduction. The golden paths end outside this circle, representing configurations where EMI reduction is not achieved.

Let $p(r, \theta)$ denote a joint **pdf** of $Z_N[h]$. Assuming that the magnitude and phase of $Z_N[h]$ can be treated as independent random variables, it follows that

$$p(r, \theta) = p_N(r) p'_N(\theta), \tag{5.5}$$

where $p'_N(\theta)$ is the **pdf** of uniform distribution $\mathcal{U}(0, 2\pi)$, while $p_N(r)$ can be obtained by differentiating **cdf** from (5.2). Using the recursive properties of Bessel functions, this yields:

$$p_N(r) = r \int_0^\infty t J_0(t)^{N-1} J_0(rt)\, \mathrm{d}\, t. \tag{5.6}$$

This represents the differentiation of the solution provided by Kluyver. A full explanation and step-by-step differentiation is presented in Appendix B.

Fig. 5.6 shows the pdf $p(r, \theta)$, where $r = \sqrt{\mathrm{Re}(Z_N[h])^2 + \mathrm{Im}(Z_N[h])^2}$ and

$\theta = \arg(Z_N[h])$. As the **pdf** is rationally symmetrical around $(0, 0)$ only the negative range $(-6, 0)$ for the real part of $Z_N[h]$, and the range $(-6, 6)$ for the imaginary part of $Z_N[h]$ are shown. This joint pdf represents the distribution of all possible states resulting from time-shifted contributions of multiple converters to vector $Z_N[h]$. It can be understood intuitively that the value at 0 is 0, as the probability of vector $Z_N[h]$, which represents the sum of contributions from any additional converter, being exactly 0 is 0.

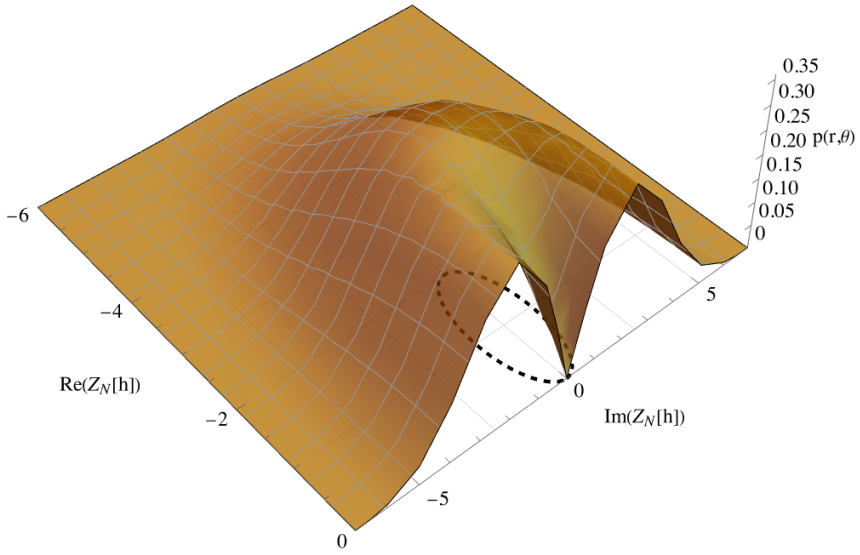

Figure 5.6: The joint **pdf** $p(r, \theta)$ is expressed as the product of **pdf** from (5.6) and the **pdf** of the uniform distribution $\mathcal{U}(0, 2\pi)$. Therefore, $p(r, \theta)$ is obtained by rotating the pdf from (3.12) around the z-axis.

The same $p(r, \theta)$ is shown as a contour plot in Fig. 5.7. The contours form concentric circles centred at the origin $(0, 0)$ indicating that the **pdf** $p(r, \theta)$ is rotationally symmetrical around the origin. The colour gradient, ranging from blue to red, indicates the value of the **pdf** $p(r, \theta)$. Red regions indicate higher probability densities, while blue regions indicate lower probability densities. The dashed circle represents the region where EMI reduction occurs. Interpreting this further, the red colour within the dashed circle

shows that the probability of the vector $Z_N[h]$ endpoint to be within that ϵ-region of the circle is 0.3.

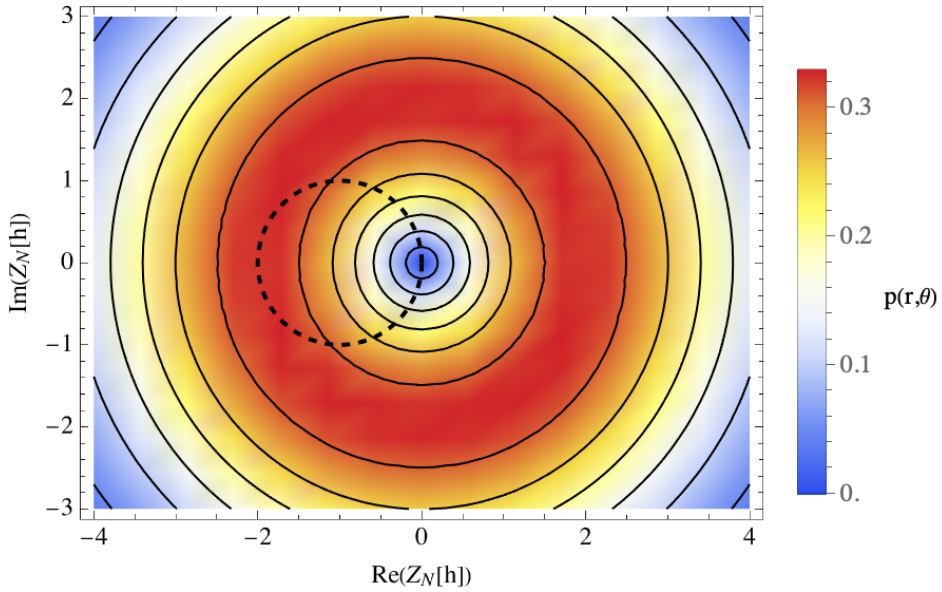

Figure 5.7: Contour plot of the **pdf** $p(r, \theta)$ of the vector $Z_N[h]$ endpoint to be in a certain region.

In the next step, the probability of the h-th harmonic reduction can be computed as a volume of a cylinder, the base of which is created from the unit circle centred at point $(-1, 0)$ and bounded by the **pdf** $p(r, \theta)$ from the top as shown in Fig. 5.8.

Finally, the volume of the red cylinder, as shown in Fig. 5.9, represents the probability of EMI reduction.

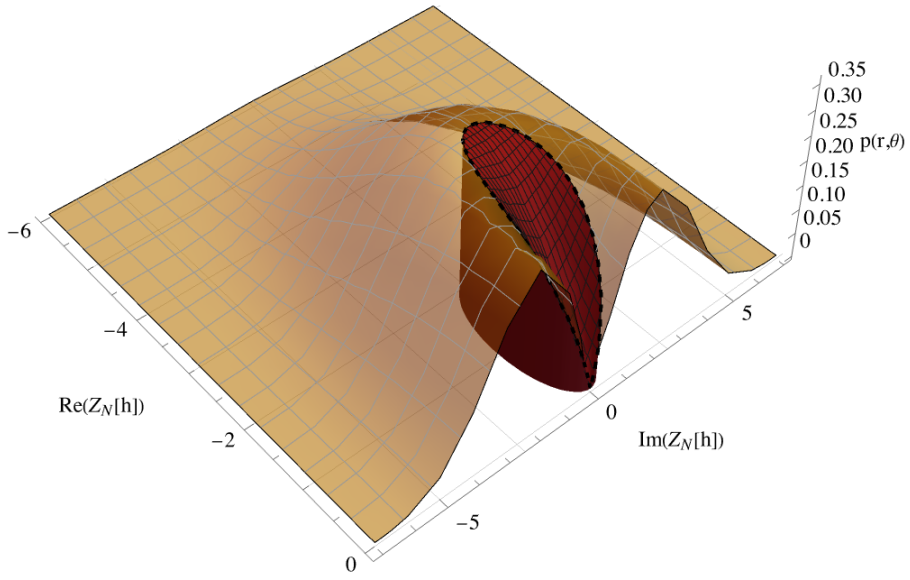

Figure 5.8: The probability of EMI reduction $P(|I_N[h]| \leq |I_{\mathrm{CM}}[h]|)$ of the h-th harmonic can be computed as the volume of the (red) cylinder based on a circle centred at $(-1, 0)$ and bounded by the joint **probability density function** $p(r, \theta)$ of $Z_N[h]$ (in orange).

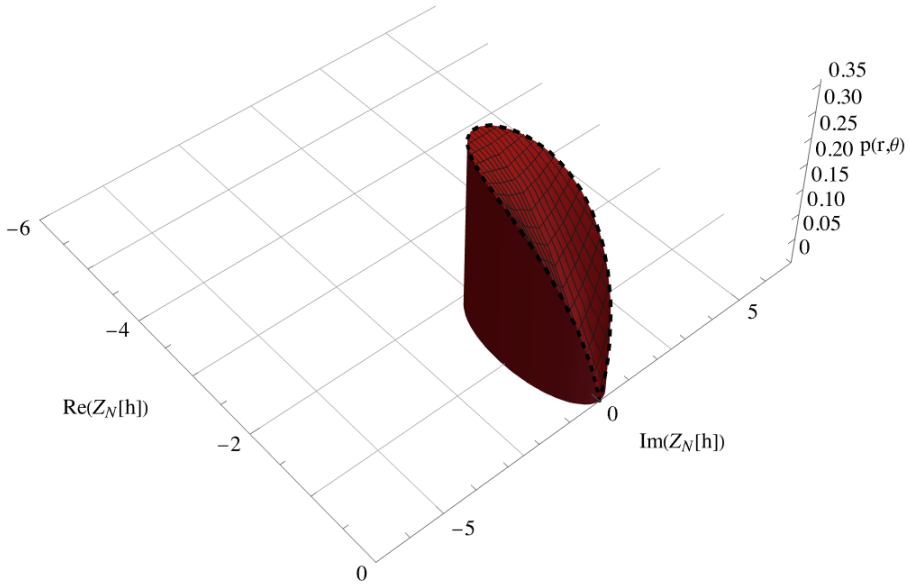

Figure 5.9: The volume of the red cylinder representing the probability of EMI reduction.

It follows that the same reasoning applies regardless of the number of converters, N. One can intuitively deduce that as the number of converters increases, the volume of the cylinder decreases, leading to a smaller probability of EMI reduction. Fig. 5.10, Fig. 5.11, and Fig. 5.12 show the probability of EMI reduction $P(|I_N[h]| \leq |I_{\mathrm{CM}}[h]|)$ of the h-th harmonic for $N = 10, 14, 30$ converters, respectively. a) The probability is computed as the volume of the (red) cylinder based on a circle centred at $(-1, 0)$ and bounded by the joint **probability density function** $p(r, \theta)$ of $Z_N[h]$ (in orange); b) The volume represents the probability of EMI reduction; c) The contour plot shows the joint **pdf** $p(r, \theta)$ as in a). Moreover, these figures illustrate precisely this decrease in volume (facets b) for $N = 10$, $N = 14$, and $N = 30$ converters, respectively. It is evident that for an increased number of converters $N = 30$ (shown in Fig. 5.12), the volume decreases with the respect to $N = 14$ converters (shown in Fig. 5.11), and decreases even further with respect to $N = 10$ (shown in Fig. 5.10). This can be appreciated by looking at the contour plots (facets c) where the red region, representing higher probabilities of the vector $Z_N[h]$ being within the unitary circle, moves outside the circle as the number of converters increases.

$N = 10$

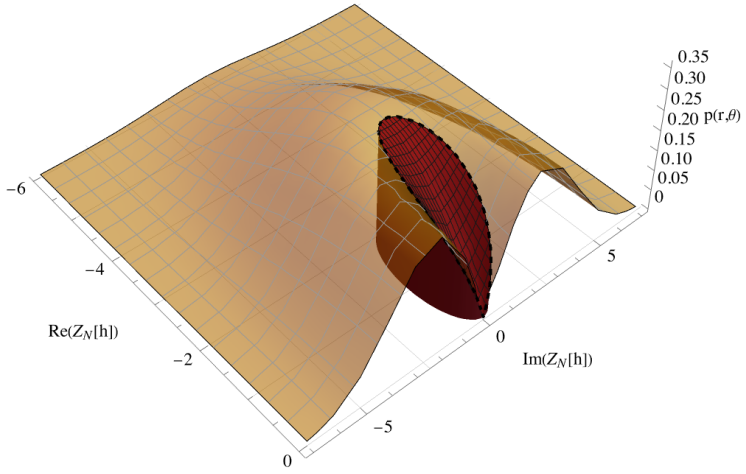

(a)

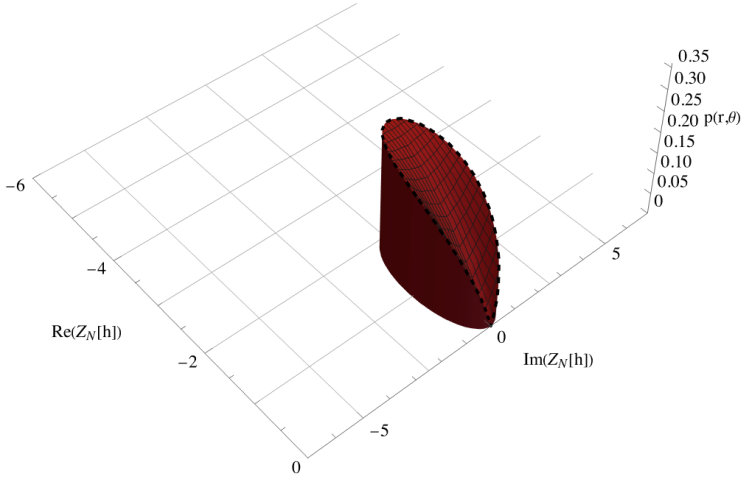

(b)

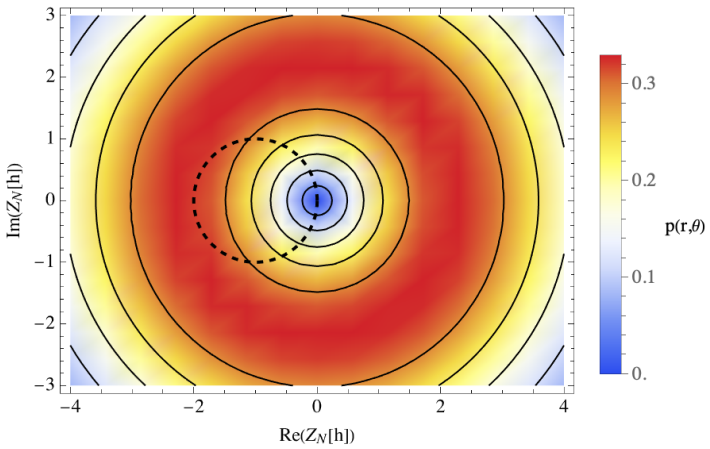

(c)

Figure 5.10: Probability of EMI reduction for $N = 10$ converters: a) joint pdf $p(r, \theta)$; b) EMI reduction probability: volume; c) contour plot of $p(r, \theta)$.

$N = 14$

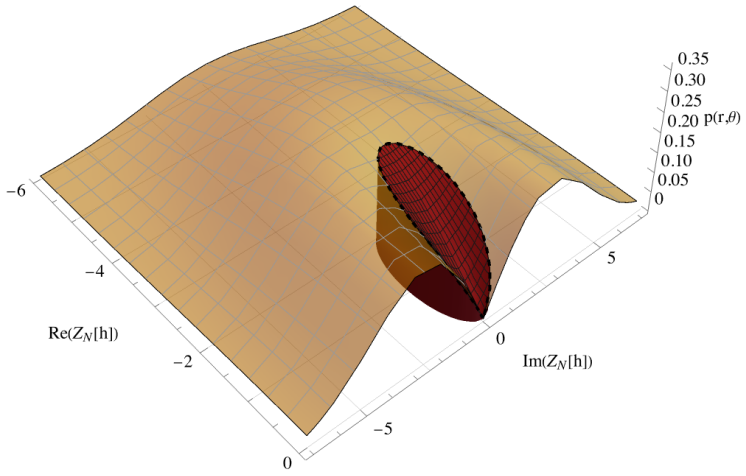

(a)

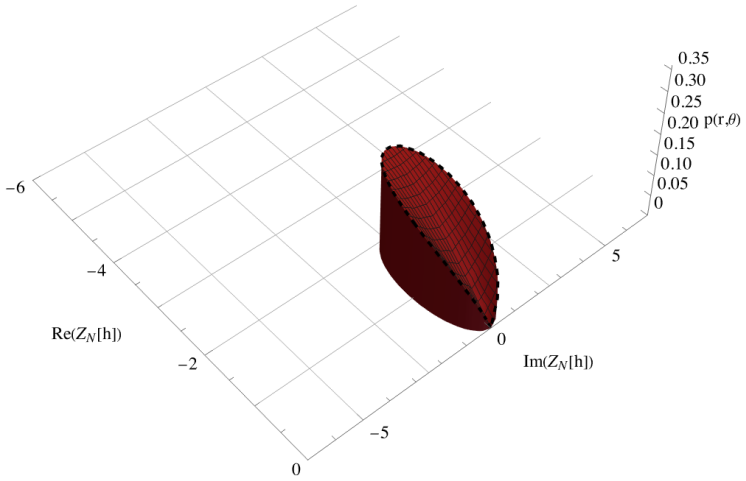

(b)

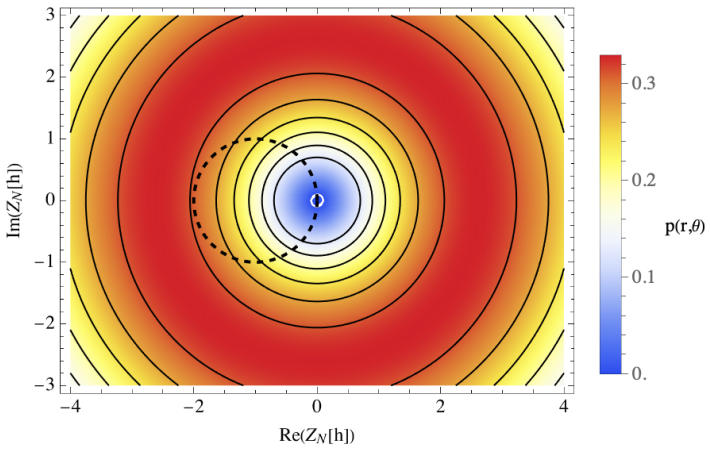

(c)

Figure 5.11: Probability of EMI reduction for $N = 14$ converters: a) joint pdf $p(r, \theta)$; b) EMI reduction probability: volume; c) contour plot of $p(r, \theta)$.

$N = 30$

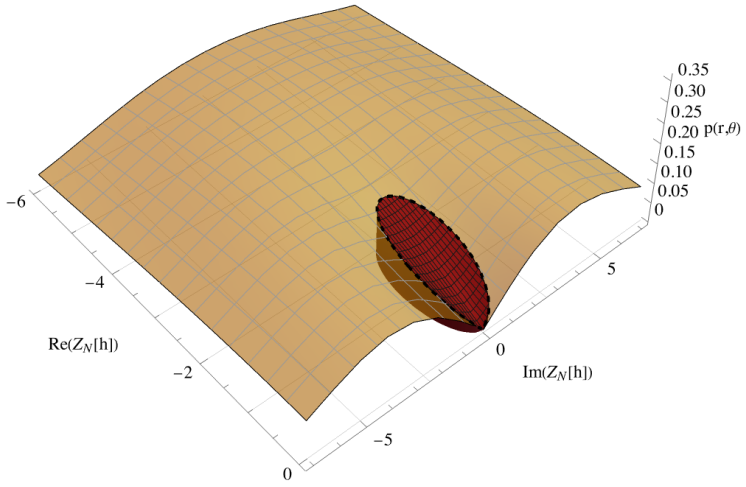

(a)

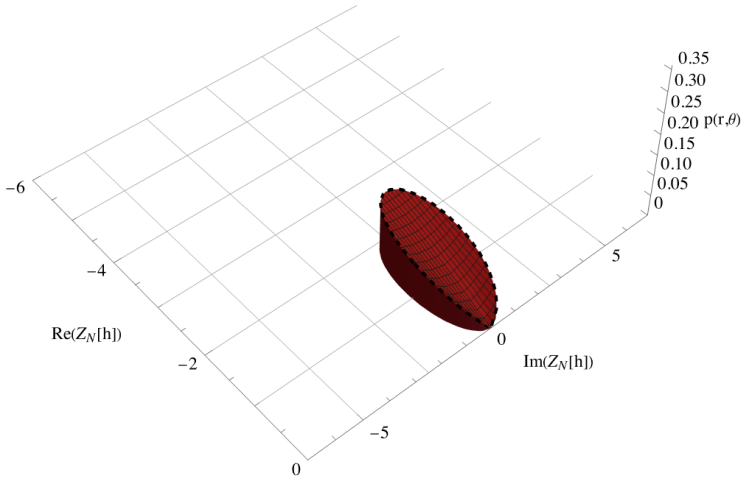

(b)

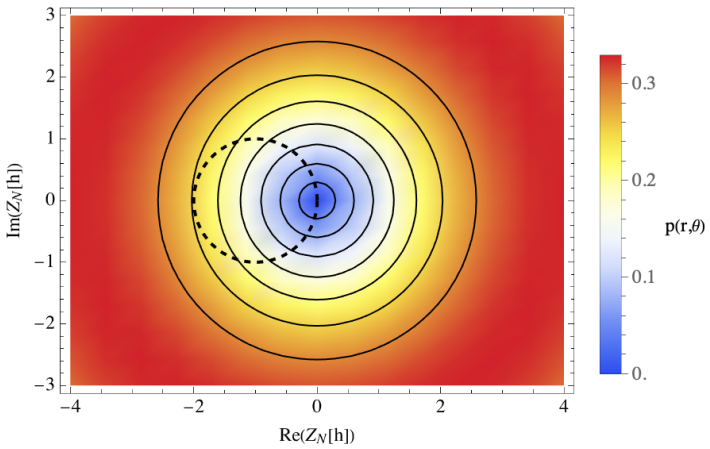

(c)

Figure 5.12: Probability of EMI reduction for $N = 30$ converters: a) joint pdf $p(r, \theta)$; b) EMI reduction probability: volume; c) contour plot of $p(r, \theta)$.

5.3.1 Analytical Model of EMI reduction

As stated above, to quantify the probability of EMI reduction, the following reasoning is required. The joint **probability density function** $p(r, \theta)$ of $Z_N[h]$ (shown in Fig. 5.10,5.11, 5.12 - facets a) and c) as a contour plot) represents the distribution of all possible states resulting from time-shifted contributions of multiple converters to vector $Z_N[h]$ and can be obtained by differentiating the original solution to the Pearson's Random Walk problem, provided by Kluyver [68] in the form of a **cumulative distribution function (cdf)**. The pdf exhibits rotational symmetry around $(0, 0)$. As established in Chapter 5, EMI reduction occurs when the endpoint of vector $Z_N[h]$ falls within the unit circle centred at $(-1, 0)$. Consequently, the EMI reduction probability can be calculated as the volume of a cylinder whose base is this unit circle and whose height is bounded by the pdf of $Z_N[h]$.

By integrating over the magnitude and phase, the probability of h-th harmonic reduction can be expressed as

$$P(|I_N[h]| \leq |I_{\mathrm{CM}}[h]|) = \frac{1}{\pi} \int_0^2 r p_N(r) \arccos\left(\frac{r}{2}\right) \mathrm{d}r, \tag{5.7}$$

under the assumption that the joint density $p(r, \theta)$ is normalized, which reduces to

$$\int_0^\infty r p_N(r) dr = 1. \tag{5.8}$$

To compute the probability of EMI reduction, the integration of the joint pdf $p(r, \theta)$ with the intersection of the cylinder based in $(-1, 0)$ is required. This two-dimensional pdf, $p(r, \theta)$, is a product of a one dimensional pdf $p_N(r)$ and $p'_N(\theta)$. Since these two variables can be thought as independent

variables, the joint pdf is given by the product of their individual distributions. When integrating this joint pdf over the entire domain, the result exceeds 1. To satisfy the fundamental property that a pdf must integrate to 1, normalisation is necessary. Hence, the assumption that the joint density $p(r, \theta)$ is normalized.

The mathematical derivation leading to this formulation is presented in the Appendix C.

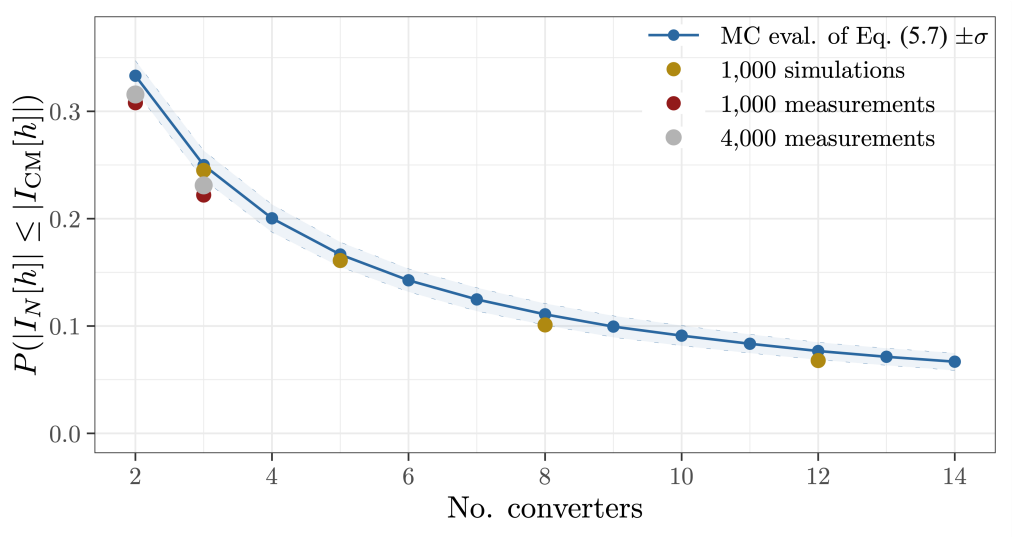

Figure 5.13: Probability of reduction of h-th harmonic EMI.

Fig. 5.13 presents the values of the probabilities $P(|I_N[h]| \leq |I_{\text{CM}}[h]|)$ obtained by numerically evaluating (5.7) (solid blue line) with the confidence interval (σ) indicated by dashed lines and shaded area. These are compared with the results of 1,000 simulations for 3, 5, 8, and 12 converters (yellow circles) as well as with the 1,000 (red circles) and 4,000 (grey circles) experimental runs with 3 converters. The probabilities in both simulation and experimental cases were obtained by counting the number of runs for which $|I_N[h]| \leq |I_{\text{CM}}[h]|$ and dividing by the total number of runs (1,000 and 4,000, respectively). To numerically evaluate (5.7), Monte Carlo samples were used to compute the volume of the cylinder, for each $N = 2, \ldots, 14.$, as Bessel functions are numerically unstable. The entire procedure was

performed for $h = 1$ of the switching frequency.

The theoretical probability (blue line) shows a decreasing trend as the number of converters increases, confirming the observations made in previous pages regarding the volume of the cylinder. The simulation results closely follow the theoretical curve. The experimental data for up to $N = 3$ align well with both the theoretical curve and simulation results providing validation of the model.

5.4 Conclusion

This chapter presented the statistical verification of the Pearson's Random Walk model through **empirical cumulative distribution function (ecdf)**. The analysis and the results demonstrated the effectiveness of the model in characterising electromagnetic emissions from multiple PE converters. The key findings were:

- Section 5.1 statistically verified the Pearson's Random Walk model, described by $I_N[h] = I_{\mathrm{CM}}[h]\,(1 + Z_N[h])$, through **ecdf** comparison against simulation data. The Kluyver solution, providing a **cumulative distribution function (cdf)** in integral form, was verified against the **ecdf** obtained from 1,000 simulations. In addition, the results demonstrated that the method is valid regardless of the harmonic under consideration;

- Section 5.2 statistically verified the Pearson's Random Walk model, described by $I_N[h] = I_{\mathrm{CM}}[h]\,(1 + Z_N[h])$, through the **ecdf** against experimental data from three DC/DC converters operating with random phases. Specifically:

(a) The experimental data validity was confirmed by verifying the equivalence between the distribution of the assumed phases (angles) and measured phase distributions,

(b) Comparison between the Kluyver solution and the **ecdf** obtained from 1,000 and 4,000 measurements showed strong agreement, with some negligible deviations. A potential solution was proposed for implementation in future research investigations,

(c) Probability density analysis was conducted through histogram which was obtained by differentiating the **ecdf** for both measurement sets;

- Section 5.3 provides the first explicit computation of the probability that the h-th harmonic of the common mode current will be reduced in a setup with many converters compared to one with a single converter. The findings indicated diminishing EMI reduction with increasing number of converters. This can be intuitively understood because, with a higher number of converters, there are many more permutations of their initial switching times, with only a limited subset being in a particular 'opposing' state that enables EMI reduction.

In conclusion, the combined simulation and experimental results validated the Pearson's Random Walk model as an effective framework for characterising electromagnetic emissions in multi-converter power electronic systems.

Chapter 6

Conclusions

This chapter recapitulates the topics addressed in the various chapters of this thesis, revisiting the contributions outlined in the introduction. Future research directions are then discussed.

6.1 Chapter Synopsis and Contributions

Chapter 1 addressed a research gap in the EMC domain by highlighting the need for a statistical framework to characterise aggregate electromagnetic emissions in multi-converter configurations. The increasing deployment of PE converters across different domains including renewable energy systems, electric vehicles, aerospace applications and data centres motivated the challenge of modelling aggregated CM noise when multiple PE converters operate simultaneously, where electromagnetic interactions pose significant EMI challenges. This chapter introduced the EMI sources in PE converters, specifically the fast switching transitions that generate rapid voltage and current transients which translate into electromagnetic interference. Furthermore, the introduction identified a fundamental limitation in current

EMC standards, which predominantly focus on single-device evaluation. Individual device EMC compliance does not guarantee compliance in multi-device scenarios, expressed as $\mathrm{CE}_{individual} \nRightarrow \mathrm{CE}_{multiple}$. This limitation is particularly problematic as EMC regulations require manufacturers to assess compliance across all foreseeable configurations, with specific attention to worst-case scenarios, yet provide no guidance on how to achieve this. To address the challenge of modelling multiple interference sources, this thesis proposed a statistical approach based on Pearson's Random Walk theory.

Chapter 2 presented the main EMC issues generated by PE converters, namely the rapid changes in voltage and current rates of the switching devices utilised in PE converters; aggregation due to cooperation within a larger network; and beating phenomena. The chapter continued by showing literature examples where the EMC assessment was reliable for a single converter but important divergences arose as soon as multiple devices were considered, thus stating the necessity for statistical approaches to model the electromagnetic emissions from multiple PE converters. This contrasts with the current status quo of modelling multiple interference sources, which relies on deterministic approaches that represent only a narrow fragment of reality and are not always able to produce accurate models to describe the behaviour of multiple power electronic converters.

Chapter 3 introduced Pearson's Random Walk theory to characterise electromagnetic emissions in multi-converter configurations. Pearson's Random Walk, described by Karl Pearson in a letter to Nature[60], involves a person taking steps of equal length in random directions. The fundamental question concerns the probability distribution of the distance from the origin after n steps. This chapter established a mathematical analogy between Pearson's Random Walk and the electromagnetic behaviour of multiple PE converters. In this analogy, vectors represent the phase CM

current waveforms produced by each converter, with vector angles corresponding to their switch-ON times. By varying these angles, different vector paths are generated, corresponding to unique emissions patterns.

Pearson's Random Walk provided a means to express the total common mode current generated by multiple converters (having a damped oscillating shape) as the sum of the CM current generated by one converter (the reference) plus the contributions that arise from the time shifts due to the different switching-ON times of the additional converters ($I_N[h] = I_{\mathrm{CM}}[h]\,(1 + Z_N[h])$). Attention was then directed towards these contributions $Z_N[h]$ to the total CM current. The chapter concluded with Kluyver's solution for the distribution of the contributions to the emission levels (interference) generated by multiple PE converters through the **cumulative distribution function (cdf)**, which provided the probability that the magnitude of the contributions was lower than or equal to a certain threshold. In the author's view, *Chapter 3* demonstrated a successful implementation of Objectives 1 and 2 listed in Section 1.6.

Chapter 4 presented a methodology for verifying the applicability of Pearson's Random Walk model to PE converters. The model, expressed mathematically as $I_N[h] = I_{\mathrm{CM}}[h]\,(1 + Z_N[h])$, relates the CM current generated by N converters to that of a single converter. Vectors (or vector angles) forming paths analogous to random walk trajectories described by Pearson were employed to represent converters' switching-ON times.

The verification methodology employed two complementary approaches:

1. Simulation-based verification: An eight-converter simulation setup was implemented using MATLAB Simulink. Each converter was modelled as a full-bridge converter with inductive-resistive elements

and a parasitic capacitor of arbitrary value (realistically representing the metallic enclosure capacitance) to allow the CM current to flow. The CM current was measured at a common coupling point;

2. Experimental verification: A physical setup comprising three DC/DC converters based on Infineon CoolGaN HEMT[66] half-bridge evaluation boards was constructed. This setup employed function generators to provide precise phase control of the converter phases, with CM current measured via current probes.

For both verification approaches, a point $Z[h]$ representing a certain interference level was selected in the complex plane. This point could be reached through different switching-ON patterns of the converters (which corresponded to different vector paths). Once a path was arbitrarily chosen, the angles of these vectors were obtained (representing phases for the converters) and these phases were fed into the converters. Then, by comparing the converters' switchingON sequence with the initially chosen path, it was possible to assess whether Pearson's Random Walk summation model holds.

The simulation results demonstrated that this deterministic analysis confirmed that imposing agreement on the first harmonic led to agreement for higher harmonics, thus validating the summation model. The experimental analysis of recovering the vectors after operating the converters with the arbitrary chosen phases, involved two approaches: one FFT-based (similar to how these vectors were recovered from simulation data); and a second approach (τ -based) which consisted of recovering these vectors from time domain data through the detection of peaks in CM current values. It was observed that that the FFT-based method yielded vectors which presented minimal deviation, while the τ-based approach produced precisely aligned

vectors. The alignment in the second approach can be understood because the τ-based method inherently assumed unit-length vectors, which the FFT-method does not. However, since the deviation was minimal, the results confirmed verification of the summation model, and the FFT-based method is deemed as appropriate for further statistical exploration as presented in the following chapter.

In the author's view, *Chapter 4* demonstrated a successful implementation of Objective 3 listed in Section 1.6.

Chapter 5 presented the results in terms of the distribution of the magnitude of the contributions ($|Z_N[h]|$) to the total CM current generated by N converters. These contributions resulted solely from the different time-shifts among the PE converters. The **cumulative distribution function (cdf)** provided the probability that the length of these contributions was less than or equal to a certain value, which was the original question Pearson asked. The results obtained from both the simulation data and experimental data are juxtaposed with the analytical cdf.

More specifically, the results herein presented were organised as follows:

1. First, a comparison between the theoretical solution provided by Kluyver and the **empirical cumulative distribution function (ecdf)** obtained from running 1,000 simulations for 3, 5, and 8 converters. Results demonstrated consistent alignment between theoretical predictions and simulation outcomes across different harmonic numbers.

2. Secondly, a comparison between the theoretical solution provided by Kluyver and the **empirical cumulative distribution function (ecdf)** obtained from running 1,000 and 4,000 measurements of an

experimental setup consisting of 3 DC/DC converters operating with random phases. Results from these experimental data showed strong agreement with minor deviations.

Subsequently, the chapter addressed a fundamental research question: what is the probability that the CM current magnitude in a multi-converter setup will decrease compared to a single-converter arrangement? The analytical model demonstrated that this probability can be calculated as the volume of a cylinder whose base is a unit circle centred at $(-1, 0)$ and bounded by the **probability density function (pdf)** of $|Z_N[h]|$. Results revealed a decreasing probability of EMI reduction as the number of converters increases.

The chapter conclusively verified the PRW model through both simulation and experimental results, establishing it as an effective framework for characterising electromagnetic emissions in multi-converter systems. The new contribution included the explicit computation of EMI reduction probability in multi-converter setups, demonstrating that while possible, the likelihood of EMI reduction diminishes with an increasing number of converters. This last result can be also read as the opposite of the risk of increasing EMI. Indeed, such probability is the complement of the probability provided in this thesis.

In the author's view, *Chapter 5* demonstrated a successful implementation of Objectives 3 and 4 listed in Section 1.6.

6.2 Future Work

The work presented in this thesis identifies improvements for future research, some of which the author and collaborators have already begun to investigate.

Regarding the results presented in Chapter 5, concerning the reduction of EMI in multiple PE converter scenarios, a harmonic-by-harmonic basis analysis has been proposed. However, predicting the behaviour of multiple harmonics from a single one would be advantageous. From a practical standpoint, determining potential interrelationship between harmonics of the CM current could reduce system complexity and, consequently, the time required for system control. Indeed, achieving electromagnetic emission reduction across the entire frequency spectrum rather than focusing on individual harmonics represents a valuable objective. Whilst investigating such potential interrelationships and deriving precise relationships governing harmonic dependence requires further correlation analysis, initial findings demonstrate that a worst-case relationship can be established between contributions to the total CM at the fundamental frequency and contributions at higher-order harmonics. Since the aim is to estimate the value of the magnitude of harmonic $Z_N[h]$ based on $Z_N[1]$, we can study the ratio $Z_N[h]/Z_N[1]$. This is shown in Fig. 6.1, where x-axis presents $|Z_N[1]|$, while y-axis shows the ratio $|Z_N[h]/Z_N[1]|$, (the h-th harmonic is scaled with respect to the first harmonic) in log-log scale. The red points present the results of the Simulink simulation, and the golden points show the predictions of the model. As it can be clearly seen, the model and the simulation are in agreement and show similar relationships.

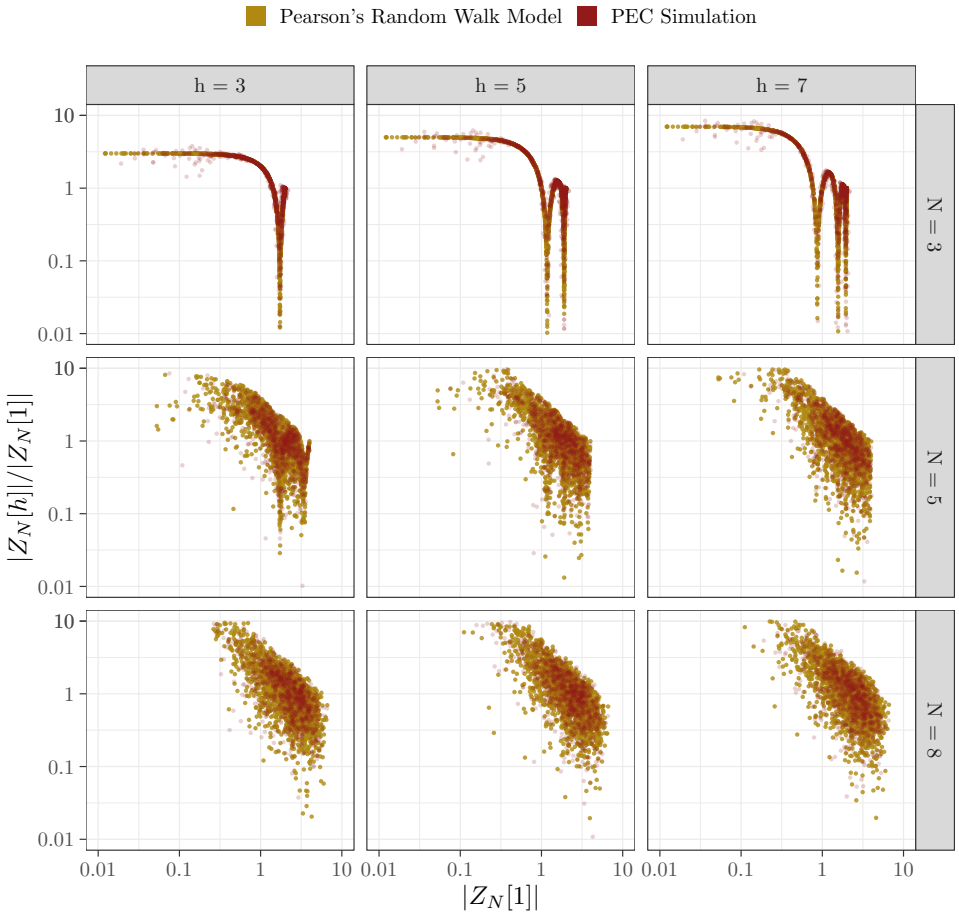

Figure 6.1: Correlation plot showing the relationship between the magnitude of the first harmonic $|Z_N[1]|$ (x-axis) and the ratio of higher harmonics to the first harmonic $|Z_N[h]/Z_N[1]|$ (y-axis), presented in logarithmic scale.

$$\left|\frac{Z_N[h]}{Z_N[1]}\right| = g(|Z_N[1]|) + \varepsilon_N, \tag{6.1}$$

where g is a (possibly nonlinear) function, and ε_N is a random variable, with parameters indexed by the number of converters N. Several candidates for the function g can be discussed, including sinc function.

Furthermore, a similar approach can be applied to develop modulation strategies that reduce EMI by orchestrating the operation of multiple similar converters within the same grid through coordinated control. Such an approach may demonstrate greater efficacy than conventional random modulation techniques. The fundamental rationale for developing such

modulation would be based on these steps:

1. Ensure the endpoint of vector $|Z_N[1]|$ (contributions to the total CM current due to the different switch-ON times of the converters, referred to the first harmonic) remains within the unitary circle shown in Section 5.3 to achieve EMI reduction;

2. Utilise the established relationship between harmonics to predict the magnitude of $|Z_N[h]|$ based on the known value of $|Z_N[1]|$;

3. Leverage the correlation between $|Z_N[1]|$ and any other $|Z_N[h]|$ to guide the system such that all harmonics remain within the unitary circle;

4. Implement coordinated control strategies that simultaneously manage the entire harmonic spectrum through this predictable relationship.

A second direction for further research work emerges from the findings on EMI reduction. While this thesis adopts a control-oriented perspective (where a continuous feedback loop would update the control over the system), an alternative approach could explore risk-based EMC considerations. In scenarios where direct control over a system is limited or absent, for instance, when N converters initially operate according to a specific synchronisation pattern over extended periods, jitter effects could eventually cause deviations that compromise EMI reduction benefits. These limitations are the reason for adopting probability-based approaches, such as randomised Pearson's Random Walk models in describing the electromagnetic behaviour of multiple PE converter. An intriguing perspective involves quantifying the risk of exceeding EMI thresholds, which represents the inverse of the EMI reduction demonstrated in this work. This

risk assessment framework connects directly to the established formula: risk = probability × severity. The probability component can be derived from methodologies proposed in this thesis, whilst incorporating known severity factors for specific applications would enable comprehensive risk quantification.

With reference to the assumption made in Chapter 3, where it was assumed that the model is based on a damped oscillation shape of the CM current, the author of this thesis has initiated an investigation to relax this constraint. A more general approach could examine whether the Pearson's Random Walk modelling can be applied to any periodic signal with an existing Fourier Transform. Preliminary results, based on experiments with synthetic datasets containing several known signals, suggest that the model maintains its validity regardless of the shape of the CM current, although some discrepancies occur. Fig. 6.2 displays the ecdfs derived from simulation results alongside the corresponding theoretical cdf for N set to $3, 5$ and 8, respectively. Different line styles and colors distinguish between the various functions, with theoretical predictions represented by dashed lines. Each subplot shows results for specific harmonic orders $h = 1, 7, 11$ and 19. M The orange-highlighted regions indicate where the theoretical cdf saturates ((reaching unity). As can be seen, the value saturates when $r = N - 1$, which can be understood by recognizing that the highest magnitude achievable by $|Z_N[h]|$ occurs when all the unitary vectors $e^{-\mathbf{j}2\pi f_{\text{sw}} h\tau_2}, \ldots, e^{-\mathbf{j}2\pi f_{\text{sw}} h\tau_N}$ align at the same angle, resulting in a magnitude of $N - 1$.

A couple of observations can be made. First, the theoretical model demonstrates strong correlation with simulation results across various input signals, validating the extension of the model to arbitrary periodic functions. Second, higher harmonic frequencies exhibit growing discrepancies between

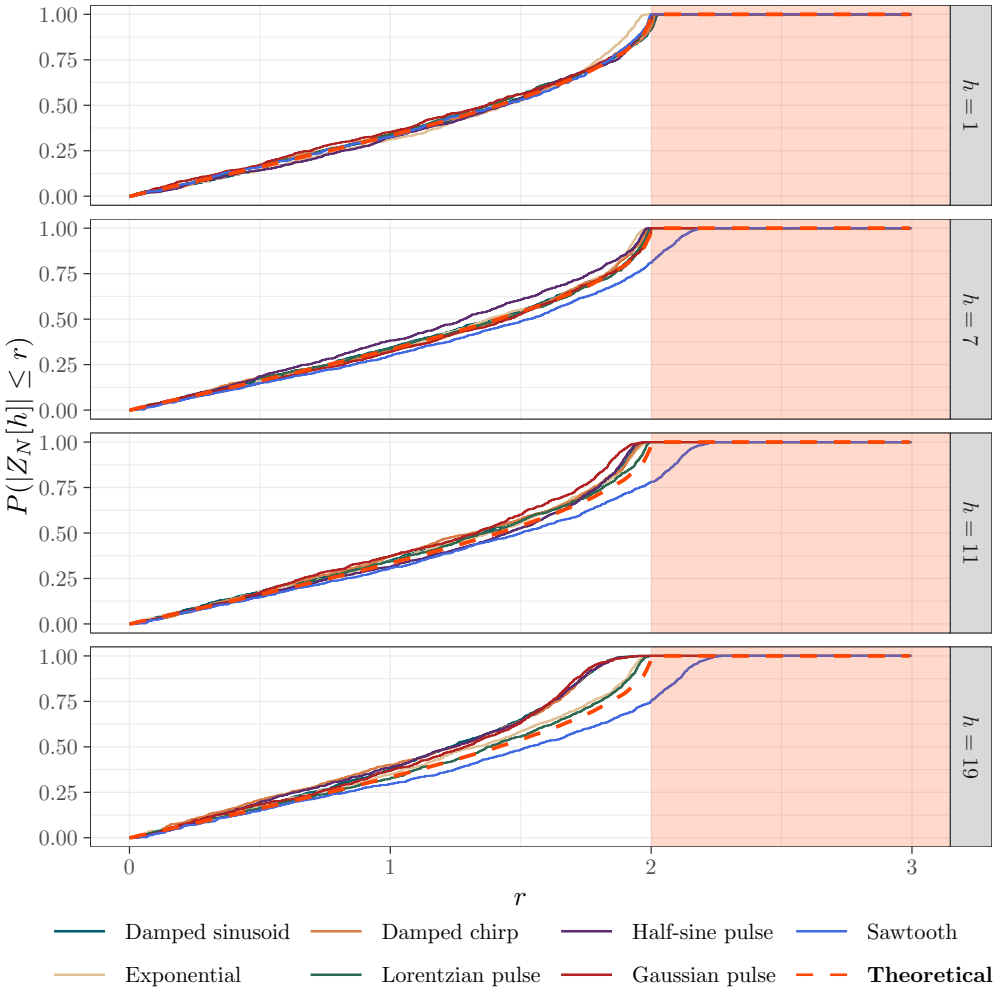

Figure 6.2: The ecdf of $Z_N[h]$, where $N = 3$. Each facet corresponds to a value of $h = 1, 7, 11$ and 19. Colours indicate different types of functions. The solid lines indicate $Z_N[h]$ obtained from simulations, while dashed line shows the theoretical solution to PRW.

theoretical predictions and simulation outcomes. This deviation can be attributed to computational precision limitations.

Finally, it is important to note that the model presented in this thesis is based on the assumption that the CM current follows a particular profile (damped oscillating sinusoid) and that the only variation is over the converters' switch-ON times, thus introducing a random phase shift or a phase shift with a certain distribution. However, additional factors such as variations in converter component values and manufacturing tolerances could have an impact. Therefore, this model could be further extended by incorporating variability in component values, PCB layout configurations and similar parameters, potentially resulting in a modified random walk where the step is no longer unitary but exhibits variable step size as the one described in [72].

Appendices

Appendix A

Function Generator Phases

This appendix aims to explain how the PE converter activation phases, as specified in Table A.1, were obtained through parallelogram formulae and implemented in the Function Generators.

	Converter 1	**Converter 2**	**Converter 3**	$\angle Z_3^{(l)}[h']$
Case 1	0°	8°	82°	45°
Case 2	0°	53°	127°	90°
Case 3	0°	143°	217°	180°
Case 4	0°	188°	262°	225°

Table A.1: Converter phase angles for different test cases

In order to deterministically verify Pearson's Random Walk, specific angles for the resultant vector $Z_3^{(l)}[h']$ were chosen, namely 45° $\left(\frac{\pi}{4}\right)$, 90° $\left(\frac{\pi}{2}\right)$, 180° ($\pi$) and 225° $\left(\frac{5}{4}\pi\right)$.

An arbitrary value for the length of $Z_3^{(l)}[h']$ is chosen ($|Z_3^{(l)}[h']| = 1.6$) in the complex plane as shown in Fig. A, where (l) indicates the possible path to reach such point; 3 indicates the number of converters; and h' refers to a generic harmonic of the switching frequency. This point represents a certain level of interference and, in the case of 3 converters, it can be

intuitively understood that there are only two paths to reach that point.

Choosing the known angles for $Z_3^{(l)}[h']$ and deriving the angles (phases) of the single converter serves to verify whether, once these single phases are fed into the function generators, the system performs as expected. This verification would confirm that the Pearson's Random Walk model holds, meaning that the obtained $|Z_3^{(l)}[h]|$ from operating the converters matches the initially chosen one $|Z_3^{(l)}[h']|$.

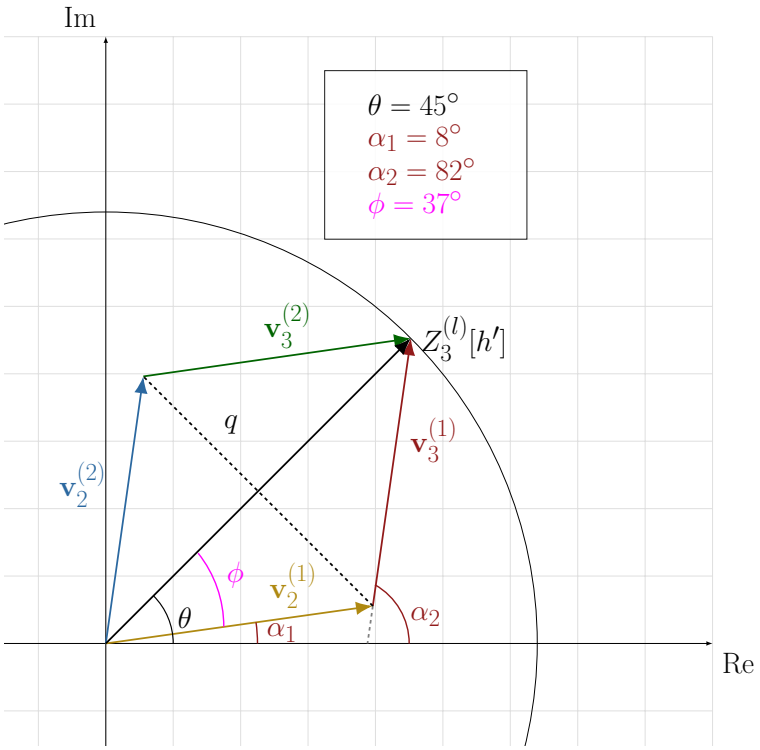

Figure A.1: Derivation of second and third converter phase angles using parallelogram vector formulae for a chosen point $Z_3^{(l)}[h']$ at 45°.

In Fig. A.1 the angles (converter's phases) are derived for a chosen $|Z_3^{(l)}[h']|$ at 45°. Since all the vectors $v_2^{(j)}$ and $v_3^{(j)}$ for $j = 1, 2$ represent the two possible paths, a rhombus can be identified.

Using trigonometric formulae:

$$\cos(\phi) = \frac{adjacent}{hypotenuse} = \frac{\frac{1.6}{2}}{1} = 0.8, \tag{A.1}$$

This means that:

$$\phi = \arccos(0.8) = 37^{\circ}, \tag{A.2}$$

With 3 converters there are two possible paths for $\theta = 45^{\circ}$:

1. $\alpha_1 = \theta - \phi = 45^{\circ} - 37^{\circ} = 8^{\circ}$
2. $\alpha_2 = \theta + \phi = 45^{\circ} + 37^{\circ} = 82^{\circ}$

This means that, assuming the first converter is always switched-ON with zero phase delay, the second and the third are switched-ON with 8° and 82°, respectively (first path composed of gold and red vectors), or conversely, the second and third converters are switched-ON with 82° and 88°, respectively (second path composed of blue and green vectors).

Appendix B

Differentiation of the Kluyver's cdf

The integral to be differentiated is the **cumulative distribution function (cdf)** provided by Kluyver. This integral is differentiated with respect to r,

$$\int_0^\infty r J_0(t)^{N-1} J_1(rt)\, dt. \tag{B.1}$$

The following steps are implemented:

1. Apply Leibniz's rule for differentiating under the integral sign;
2. Use properties of Bessel functions;
3. Apply the chain rule for the term $J_1(rt)$

First, the Leibniz's rule is used to bring the differentiation inside the integral:

$$\frac{d}{dr}\left[\int_0^\infty r J_0(t)^{N-1} J_1(rt)\, dt\right] = \int_0^\infty \frac{d}{dr}\left[r J_0(t)^{N-1} J_1(rt)\right]\, dt. \tag{B.2}$$

Next, the integrand is differentiated using the product rule:

$$\frac{d}{dr}\left[rJ_0(t)^{N-1}J_1(rt)\right] = J_0(t)^{N-1}J_1(rt) + rJ_0(t)^{N-1}\frac{d}{dr}[J_1(rt)]. \tag{B.3}$$

For Bessel functions, the derivative of $J_1(x)$ is:

$$\frac{d}{dx}[J_1(x)] = J_0(x) - \frac{J_1(x)}{x}. \tag{B.4}$$

Using the chain rule, the derivative of $J_1(rt)$ with respect to r is:

$$\frac{d}{dr}[J_1(rt)] = t \cdot \left(J_0(rt) - \frac{J_1(rt)}{rt}\right) = tJ_0(rt) - \frac{J_1(rt)}{r}. \tag{B.5}$$

Substituting this back:

$$\begin{aligned}\frac{d}{dr}\left[rJ_0(t)^{N-1}J_1(rt)\right] &= J_0(t)^{N-1}J_1(rt) + rJ_0(t)^{N-1}\left(tJ_0(rt) - \frac{J_1(rt)}{r}\right) \\ &= J_0(t)^{N-1}J_1(rt) + rtJ_0(t)^{N-1}J_0(rt) - J_0(t)^{N-1}J_1(rt) \\ &= rtJ_0(t)^{N-1}J_0(rt). \end{aligned} \tag{B.6}$$

Therefore, the final result is:

$$\frac{d}{dr}\left[\int_0^\infty rJ_0(t)^{N-1}J_1(rt)\,dt\right] = \int_0^\infty rtJ_0(t)^{N-1}J_0(rt)\,dt. \tag{B.7}$$

Appendix C

EMI Reduction - Analytical Integral Formulation

To quantify the probability of EMI reduction, one can calculate it as the volume of a cylinder whose base is the unit circle centred at (-1,0) and whose height is bounded by the joint **probability density function (pdf)**, $p(r, \theta)$ of $Z_N[h]$. Prior to this calculation, it is necessary to introduce the following concepts.

Joint pdf $p(r, \theta)$

Let $p(r, \theta)$ denote a joint **pdf** of $Z_N[h]$. Assuming that the magnitude (r) and phase (θ) of $Z_N[h]$ can be treated as independent random variables, $p(r, \theta)$ can be written as,

$$p(r, \theta) = p_N(r)\, p'_N(\theta), \tag{C.1}$$

where $p'_N(\theta)$ is taken from a uniform distribution $U(0, 2\pi)$. This gives $p'_N(\theta) = 1/2\pi$. Therefore,

$$p(r, \theta) = p_N(r) \, \frac{1}{2\pi}. \tag{C.2}$$

The function $p_N(r)$ can be obtained by differentiating the **cumulative distribution function (cdf)** provided by Kluyver [68]. A fundamental property of the **pdf** is that it must integrate to unity. Therefore,

$$\int_0^{2\pi} \int_0^{\infty} r \; p(r, \theta) \, d\theta \, dr = 1. \tag{C.3}$$

where the factor r represents the Jacobian resulting from the transformation from Cartesian to polar coordinates.

. . . . . .

Excursus: Jacobian Matrix

The computation of the Jacobian matrix for the transformation from Cartesian coordinates (x, y) to Polar coordinates (r, θ) can be as follows:

- $x = r \cos \theta$;
- $y = r \sin \theta$.

The Jacobian matrix requires the computation of all partial derivatives:

$$J = \begin{pmatrix} \dfrac{\partial x}{\partial r} & \dfrac{\partial x}{\partial \theta} \\ \\ \dfrac{\partial y}{\partial r} & \dfrac{\partial y}{\partial \theta} \end{pmatrix} \tag{C.4}$$

Calculating each partial derivative:

1. $\dfrac{\partial x}{\partial r} = \dfrac{\partial}{\partial r}(r\cos\theta) = \cos\theta;$
2. $\dfrac{\partial x}{\partial \theta} = \dfrac{\partial}{\partial \theta}(r\cos\theta) = -r\sin\theta;$
3. $\dfrac{\partial y}{\partial r} = \dfrac{\partial}{\partial r}(r\sin\theta) = \sin\theta;$
4. $\dfrac{\partial y}{\partial \theta} = \dfrac{\partial}{\partial \theta}(r\sin\theta) = r\cos\theta.$

This yields the Jacobian matrix:

$$J = \begin{pmatrix} \cos\theta & -r\sin\theta \\ \sin\theta & r\cos\theta \end{pmatrix}. \tag{C.5}$$

The determinant of this Jacobian is calculated as:

$$\begin{aligned} \det(J) &= \cos\theta \cdot r\cos\theta - (-r\sin\theta)\cdot\sin\theta \\ &= r\cos^2\theta + r\sin^2\theta \\ &= r(\cos^2\theta + \sin^2\theta) \\ &= r \cdot 1 = r \end{aligned} \tag{C.6}$$

. . . . . .

So the (C.3) becomes

$$\begin{aligned} \int_0^{2\pi}\int_0^{\infty} r\ p(r,\theta)\,d\theta\,dr = & \\ &= \int_0^{2\pi}\int_0^{\infty} r\ \frac{1}{2\pi}p_N(r)\,d\theta\,dr \\ &= \frac{1}{2\pi}\int_0^{2\pi} d\theta \int_0^{\infty} r\ p_N(r)\,dr \\ &= \frac{1}{2\pi}2\pi\int_0^{\infty} r\ p_N(r)\,dr \end{aligned}$$

$$= \int_0^\infty r \; p_N(r) \, dr \tag{C.7}$$

under the assumption that the **pdf** $p_N(r)$ integrates to 1.

Computation of the volume representing EMI reduction

In order to compute the volume representing the EMI reduction, beyond the **joint pdf** introduced above, it is necessary now to define the area of the unitary circle based at $(-1, 0)$ which must be multiplied by the height bounded by the **joint pdf** $p(r, \theta)$.

First,

$$|1 + Z_N[h]| \leq 1 \tag{C.8}$$

which is the condition to have EMI reduction represents a circle

$$(x + 1)^2 + y^2 = 1, \tag{C.9}$$

where the end of the vector $Z_N[h]$ must lie (shown in black in Fig. C.1). This circle is symmetrical with respect to the x-axis, which means that one can consider only the top part and then double the result. To differentiate over this area, two strategies can be implemented: first, the angle θ can be fixed and then the radius r varied, or the radius can be fixed and then the appropriate angle θ determined. The second strategy will be followed.

In Fig. C.1, the radius r is fixed and it is necessary to find the angles $\pi - \theta$ for which differentiation is required, which means finding the point A in Fig. C.2. It is convenient to consider a second circle of radius $r = Z_N[h]$,

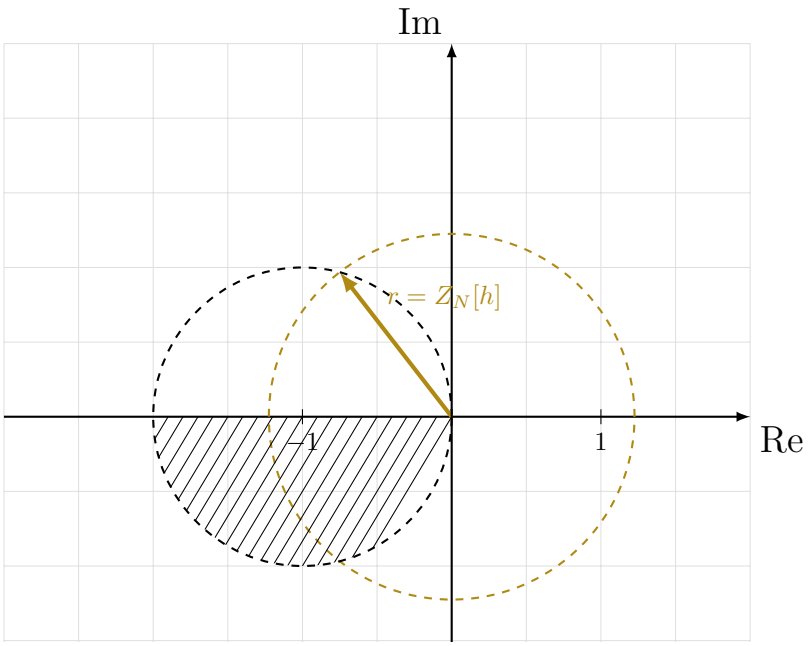

Figure C.1: Circle centred at $(-1, 0)$ symmetrical with respect to the x-axis. Only the upper half is considered.

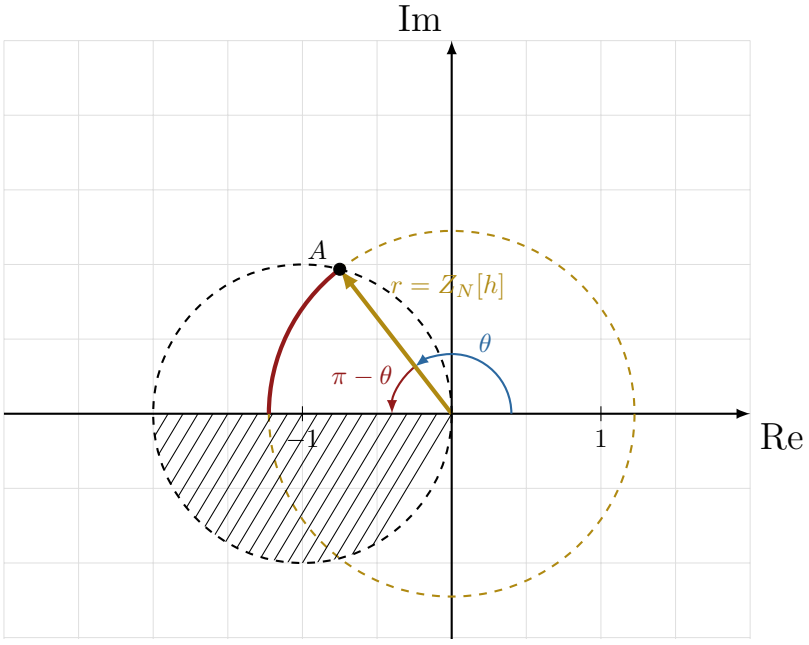

Figure C.2: Determination of the upper limit for the angle θ, for a specific r.

and the point A can be found as follows

$$
\begin{cases} x^2 + y^2 = r^2 \\ (x+1)^2 + y^2 = 1 \end{cases} \Rightarrow \begin{cases} x^2 + y^2 = r^2 \\ x^2 + 2x + 1 + y^2 = 1 \end{cases}
$$

$$
\Rightarrow \begin{cases} x^2 + y^2 = r^2 \\ x^2 + y^2 + 2x = 0 \end{cases}
$$

$$
\Rightarrow \begin{cases} x^2 + y^2 = r^2 \\ r^2 + 2x = 0 \end{cases}
$$

$$
\Rightarrow \begin{cases} \left(-\frac{r^2}{2}\right)^2 + y^2 = r^2 \\ x = -\frac{r^2}{2} \end{cases}
$$

$$
\Rightarrow \begin{cases} \frac{r^4}{4} + y^2 = r^2 \\ x = -\frac{r^2}{2} \end{cases}
$$

$$
\Rightarrow \begin{cases} y^2 = r^2 - \frac{r^4}{4} = r^2\left(1 - \frac{r^2}{4}\right) \\ x = -\frac{r^2}{2} \end{cases}
$$

$$
\Rightarrow \begin{cases} y = \pm\sqrt{r^2\left(1 - \frac{r^2}{4}\right)} = \pm r\sqrt{1 - \frac{r^2}{4}} \\ x = -\frac{r^2}{2} \end{cases} \tag{C.10}
$$

Only the positive solution $y = r\sqrt{1 - \frac{r^2}{4}}$ is considered.

The angle $\pi - \theta$ must then be determined. Then

$$|x| = r\cos(\pi - \theta) = -r\cos\theta. \tag{C.11}$$

Since x is negative, it is multiplied by -1

$$x = r\cos\theta, \tag{C.12}$$

which means that

$$x = -\frac{r^2}{2} \Rightarrow -\frac{r^2}{2} = r\cos\theta \Rightarrow \theta = \arccos\left(\frac{-r}{2}\right) = \theta(r), \tag{C.13}$$

and this is the value of θ for which the first circle is intersected.

The radius ranges from 0 to 2 and the angle from $\theta(r)$ to π; these limits define the area of the unitary circle base of the cylinder whose volume requires computation. This base must be multiplied by the height bounded by the **joint pdf** $p(r, \theta)$.

Therefore, the double integral to be computed is:

$$\int_0^2 \int_{\theta(r)}^{\pi} r\, p(r, \theta)\, d\theta\, dr \tag{C.14}$$

where r represents the Jacobian resulting from the transformation from Cartesian to polar coordinates. As polar coordinates (r, θ) are being considered rather than Cartesian coordinates (x, y), the differential elements $drd\theta$ form non-rectangular regions on the red arch in Fig. C.2. The Jacobian factor r accounts for this coordinate transformation.

So the volume is computed as:

$$\begin{aligned}\int_0^2 \int_{\theta(r)}^{\pi} r\, p(r,\theta)\, d\theta\, dr = & \\ &= \int_0^2 \int_{\theta(r)}^{\pi} r\, \frac{1}{2\pi}\, p_N(r)\, d\theta\, dr \\ &= \frac{1}{2\pi} \int_0^2 r\, p_N(r)\, [\pi - \theta(r)]\; dr \\ &= \frac{1}{2\pi} \int_0^2 r\, p_N(r) \left(\pi - \arccos\left(-\frac{r}{2}\right)\right)\; dr\end{aligned}$$

$$\arccos\left(-\frac{r}{2}\right) = \pi - \arccos\left(\frac{r}{2}\right)$$

$$= \frac{1}{2\pi} \int_0^2 r\, p_N(r) \arccos\left(\frac{r}{2}\right)\; dr \tag{C.15}$$

Since, only the upper portion of the circle was consdiered, the results needs to be doubled, leading to:

$$\int_0^2 \int_{\theta(r)}^{\pi} r\, p(r,\theta)\, d\theta\, dr = \frac{1}{\pi} \int_0^2 r\, p_N(r) \arccos\left(\frac{r}{2}\right)\; dr \tag{C.16}$$

So, the $P(I_N[h] \leq I_{CM}[h])$ is:

$$P(I_N[h] \leq I_{CM}[h]) = \frac{1}{\pi} \int_0^2 r\, p_N(r) \arccos\left(\frac{r}{2}\right)\; dr \tag{C.17}$$

under the assumption that the joint density $p(r,\theta)$ is normalized, which reduces to

$$\int_0^{\infty} r p_N(r) dr = 1. \tag{C.18}$$

Bibliography

[1] C. R. Paul, R. C. Scully, and M. A. Steffka, "Introduction to EMC," in *Introduction to Electromagnetic Compatibility*, 3rd ed. Hoboken, NJ, USA: John Wiley & Sons, 2023, pp. 1–9.

[2] R. W. Erickson and D. Maksimović, "Introduction," in *Fundamentals of Power Electronics*, 3rd ed. Cham, Switzerland: Springer, 2020, pp. 1–11.

[3] K. Strunz, K. Almunem, C. Wulkow, M. Kuschke, M. Valescudero, and X. Guillaud, "Enabling 100% renewable power systems through power electronic grid-forming converter and control: System integration for security, stability, and application to Europe," *Proc. IEEE*, vol. 111, no. 7, pp. 891–915, 2023.

[4] R. Sekar, D. S. Suresh, and H. Naganagouda, "A review on power electronic converters suitable for renewable energy sources," in *2017 International Conference on Electrical, Electronics, Communication, Computer, and Optimization Techniques (ICEECCOT)*, 2017, pp. 501–506.

[5] D. Kumar, F. Zare, and A. Ghosh, "DC microgrid technology: System architectures, AC grid interfaces, grounding schemes, power quality, communication networks, applications, and standardizations aspects," *IEEE Access*, vol. 5, pp. 12 230–12 256, 2017.

[6] A. Krishna and K. Gunawardane, "Emi issues in lvdc-microgrids due to power electronic converters," in *TENCON 2021 - 2021 IEEE Region 10 Conference (TENCON)*, 2021, pp. 833–838.

[7] P. Biczel and L. Michalski, "Simulink models of power electronic converters for dc microgrid simulation," in *2009 Compatibility and Power Electronics*, 2009, pp. 161–165.

[8] C. Bali, P. Choudekar, D. Asija, and R. Ruchira, "Power converters for dc microgrids modelling and simulation," in *2021 4th International Conference on Recent Developments in Control, Automation & Power Engineering (RDCAPE)*, 2021, pp. 38–42.

[9] K. P and S. Prakash, "A review of high efficiency power converters for electric vehicles applications," in *2024 5th International Conference on Electronics and Sustainable Communication Systems (ICESC)*, 2024, pp. 26–29.

[10] C. M, "An overview of the importance of power electronic converters in electric vehicle technologies," in *2023 9th International Conference on Advanced Computing and Communication Systems (ICACCS)*, vol. 1, 2023, pp. 199–204.

[11] L. Dorn-Gomba, J. Ramoul, J. Reimers, and A. Emadi, "Power electronic converters in electric aircraft: Current status, challenges, and emerging technologies," *IEEE Transactions on Transportation Electrification*, vol. 6, no. 4, pp. 1648–1664, 2020.

[12] G. Buticchi, P. Wheeler, and D. Boroyevich, "The more-electric aircraft and beyond," *Proceedings of the IEEE*, vol. 111, no. 4, pp. 356–370, 2023.

[13] A. Barzkar and M. Ghassemi, "Electric power systems in more and all

electric aircraft: A review," *IEEE Access*, vol. 8, pp. 169 314–169 332, 2020.

[14] A. Elwakeel, Z. Feng, N. McNeill, M. Zhang, B. Williams, and W. Yuan, "Study of power devices for use in phase-leg at cryogenic temperature," *IEEE Transactions on Applied Superconductivity*, vol. 31, no. 5, pp. 1–5, 2021.

[15] U. Nasir, Z. Iqbal, M. T. Rasheed, and M. Bodla, "Voltage mode controlled buck converter under input voltage variations," in *2015 IEEE 15th International Conference on Environment and Electrical Engineering (EEEIC)*, 2015, pp. 986–991.

[16] J. Sutaria and S. K. Rönnberg, "High frequency interaction of power electronics converters in ac and dc powered data centers," in *CIRED 2021 - The 26th International Conference and Exhibition on Electricity Distribution*, vol. 2021, 2021, pp. 718–722.

[17] F. F. Wang and Z. Zhang, "Overview of silicon carbide technology: Device, converter, system, and application," *CPSS Transactions on Power Electronics and Applications*, vol. 1, no. 1, pp. 13–32, 2016.

[18] K. Niewiadomski, R. Smolenski, P. Lezynski, J. Bojarski, D. W. P. Thomas, and F. Blaabjerg, "Comparative analysis of deterministic and random modulations based on mathematical models of transmission errors in series communication," *IEEE Transactions on Power Electronics*, vol. 37, no. 10, pp. 11 985–11 995, 2022.

[19] S. Peyghami and F. Blaabjerg, "Availability modeling in power converters considering components aging," *IEEE Transactions on Energy Conversion*, vol. 35, no. 4, pp. 1981–1984, 2020.

[20] S. Jahdi, O. Alatise, J. Ortiz-Gonzalez, P. Gammon, L. Ran, and

P. Mawby, "Investigation of parasitic turn-on in silicon igbt and silicon carbide mosfet devices: A technology evaluation," in *2015 17th European Conference on Power Electronics and Applications (EPE'15 ECCE-Europe)*, 2015, pp. 1–8.

[21] C. D. Fuentes, S. Kouro, and S. Bernet, "Comparison of 1700-v sic-mosfet and si-igbt modules under identical test setup conditions," *IEEE Transactions on Industry Applications*, vol. 55, no. 6, pp. 7765–7775, 2019.

[22] N. Li, M. B. Macavilca, C. Wu, S. Finney, and P. D. Judge, "Converter topology for megawatt scale applications with reduced filtering requirements, formed of igbt bridge operating in the 1000 hz region with parallel part-rated high-frequency sic mosfet bridge," *IEEE Transactions on Power Electronics*, vol. 39, no. 1, pp. 799–813, 2024.

[23] ——, "Converter topology for megawatt scale applications with reduced filtering requirements, formed of igbt bridge operating in the 1000 hz region with parallel part-rated high-frequency sic mosfet bridge," *IEEE Transactions on Power Electronics*, vol. 39, no. 1, pp. 799–813, 2024.

[24] J. Luszcz, "Conducted emissions origins in switch-mode power converters," in *High Frequency Conducted Emission in AC Motor Drives Fed by Frequency Converters*. Hoboken, New Jersey: John Wiley & Sons, Inc., 2018, pp. 21–24.

[25] Z. Hanzelka, A. Kempski, and R. Smoleński, "Quality problems in smart networks," in *Power Electronics in Smart Electrical Energy Networks*, R. M. Strzelecki and G. Benysek, Eds. London, UK: Springer, 2008, pp. 107–110, 125–132.

[26] Y. Liu, Z. Mei, S. Jiang, and W. Liang, "Conducted common-mode electromagnetic interference suppression in the ac and dc sides of a grid-connected inverter," *IET Power Electron.*, vol. 13, no. 13, pp. 2926–2934, 2020.

[27] P. Koch, N. Moonen, and F. Leferink, "Common mode current estimation for filter design for non-ideal back emf of a pmsm," in *2023 IEEE Symposium on Electromagnetic Compatibility & Signal/Power Integrity (EMC+SIPI)*, 2023, pp. 632–637.

[28] J. Luszcz, "Introduction to conducted emission in adjustable speed drives," in *High Frequency Conducted Emission in AC Motor Drives Fed by Frequency Converters*. Hoboken, New Jersey: John Wiley & Sons, Inc., 2018, p. 6.

[29] *IEC 60050-161 International Electrotechnical Vocabulary (IEV) - Part 161: Electromagnetic compatibility*, International Electrotechnical Commission Std., 1990, amendment 10.

[30] J. Luszcz, "Introduction to conducted emission in adjustable speed drives," in *High Frequency Conducted Emission in AC Motor Drives Fed by Frequency Converters*. Hoboken, New Jersey: John Wiley & Sons, Inc., 2018, pp. 5–9.

[31] "The electromagnetic compatibility regulations 2016," Government of Great Britain, London, UK, Statutory Instrument 2016/1091, December 2016, p. 27, Available: legislation.gov.uk.

[32] "Directive 2014/30/EU of the European Parliament and of the Council of 26 February 2014 on the harmonisation of the laws of the Member States relating to electromagnetic compatibility," European Parliament and Council of the European Union, Brussels, Belgium, Directive L 96/79-106, March 2014, consulted pages: L96/80, L96/81, L96/97.

[33] F. Leferink, C. Keyer, and A. Melentjev, "Static energy meter errors caused by conducted electromagnetic interference," *IEEE Electromagnetic Compatibility Magazine*, vol. 5, no. 4, pp. 49–55, 2016.

[34] J. Bojarski, R. Smoleński, A. Kempski, and P. Lezynski, "Pearson's random walk approach to evaluating interference generated by a group of converters," *Appl. Math. Comput.*, vol. 219, pp. 6437–6444, February 2013.

[35] IEC CISPR Working Group 4. (2024) Impact of 'increased number of devices' on EMC and radio protection. International Electrotechnical Commission. [Online]. Available: https://www.iec.ch/dyn/www/f?p=103:14:705228242272342::::FSP_ORG_ID,FSP_LANG_ID:50102,25

[36] International Electrotechnical Comission, "IEC TR 61000-3-6:2008 — Electromagnetic compatibility (EMC) — Part 3-6: Limits — Assessment of emission limits for the connection of distorting installations to MV, HV and EHV power systems," Standard, February 2008.

[37] Á. Espín-Delgado, S. K. Rönnberg, T. Busatto, V. Ravindran, and M. H. J. Bollen, "Summation law for supraharmonic currents (2–150 kHz) in low-voltage installations," *Electric Power Systems Research*, vol. 184, p. 106325, July 2020.

[38] E. Larsson and M. H. J. Bollen, "Measurement result from 1 to 48 fluorescent lamps in the frequency range 2 to 150 kHz," in *Proceedings of 14th International Conference on Harmonics and Quality of Power - ICHQP 2010*, 2010, pp. 1–8.

[39] S. Rönnberg, A. Larsson, M. Bollen, and J. L. Schanen, "A simple model for interaction between equipment at a frequency of some tens of khz," in *Proceedings of CIRED 21st International Conference on Electricity Distribution,*, 2011, pp. 6–9.

[40] M. Bollen, H. Hooshyar, and S. Rönnberg, "Spread of high frequency current emission," in *22nd International Conference on Electricity Distribution (CIRED),*, 2013, pp. 1–4.

[41] J. Sutaria, Á. Espín-Delgado, and S. Rönnberg, "Summation of Supra-harmonics in Neutral for Three-Phase Four-Wire System," *IEEE Open Journal of Industry Applications*, vol. 1, pp. 148–156, 2020.

[42] B. Czerniewski, J.-L. Schanen, and P. Zanchetta, "EMC Generation and Propagation in Embedded Grids with Multiple Converters," in *2019 10th International Power Electronics, Drive Systems and Technologies Conference (PEDSTC)*, 2019, pp. 433–438.

[43] P. Zumel, O. GarcÍa, J. A. Oliver, and J. A. Cobos, "Differential-Mode EMI Reduction in a Multiphase DCM Flyback Converter," *IEEE Transactions on Power Electronics*, vol. 24, no. 8, pp. 2013–2020, 2009.

[44] S. U. Hasan, Y. P. Siwakoti, and D. Lu, "Electromagnetic compatibility issues with off-the-shelf power converters: A case study," in *2022 32nd Australasian Universities Power Engineering Conference (AUPEC)*, 2022, pp. 1–4.

[45] R. Smolenski, P. Lezynski, J. Bojarski, W. Drozdz, and L. C. Long, "Electromagnetic compatibility assessment in multiconverter power systems – conducted interference issues," *Measurement*, vol. 165, p. 108119, Dec. 2020.

[46] H. J. Loschi, R. Smolenski, P. Lezynski, D. Nascimento, and G. Demidova, "Aggregated conducted electromagnetic interference generated by dc/dc converters with deterministic and random modulation," *Energies*, vol. 13, 07 2020.

[47] Z. Hanzelka, A. Kempski, and R. Smoleński, "Quality problems in smart networks," in *Power Electronics in Smart Electrical Energy Networks*, R. M. Strzelecki and G. Benysek, Eds. London, UK: Springer, 2008, pp. 107–110, 125–132.

[48] J. Luszcz, "Conducted emission origins in switch-mode power converters," in *High Frequency Conducted Emission in AC Motor Drives Fed by Frequency Converters*. Hoboken, New Jersey: John Wiley & Sons, Inc., 2018, pp. 21–38.

[49] H. Soltani, F. Zare, and J. Adabi, "Effect of switching time on output voltages of a multilevel inverter used in high frequency applications," in *2007 Australasian Universities Power Engineering Conference (AUPEC'07)*. IEEE, 2007, pp. 1–6.

[50] R. Smolenski, "Power electronic interfaces in smart grids," in *Conducted Electromagnetic Interference (EMI) in Smart Grids*, ser. Power Systems. London: Springer London, 2012, ch. 1, pp. 1–22.

[51] E. Ballukja, K. Niewiadomski, D. W. P. Thomas, S. Sumsurooah, M. Sumner, and J. Bojarski, "A statistical approach to predict the low frequency common mode current in multi-converter setups," in *2023 IEEE Symposium on Electromagnetic Compatibility Signal/Power Integrity (EMC+SIPI)*, 2023, pp. 7–12.

[52] N. Oswald, P. Anthony, N. McNeill, and B. H. Stark, "An experimental investigation of the tradeoff between switching losses and emi generation with hard-switched all-Si, Si-SiC, and all-SiC device combinations," *IEEE Transactions on Power Electronics*, vol. 29, no. 5, pp. 2393–2407, May 2014.

[53] L. Ran, S. Gokani, J. Clare, K. Bradley, and C. Christopoulos, "Conducted electromagnetic emissions in induction motor drive systems. i.

time domain analysis and identification of dominant modes," *IEEE Transactions on Power Electronics*, vol. 13, no. 4, pp. 757–767, 1998.

[54] Schaffner, "Schaffner Survey Reveals EMC Regulation Change Uncertainty," http://schaffner.com, 2023, accessed: 2024-11-21.

[55] R. Smolenski, "Conducted EMI issues in smart grids," in *Conducted Electromagnetic Interference (EMI) in Smart Grids*, ser. Power Systems. London: Springer London, 2012, ch. 3, pp. 47–53.

[56] *Industrial, scientific and medical equipment — Radio-frequency disturbance characteristics — Limits and methods of measurement (CISPR 11:2015, modified)*, The British Standards Institution Standard, May 2016.

[57] L. Verburgt, "The First Random Walk: A Note on John Venn's Graph," *The Mathematical Intelligencer*, vol. 42, 06 2020.

[58] O. I. Oluwafemi, E. O. Famakinwa, and O. D. Balogun, "Random walk theory and application," *World Journal of Advanced Engineering Technology and Sciences*, vol. 11, pp. 346–367, 2024.

[59] F. Xia, J. Liu, H. Nie, Y. Fu, L. Wan, and X. Kong, "Random walks: A review of algorithms and applications," *IEEE Transactions on Emerging Topics in Computational Intelligence*, vol. 4, no. 2, pp. 95–107, 2020.

[60] K. Pearson, "The Problem of the Random Walk," *Nature*, vol. 72, p. 294, 1905.

[61] J. C. Kluyver, "A local probability problem," *Nederlande Akademie van Wetenschap*, vol. 8, pp. 341–350, 1906.

[62] Y. Chu and S. Wang, "A generalized common-mode current cancelation approach for power converters," *IEEE Transactions on Industrial Electronics*, vol. 62, no. 7, pp. 4130–4140, 2015.

[63] C. R. Paul, R. C. Scully, and M. A. Steffka, "Conducted emissions and susceptibility," in *Introduction to Electromagnetic Compatibility*, 3rd ed. Hoboken, NJ, USA: John Wiley & Sons, 2023, pp. 287–310.

[64] A. Kempski, R. Smolenski, and R. Strzelecki, "Common mode current paths and their modeling in pwm inverter-fed drives," in *2002 IEEE 33rd Annual IEEE Power Electronics Specialists Conference. Proceedings (Cat. No.02CH37289)*, vol. 3, 2002, pp. 1551–1556 vol.3.

[65] K. Niewiadomski, P. Leżyński, R. Smoleński, J. Bojarski, M. Sumner, and D. W. P. Thomas, "Time-domain Assessment of Data Transmission Errors in Systems with Multiple DC/DC Converters," in *2020 International Symposium on Electromagnetic Compatibility - EMC EUROPE*, 2020, pp. 1–6.

[66] Infineon Technologies AG, *1EDF5673K Data Sheet, GaN EiceDRIVER™*, 2022, version 02.04. [Online]. Available: https://www.infineon.com/dgdl/Infineon-1EDF5673K-DataSheet-v02_04-EN.pdf?fileId=5546d46266a498f50166c9b5b486226a

[67] E. O. Brigham and R. E. Morrow, "The fast fourier transform," *IEEE Spectrum*, vol. 4, no. 12, pp. 63–70, 1967.

[68] J. C. Kluyver, "A local probability problem," in *The Netherlands: Nederlande Akademie van Wetenschap 8*, 1906, pp. 341–350.

[69] L. Malburg, N. Moonen, and F. Leferink, "Superposition of EMI in multiple interconnected SMPS," in *2022 IEEE International Sym-*

posium on Electromagnetic Compatibility & Signal/Power Integrity (EMC+SIPI), 2022, pp. 362–367.

[70] E. Ballukja, K. Niewiadomski, P. Koch, J. Bojarski, P. Evans, N. Moonen, M. Sumner, and D. W. P. Thomas, "A pearson's random walk method of estimating the electromagnetic emissions of n parallel connected power electronic converters," *IEEE Transactions on Electromagnetic Compatibility*, vol. 67, no. 3, pp. 1004–1015, 2025.

[71] M. Larbi, P. Besnier, and B. Pecqueux, "The Adaptive Controlled Stratification Method Applied to the Determination of Extreme Interference Levels in EMC Modeling With Uncertain Input Variables," *IEEE Transactions on Electromagnetic Compatibility*, vol. 58, no. 2, pp. 543–552, 2016.

[72] C. A. Serino and S. Redner, "The Pearson walk with shrinking steps in two dimensions," *J. Stat. Mech. Theory Exp.*, vol. 2010, no. 01, p. P01006, Jan. 2010. [Online]. Available: https://dx.doi.org/10.1088/1742-5468/2010/01/P01006

Acknowledgements

"Io gli studi leggiadri
Talor lasciando e le sudate carte,
Ove il tempo mio primo
E di me si spendea la miglior parte..."

— Giacomo Leopardi

Oh dear, you managed to get to the end of *le sudate carte* (laboured pages) and it's time for expressing gratitude to people who surrounded me during this journey.

First of all, I would like to express my deepest gratitude to my supervisors: Prof. Dave Thomas who gave me the opportunity to be part of the SCENT Marie Skłodowska Curie project. I am thankful for the support and freedom you provided throughout this journey. Thank you for all of your knowledge. Your knowledge has been invaluable. I must also mention how comforting I found our established tradition of enjoying a pint at the Old Trip to Jerusalem followed by an Indian meal at Laguna whenever we had cause for celebration. I would like to extend my gratitude to Prof. Mark Sumner, whose kindness and generous support were fundamental throughout these years. Thank you to Prof. Paul Evans for assuming the mantle of supervision after my two main supervisors retired. I am most grateful for your invaluable support, and consistently insightful queries during each of our meetings. I sincerely thank my supervisors from the University of Twente, Prof. Frank Leferink whose knowledge and charisma exemplify what an excellent Professor and gentleman ought to be. Thank you to Robert Smolenski for your guidance and support; each visit to the University of Zielona Gora was made inspiring by your motivation and warm welcome.

I express my gratitude to the Marie Skłodowska Curie Actions, which have made possible such an inter-European doctoral project.

I would like to thank Niek for the opportunities given to me, and for his continual encouragement. Jestem wdzieczny Dr. Jackowi Bojarskiemu za przekazanie zarówno jego pasji do matematyki, jak i jego bezwarunkowego wsparcia.

Thank you, Karol and Marianna. I arrived in Nottingham alone, yet swiftly discovered family. My deepest thanks to Karol for your unwavering support as a friend, brother and companion on our numerous shared adventures.

Grazie ai miei amici Caterina, Alice e Denis per esserci per il prezioso tempo insieme, per il supporto, per i vostri consigli e le nostre mangiate.

Grazie Francesca, sei una delle cose più belle che porto con me dall'esperienza a Nottingham. La tua calma, maturità e personalità sempre riconoscente sono una vera benedizione. Daniel (and your beautiful dog Finn), thank you for all the splendid walks through the beautiful British countryside and for all the time spent together. Thank you to Vasso and Dasha, my most brilliant colleagues and dear friends, to Patrick for your remarkable generosity of spirit.

Grazie alla Dottoressa Laura Milanese per il suo costante supporto.

Infine, un immenso grazie soprattutto ai miei genitori Valbona e Ferdinant. *E dashura mami, i dashur babi, kemi kaluar kohë shumë të bukura por edhe sfiduese. Faleminderit për të gjithë dashurinë e pakushtëzuar që kam marrë nga ju të dy. Mami, ke qenë një shembull i një gruaje kokëulur dhe punëtore por e vendosur për të arritur qëllimet e saj. Babi, ke kaluar plot sfida në jetë dhe je duke kaluar një shumë të madhe. Ti je një shembull mirësie dhe ndihme të pakursyer e të painteresuar ndaj të tjerëve. Një faleminderit edhe për gjyshërit e mi për dashurinë e dhënë.*